Title

Influence of Synthetic Conditions on the Polyol Process for High Power High Energy Materials: Structural and Electrochemical Properties

Author

Yoon, Hyojung

Publication Date

2016

UNIVERSITY OF CALIFORNIA, SAN DIEGO

Influence of Synthetic Conditions of Polyol Process on High Power High Energy Materials: Structural and Electrochemical Properties

A dissertation submitted in partial satisfaction of the
requirements for the degree Doctor of Philosophy

in

Materials Science and Engineering

by

Hyojung Yoon

Committee in charge:

Professor Ying Shirley Meng, Chair
Professor Olivia A. Graeve
Professor Joanna M. McKittrick
Professor Yu Qiao
Professor Oleg Shpyrko

2016

The Dissertation of Hyojung Yoon is approved, and it is acceptable in quality and form for publication on microfilm and electronically:

Chair

University of California, San Diego

2016

DEDICATION

To my parents,

Kuemlim Ko and Bokyoung Yoon

TABLE OF CONTENTS

LIST OF FIGURES

LIST OF TABLES

ACKNOWLEDGEMENTS

First of all, I would like to express my gratitude to my thesis advisor Dr. Ying Shirley Meng for providing me all the opportunities to do this research and her continuous support. I was sincerely honored to meet and work with her. Through countless advice and encouragement, I can finally be ready to fly on my own. I shall never forget her endless advice and help. I would also like to thank my co-advisor Dr. Sungho Jin for his support and advice. I would like to extend my grateful acknowledgement to my other committee members: Dr. Olivia A. Graeve, Dr. Joanna M. McKittrick, Dr. Yu Qiao, and Dr. Oleg Shpyrko for their time and guidance.

I would also like to acknowledge my collaborators and co-authors in UCSD, with whom I had many useful and stimulating discussions. I'm also grateful to all my group mates in Laboratory for Energy Storage and Conversion (LESC) and all the senior and junior students in UCSD, who have helped and inspired me in many ways. Finally, I would like to express my special thanks to collaborator and co-authors, Dr. Jim Ciston, and Chengyu Song at Lawrence Berkeley National Laboratory, and Syed Khalid at Brookhaven National Laboratory.

Chapter 4, in full, is a reprint of the material "In Situ Non-aqueous Nucleation and Growth of Next Generation Rare-Earth-Free Permanent Magnets" as it appears in the Physical Chemistry Chemical Physics, Hyojung Yoon, Aoran Xu, George E. Sterbinsky, Darico A. Arena, Ziying Wand, Peter W. Stephens, Ying Shirley Meng, and Kyler J. Carroll, 2015, 17, 1070. The dissertation author was the primary investigator and author of this paper. All the experiment and writing were performed by the author.

Chapter 5, in full, is currently under review for publication of the material “Mitigating Surface Structural Instability of High Voltage Spinel Cathode Materials in Li-ion Batteries” Hyojung Yoon, Hyun-Man Cho, Danna Qian, Mahsa Sina, Jim Ciston, Chengyu Song, and Ying Shirley Meng. The dissertation author was the primary investigator and author of this paper. All the experiment and writing were conducted by the author except computational calculations.

Chapter 6, in full, is currently being prepared for submission for publication of the material “Probing Defects and Electrochemical Properties in Polyol Synthesized High Voltage $LiCoPO_4$ Olivine Materials” Hyojung Yoon, Jessie Lin, Mahsa Sina, Hyeseung Chung, Jim Ciston, and Ying Shirley Meng. The dissertation author was the co-primary investigator and author of this paper. All the experiment parts were performed by the author.

Chapter 7, in part, is currently being prepared for submission for publication of the material “Probing the Surface Structure of Polyol Syntehsized High Energy $LiNi_xCo_yMn_zO_2$ Layered Cathode Material ($x + y + z = 1$)”. Hyeseung Chung, Hyojung Yoon, Jessie Lin, and Ying Shirley Meng. The dissertation author was the co-investigator and co-author of this material.

For the last but not least, my deepest gratitude goes to my parents Kuemlim Ko and Bokyoung Yoon for their love, patience and never-ending support during my Ph.D.

I would like to acknowledge the financial support from the U.S. Department of Energy Advanced Research Project Agency – Energy (ARPA-E) under the contract # DE-AR0000192 and DE-AR0000396.

VITA

2009	Bachelor of Science, Inha University, Incheon, Republic of Korea
2011	Master of Science, Inha University, Incheon, Republic of Korea
2016	Doctor of Philosophy, University of California, San Diego, USA

PUBLICATIONS

1. **H. Yoon**, J. Hong, C. W. Park, D. W. Park, and S. E. Shim, "An Inexpensive Route to Prepare Mesoporous Hollow Silica Microspheres using W/O ethanol/edible soybean oil Macroemulsion as the Template", *Materials Letters*, 63, 2047-50 (2009).

2. **H. Yoon**, J. Lee, D. W. Park, C. K. Hong, and S. E. Shim, "Preparation and Electrorheological Characteristic of CdS/polystyrene Composite Particles", *Colloid and Polymer Science*, 288, 613-9 (2010).

3. **H. Yoon**, Y. M. Rhym, D. H. Kim, and S. E. Shim, "Optical properties of PMMA/CdS Nanoparticles prepared by in situ and ex situ surfactant-free emulsion polymerization", *Colloid and Polymer Science*, 289, 1185-9 (2011).

4. **H. Yoon**, Y. M. Rhym, and S. E. Shim, "In situ synthesis of polystyrene/nano-CdSe core/shell microspheres in aqueous solution at room temperature", Colloid and Polymer Science, 291, 1155-62 (2013).

5. **H. Yoon**, A. Xu, G. Sterbinsky, D. Arena, Z. Wang, P. Stephens, K. Carroll, and S. Meng, "In situ non-aqueous nucleation and growth of next generation rare-earth-free permanent magnets", Phys. Chem. Chem. Phys., 12, 1070-6 (2015).

6. M. Wang, A.V. Le, Y. Shi, D. Noelle, **H. Yoon**, M. Zhang, S. Meng and Y. Qiao, "Effects of Angular Fillers on Thermal Runaway of Lithium-ion Battery", *J. Mater. Sci. and Tech.*, Accepted, Paper No. JMST-2015-2217.R1 (2016).

7. **H. Yoon**, H. Cho, D. Qian, M. Sina, C. Song, J. Ciston and S. Meng, "Mitigating Surface Structural Instability of High Voltage Spinel Cathode Materials in Li-ion Batteries", *Nature Communication*, Under Review (2016).

8. A.V. Le, M. Wang, Y. Shi, D.J. Noelle, **H. Yoon**, Y.S. Meng, D. Wu, J. Fan, and Y. Qiao, "Heat Generation of Mechanically Abused Lithium-ion Battery Cell Based on Thermally Sensitive Cathode Binder*", J. Compos. Mater.*, Submitted (2016).

9. M. Wang, A.V. Le, D.J. Noelle, Y. Shi, **H. Yoon**, M. Zhang, Y.S. Meng, and Y. Qiao, "Effects of Electrode Pattern on Thermal Runaway of Lithium-ion Battery", *Int. J. Damage. Mech.*, Submitted (2016).

10. **H. Yoon**, J. Lin, H. Chung, M. Sina, J. Ciston, S. Shim and S. Meng, "Probing Defects and Electrochemical Properties in Polyol Synthesized High-voltage LiCoPO4 Cathode", *J. Electrochem. Soc.*, Submitted (2016).

11. H. Chung, **H. Yoon**, J. Lin, Y. S. Meng, "Probing the Surface Structure of Polyol Syntehsized High Energy $LiNi_xCo_yMn_zO_2$ Layered Cathode Material ($x + y + z = 1$)", in preparation (2016).

ABSTRACT OF THE DISSERTATION

Influence of Synthetic Conditions on the Polyol Process for High Power High Energy Materials: Structural and Electrochemical Properties

by

Hyojung Yoon
Doctor of Philosophy in Materials Science and Engineering
University of California, San Diego, 2016

Professor Ying Shirley Meng, Chair

With the rapid depletion of conventional energy sources based on fossil fuels and increasing energy demand, sustainable and renewable energy technologies, such as solar, wind, hydroelectric power, have been drawn worldwide attention in energy-based economics. Because of their uncontrollable and intermittent nature, large-scale high-power electrical energy storage (EES) system is required to increase reliability of renewable energy resources. Among various energy storage systems, lithium-ion batteries (LiBs) are considered as the most important rechargeable energy storage system.

However current LiB technology is still inadequate to compete against the conventional fossil fuels and implement in the large-scale applications: Key questions are cost, energy density, cycling life, and safety issues.

In the first part of this dissertation, rare-earth-free permanent magnets (PMs) are intensively studied. Our innovative approach, using polyol process, developed nanostructured cobalt carbide (NCC) consisting of an assembly of Co_2C and Co_3C nanoparticles. The resulting material exhibits an energy product of greater than 15.84 MGOe at room temperature before compaction, which is confirmed through vibrating sample magnetometer (VSM) and first order reversal curves (FORCs). An understanding of the formation mechanism, using *in situ* time-resolved x-ray absorption spectroscopy (XAS), and the correlation between phase contributions to the properties are described in detail. Our success in the development of rare-earth-free PMs may provide a cost-effective and sustainable platform for clean technology applications.

Although the performances of LiBs have been drastically improved, the limit in terms of the energy density and material stability still needs to be resolved. In the second part, high-voltage cathode materials, spinel $LiNi_{0.5}Mn_{1.5}O_4$ (LNMO) and olivine $LiCoPO_4$, are investigated to understand the influence of synthetic conditions of polyol synthesis on their electrochemical properties and structural stabilities upon cycling. High-angle annular dark field scanning transmission electron microscopy (HAADF-STEM) and X-ray photoelectron spectroscopy (XPS) allow us to determine the evolution of phase transformation accompanied with the migration of transition metal (TM) ions at the surface and electrode/electrolyte interfaces.

Chapter 1. Introduction and Motivation

1.1. Li-ion Batteries

Rechargeable lithium ion battery (LIB) technology has been most extensively used in energy storage systems for powering consumer electronics and power tools for the past several years.[1-2] Compared with other commonly used batteries, LiBs are featured by high energy/power density, long life and environmental friendliness. With the recent development of hybrid electric vehicles (HEV) and electric vehicles (EV) such as Tesla, Toyota Prius, Nissan Leaf etc., the rapid growth of interest in LiB research has been accelerated. LIBs are the most suitable candidates for it, because lithium weighs lightest, holds highest voltage, and greatest energy density of all metals.[3-4]

In the early 1990s, Sony commercially introduced the LiB technology based on the use of Li-intercalation compounds. Figure 1.1 illustrates the basic working principles of LiB system, which consists of a positive (cathode) and a negative (anode) electrode separated by a separator containing an electrolyte. The most common cathode material is the oxides of transition metals, which can undergo oxidation to higher valences when lithium is removed.[5-6] As well known, carbon-based compound and Li-containing alloys are the most common anode materials. Especially, graphite has a hierarchical structure to possess the Li ion between the inter-slabs serve as an anode. A micro-porous separator allows physical separation between the positive and negative electrodes, preventing short circuit. The electrolyte, as an ion conductor to provide a medium to transport electroactive Li^+ ions, is an organic solvent typically consisting of alkyl carbonates and dissociated $LiPF_6$ salts. The Li ions flow through the electrolyte while the electrons generated from the reaction go through the external circuit, thus the electrode system must allow for the flow of both lithium ions and electrons.[6] The electrolyte should features high ionic conductivity, high melting points and maintain stability within the operating voltage (0.8 – 4.5 V).[7] Upon the discharge, Li-ion is inserted into the cathode material and the transition metal ions in the cathode are reduced to lower valence by accepting electrons generated from the anode as shown in Figure 1.1. The rates of these processes, occurs at the electrode-electrolyte interface, determine the maximum discharge current, thus the cathode performance depends critically on the electrode microstructure and morphology. The developments of cathode materials therefore have become crucial and receive much attention in recent decade.

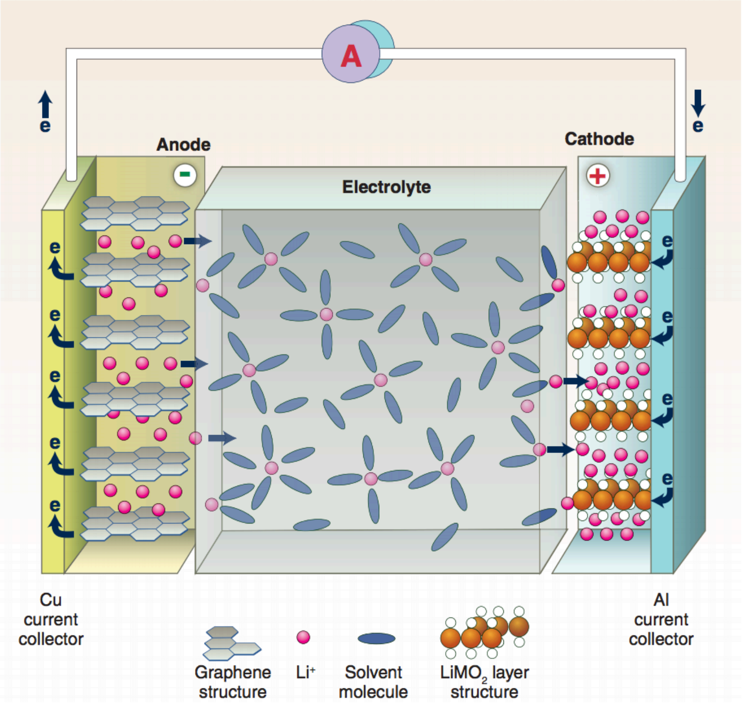

Figure 1.1 Schematics for the operating principle of lithium-ion battery (discharging)[2]

1.2. Permanent Magnets

Permanent magnets (PMs), specifically those containing rare earth metals, are expending across many technological applications. They are an indispensible component of many applications in electric, electronics, communications and automobile industries. One area where they can make a major impact is in the field of electric motors. Because they produce high torque with a much smaller motor, electric motors containing permanent magnets are becoming more common, yet this higher torque is solely associated with rare earth PMs.

The development of existing permanent magnet systems has occurred in abrupt and substantial leaps (Figure 1.2). The first significant discovery was AlNiCo in the 40's. The next major find occurred in the late 60's when the first rare earth magnet SmCo was discovered. Hexagonal $SmCo_5$ compound with a $CaCu_5$-type structure appeared as the first rare-earth high-performance magnets.[8-9] The compound has magnetic properties that are suitable for a permanent magnet, such as a large uniaxial magnetocrystalline anisotropy ($\mu_0H_A \sim 28$ T), a relatively high saturation magnetization ($J_s \sim 1.14$ T) and a high Curie temperature ($T_c = 720$ °C). The $(BH)_{max}$ of this type of magnet reached 160 kJ m^{-3}. The Sm_2Co_{17} compound has a higher saturation magnetization ($J_s \sim 1.25$ T) and a higher T_c than the $SmCo_5$ compound; however, the anisotropy field is smaller.[10] The discovery of this "super-magnet" initiated a flurry of activity to develop better magnets from more readily available materials. The early 80's saw the development of the NdFeB system, which had the largest energy product to date. The body centered tetragonal $Nd_2Fe_{14}B$ phase,[11] process via melt-spinning[12-13] and powder-metallurgy[14] techniques, results in $(BH)_{max}$ greater than 288 kJm^{-3}.

However, there has not been a commercial non-rare earth magnet discovered that approaches the energy products observed in the SmCo or NdFeB systems. Therefore, studies on finding and developing new permanent magnet materials are strongly in demand.

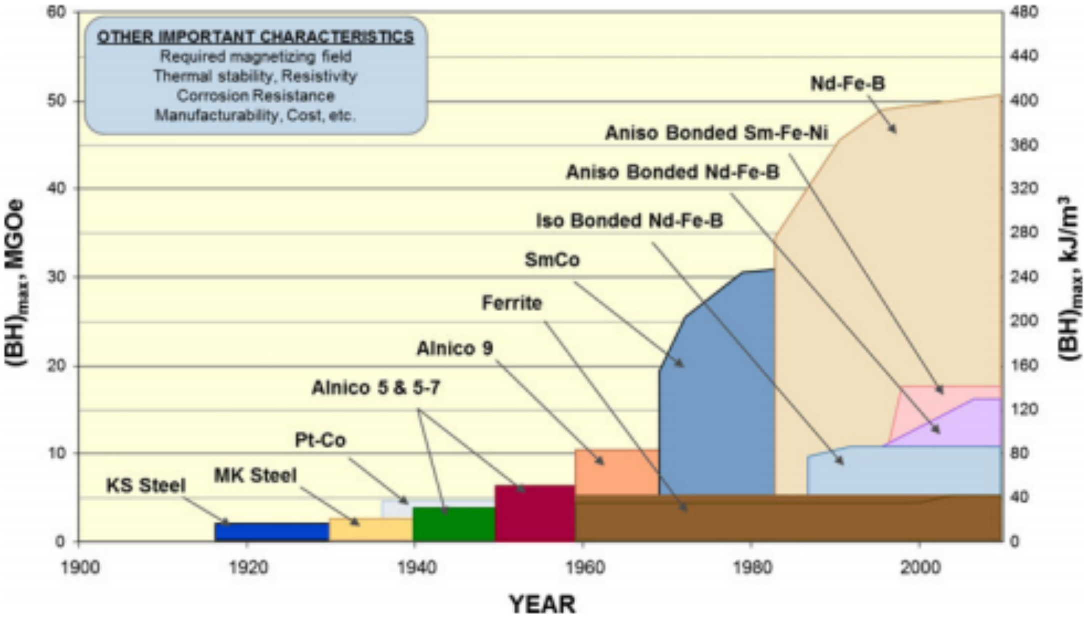

Figure 1.2 Historical trend of the improvement in the maximum energy product for commercially produced permanent magnets[15]

1.3. Conventional Cathode Materials in Li-ion Batteries

Categorized by structure, the conventional cathode materials include $LiMO_2$ (M = Co, Ni, Mn, etc.) layered compounds, $LiMPO_4$ (M = Fe, Mn, Ni, Co, etc.) olivine compound, and LiM_2O_4 (M = Mn, Ni, etc.)spinel compounds. Goodenough firstly demonstrated that the $LiCoO_2$ had a layered structure and the lithium could be removed electrochemically.[16] Since the $LiCoO_2$ became a viable cathode material, the transition metal (TM) intercalation oxides have drawn significant interests at the cathode materials.

Figure 1.3(a) illustrates the ideal structure of the layered compound $LiMO_2$. The oxygen anions form a close-packed lattice with cations located in the 6-coordinated octahedral crystal site. This structure allows the 2D Li diffusion pathways in which the MO_2 slabs and Li layers are stacked alternatively. Although the conventional layered oxide $LiCoO_2$ has been commercialized as the cathode materials since 1990, the intrinsic structural instability of the material limits the specific capacity, about 140mAh/g which is only half of its theoretical capacity. The phase transformation proceeds when more than half of the Li-ions are extracted from the structure.

In 1997, Padhi *et al.* discovered the electrochemical properties of the olivine phase, in particular $LiFePO_4$.[17] The olivine structure of $LiMPO_4$ is shown in Figure 1.3(b). This material brought drastic changes in electrochemical energy storage because of potentially low cost, plentiful elements, environmentally benign. The discharge potential of the $LiFePO_4$ is about 3.4 V vs. Li with the specific capacity of 170 mAh/g and it is very stable during discharge/recharge: no significant capacity fading was observed even after long cycles. However, this material has a very low conductivity; it could achieve the theoretical capacity only at a very low current density or at elevated temperatures due to the low Li diffusion at the interface.

The LiM_2O_4 spinel cathode was originally proposed by Thackeray *et al.* in 1983.[18] Figure 1.3(c) shows the structure of LiM_2O_4 spinel. The oxygen anion framework contains cubic close-packed and it is same as that of $LiMO_2$ layered structure, differing only in the distribution of the cations among the available octahedral and tetrahedral sites. TM cations still occupy the octahedral site but 1/4 of them are located in the Li layer, leaving 1/4 of the sites in transition metal layer vacant. Li ions occupy the tetrahedral sites in Li layer that share faces with the empty octahedral sites in the transition metal layer. Although the spinel structure is based on a three-dimensional MO_2 host and the vacancies in transition metal layer ensure the three-dimensional Li diffusion pathways, it has problem in terms of the capacity fading, resulting from Mn ion dissolution into to electrolyte during the electrochemical reactions.

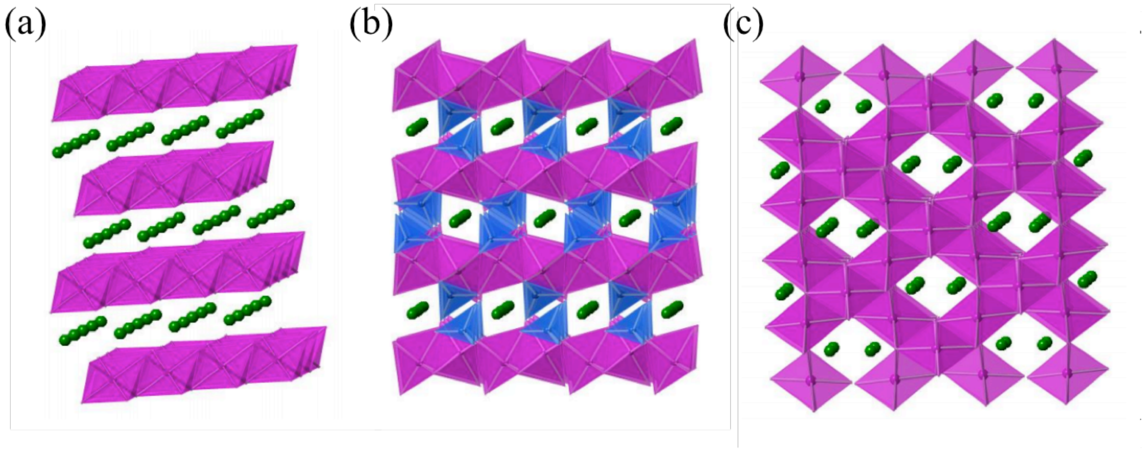

Figure 1.3 Structures of the conventional intercalation based cathode materials. Layer (a), (b) olivine (b), and spinel (c) structure (Green: Li-ions; Pink: TM-ions; Blue: P-ions)

Chapter 2. Background

2.1. Polyol Synthesis

In nanoparticle synthesis, the polyol process appears as an easy to carry out and versatile route among the chemical, physical, or electrochemical processes.[19] Initially, the polyol process was described as a novel route for preparing elemental metals and alloys via reduction of inorganic precursors in various polyhydric alcohols namely α-diols or etherglycols such as ethylene glycol, propylene glycol, tetraethylene glycol, etc..[20-22] Polyols, as well as monoalcohols, are mild reducing agents and also coordinating solvents, which can form complexes with many metal cations, owing to their chelating properties.[23-24] The solid inorganic precursor is suspended in the liquid polyol, which may be quite soluble (nitrate, chloride, acetate) or only partially soluble (oxide, hydroxide), then the solution is stirred and heated to a given temperature which can reach the boiling point of the polyol for less reducible metals as illustrated in Figure 2.1. The reaction occurs via a progressive or total dissolution of the solid precursor.

Beside metals, the polyol process turned out to be suitable for the preparation of nano-sized binary and ternary oxides as well as phosphates, sulfides or halogenides, too.[22, 25-26] It can be achieved through forced hydrolysis and inorganic polymerization. The final compound of these reactions depends mainly upon the hydrolysis ratio h defined as the amount of water added in the polyol and the amount of metal involved.

In general, the characteristic features of the polyol synthesis can be summarized as given below

- Inorganic compounds/salts are often well soluble because of the polarity of the polyols (ε > 30)
- The reaction proceeds in two steps: Nucleation and particle growth, resulting controllable morphology (Figure 2.2).
- The reaction performed at temperatures up to the boiling points of the polyols (e.g., diethylen glycol = 197 °C, tetraethylene glycol = 314 °C), resulting well-crystallized materials.
- The chelation of the solid nuclei by the polyols: Limiting the particle growth and preventing agglomeration of the particles.
- The polyol process is comparably easy to perform and suitable for a preparation of larger quantities.

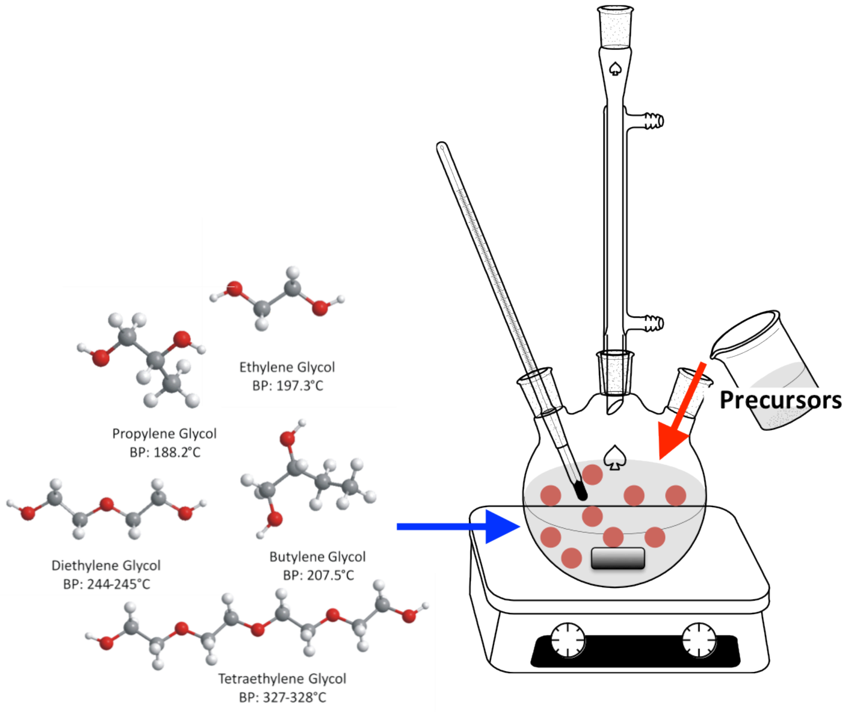

Figure 2.1 Schematic illustration of the polyol process with various polyols

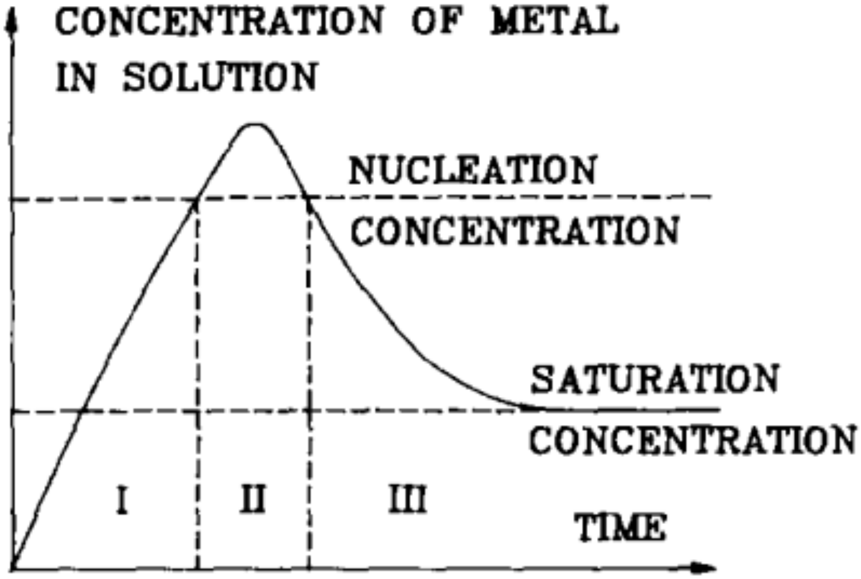

Figure 2.2 La Mer's model for the formation of a homogeneously dispersed system by controlled nucleation and growth[24, 27]

2.2. High-energy Cobalt Carbide (Co_xC, $x = 2$ and 3) Nanomagnets

The cobalt carbide nanomagnet is a novel material that demonstrates properties not found in the original bulk materials. Figure 2.3 shows the crystal structure of Co metal. Co metal has two stable low temperature allotropes, α-Co and β-Co.[28] From the [001] direction, α-Co has a hexagonal closed packed (HCP) structure while β-Co has a face centered cubic (FCC) structure as seen from the [111] direction in the Figure 2.1. The calculated magnetic moments of α-Co and β-Co are 1.63 μ_b and 1.86 μ_b per atom.[29] Both kinds of Co metal are soft phase materials, which means these materials have a relative low coercivity and high saturation magnetization.

Theoretical studies indicate that both Co_2C and Co_3C are both metallic; however, the bulk Co moment is reduced to 1.0 μ_b/atom for the Co_2C and 1.65 μ_b/atom for Co_3C phase, resulting the increase in magnetic moment from Co_2C to Co_3C phase.[30] Figure 2.4 shows the crystal structures of Co_2C (a) and Co_3C (b) materials, respectively. Co_2C has one kind of Co atom; display a layered structure with intervening layer of carbon atoms. It leads to an easy axis along the [001] direction and harder axis along the other direction. However, Co_3C has two kinds of Co atoms. The crystal structure from the [100] direction shows that two zigzag planes of Co atoms are separated by single plane of carbon atom, resulting an easy axis along [100] direction.

However, the Co_3C phase shows the increase of magnetocrystalline anisotropy energy (MAE) to 0.15 – 0.19 meV/Co_3C along other directions. The uniaxial anisotropy of the compound contributes to higher coercivity.

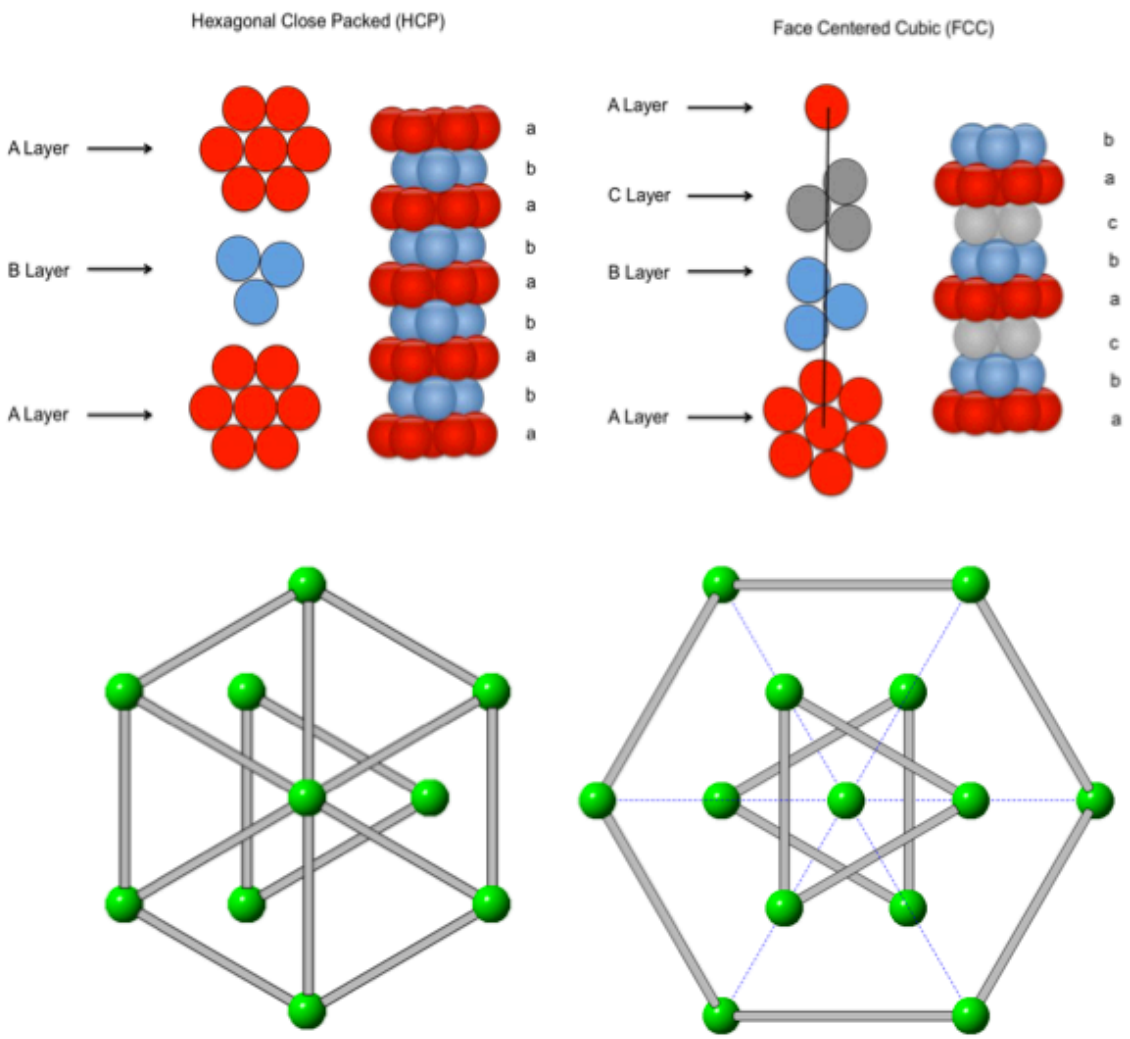

Figure 2.3 Crystal structures of α-Co (left) and β-Co (right)

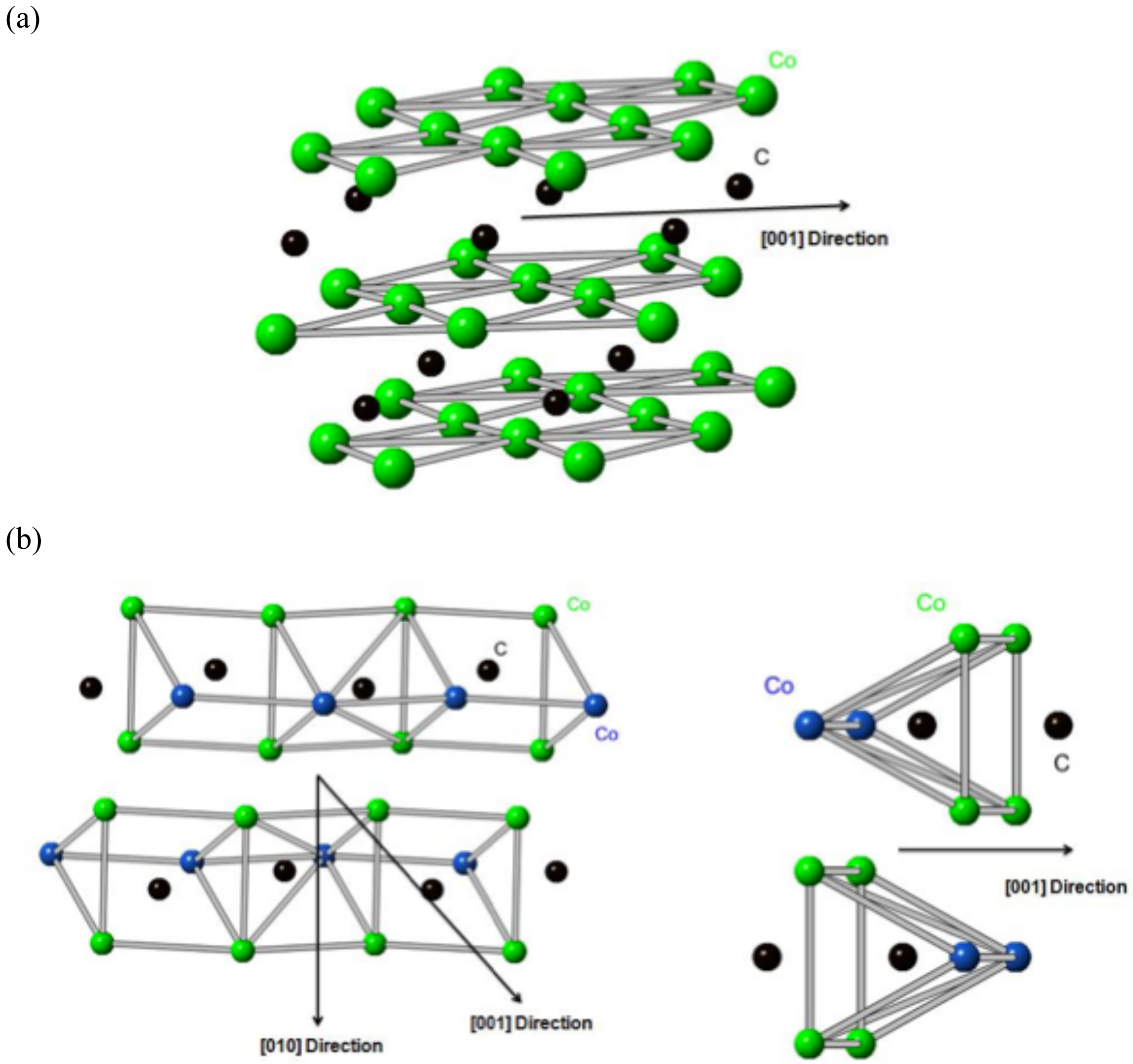

Figure 2.4 Crystal structures of Co_2C (a) and Co_3C (b)

2.3. High-voltage Cathode Materials for Li-ion Battery

Considerable attention has been devoted to cathode materials, which can deliver high energy and power density. Three classes of the cathode materials can be considered: the 3-V cathodes, e.g. MnO_2, $LiFePO_4$, the 4-V cathodes, e.g. $LiCoO_2$, $LiNi_{1/3}Co_{1/3}Mn_{1/3}O_2$, $LiMn_2O_4$, and the 5-V cathodes. Among high-voltage cathode active materials, spinel structured $LiNi_{0.5}Mn_{1.5}O_4$ (LNMO) and olivine Li*M*PO_4 (*M* = Co and Ni) have drawn considerable attention as the 5-V cathodes.[31-32]

The Ni-doped spinel oxide, $LiNi_{0.5}Mn_{1.5}O_4$, has two different crystal structures of the space groups of *Fd-3m* (disordered structure: Mn ions are present in mainly Mn^{4+} and little Mn^{3+}) and $P4_332$ (ordered structure: Mn ions are present in only Mn^{4+}), both providing a 3D network for Li-ion diffusion. It provides access to redox couple (Ni^{3+}/Ni^{4+}) below 4.8 V *vs.* Li. The disordered $LiNi_{0.5}Mn_{1.5}O_4$ spinel was found to have better electrochemical performance than ordered spinel $LiNi_{0.5}Mn_{1.5}O_4$.

The Li*M*PO4 (*M* = Co, and Ni) materials belong to the olivine family of the triphylite lithium orthophosphates where a PO_4^{3-} polyanionic framework surrounds the metal ions. It crystallizes in orthorhombic lattice with either the *Pmna* or *Pmnb* space groups. The olivine-structured orthophosphates Li*M*PO4 (*M* = Co, and Ni) offer both high redox potential. In fact the Co^{3+}/Co^{2+} and Ni^{3+}/Ni^{2+} couples show increasing redox potentials: 4.8, 5.1 V vs. Li^+/Li^0 for Co and Ni, respectively.

Even though they have emerged as the most promising candidates and extensively studied, several issues are still open questions for the practical use: poor cycling life, material instability, storage losses at high temperature, and oxidation of electrolyte at high operating voltage are need to be solved.

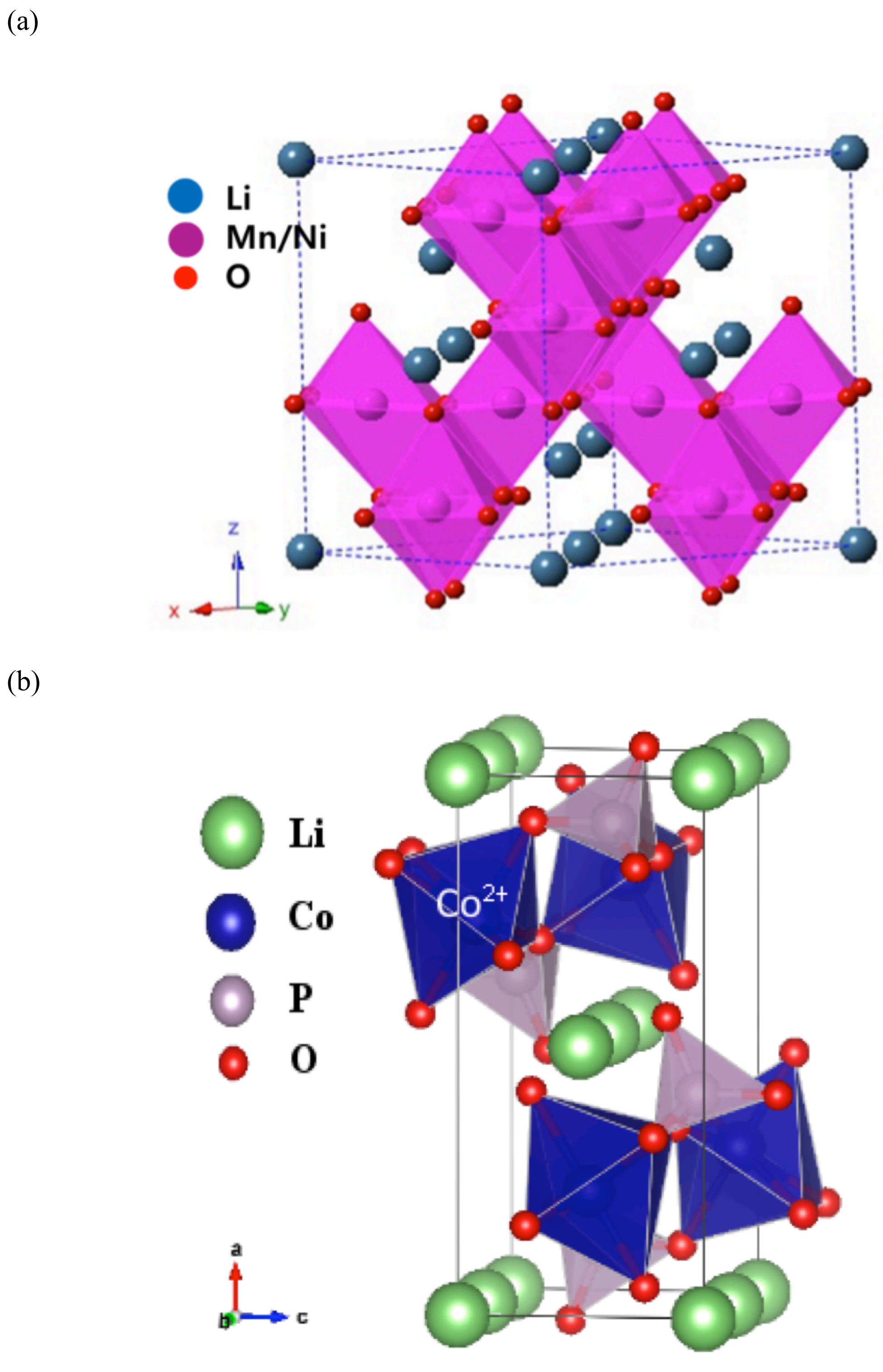

Figure 2.4 Crystal structure of $LiNi_{0.5}Mn_{1.5}O_4$ spinel (a) and $LiCoPO_4$ olivine (b)

Chapter 3. Advanced Characterization Tools

3.1. X-ray Absorption Spectroscopy (XAS)

X-ray absorption spectroscopy (XAS) has made major contributions to research topics of correlation between structure and function of the material due to their element-specific nature and high sensitivity to the local chemical environment. The X-ray energies provided by synchrotron sources are applicable to most elements in the periodic table. In XAS, transitions from core electronic states of the metal to the excited electronic states (LUMO) and the continuum. The former is known as X-ray absorption near-edge structure (XANES), and the latter as extended X-ray absorption fine structure (EXAFS), which probes the fine structure in the absorption at energies greater than the threshold for electron release.[33] X-ray absorption spectra of any material be it atomic or molecular in nature are characterized by sharp increases in absorption at specific X-ray photon energies, which are characteristic of the absorbing element. Figure 3.1(a) shows the sudden increase in the X-ray absorption with increasing photon energy.

XANES spectra provide detailed information about the oxidation state and coordination environment of the metal atoms. The K-edge absorption edge energy increases with increasing oxidation state. Any energy somewhat greater than the LUMO level is carried off as translational kinetic energy. The EXAFS modulations are a direct consequence of the wave nature of the photoelectron, resulting interference owing to scattering of nearby atoms. Thus, the EXAFS oscillations result from the interference between the outgoing photoelectron wave and components of back-scattered wave from neighboring atoms in the molecule.[34]

In general, A narrow parallel monochromatic X-ray beam of intensity I_0 passing through a sample of thickness x will get a reduced intensity I according to the equation:

$$\ln\left(\frac{I_0}{I}\right) = \mu x \qquad \text{(eq. 3.1)}$$

where μ is the linear absorption coefficient, which depends on the types of elements and the density of the material. The absorption coefficient can be detected either directly by measuring the intensities of incoming and transmitted beam (transmission mode) or indirectly by measuring the intensity of the incoming beam and of the decay products such as fluorescent X-rays or Auger electrons (fluorescence or electron yield mode) as shown in Figure 3.1(b).

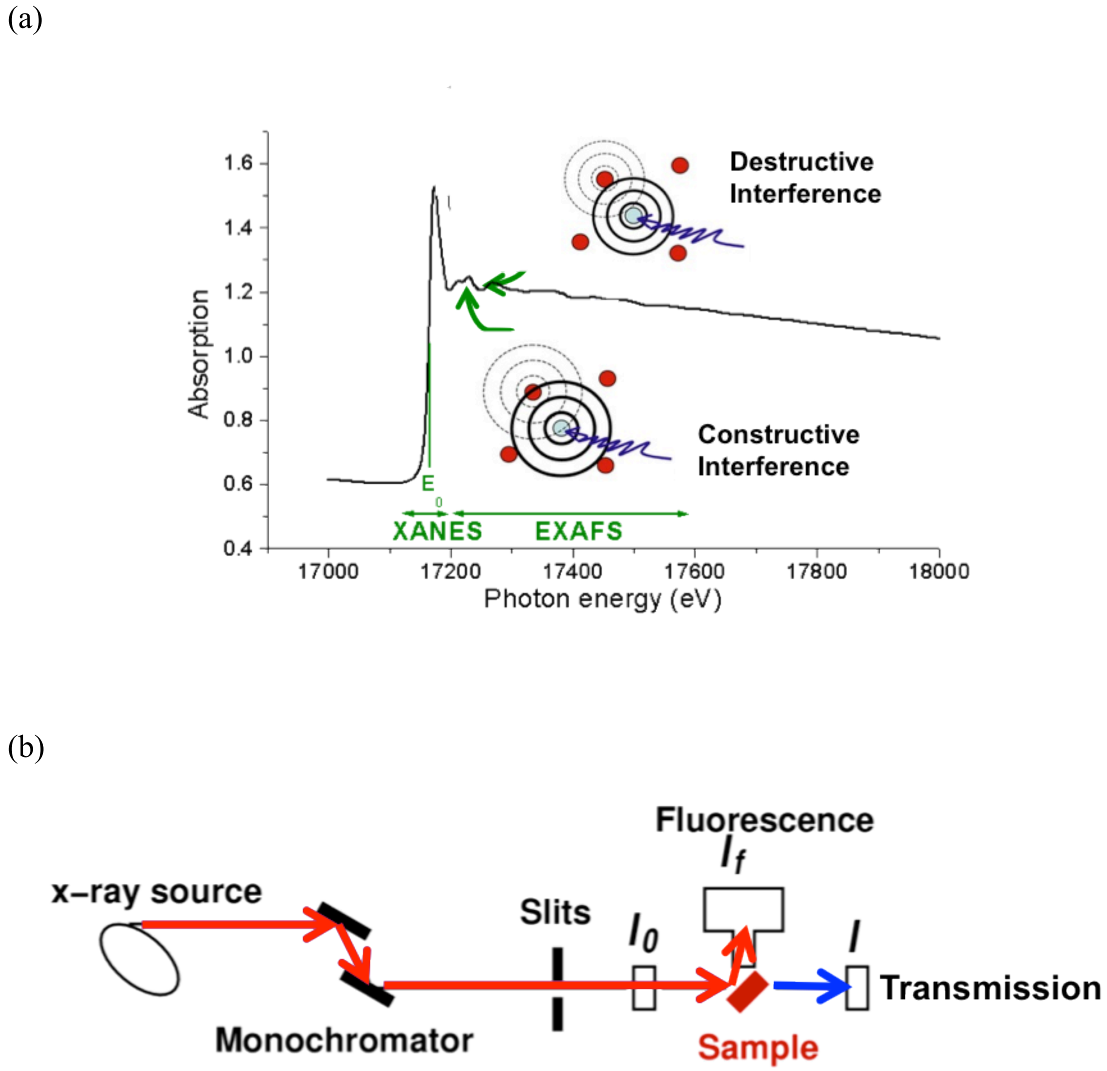

Figure 3.1 (a) X-ray absorption spectroscopy spectra including XANES and EXAFS regions. Inset schemes illustrate the origins of the oscillation in the spectra. (b) Schematic of the experimental setup for the different XAS detection modes

3.2. First-Order-Reversal Curve (FORC) Diagrams

Magnetic hysteresis loops are routinely used to determine the magnetic characterization of materials. However it is difficult to obtain information of coercivity distributions or interactions from the hysteresis loop.

To eliminate some of the ambiguity inherent of conventional hysteresis measurements, Pike *et al.*[35] and Roberts *et al.* developed first-order reversal curve diagrams that can be used to identify and discriminate between the different components in a mixed magnetic mineral assemblage.[36]

A FORC diagram is formed by series of partial hysteresis curves.[37-38] It is measured by saturation a sample in a field H_{sat}, decreasing the field to a reversal field H_a, then sweeping the field back to H_{sat} in a series of regular field steps H_b[39]. This measurement procedure is repeated for different values of H_a to obtain a suite of FORCs as shown in Figure 3.2. The FORC distribution $\rho(H_a, H_b)$ can be defined as the mixed second derivative

$$\rho(H_a, H_b) \equiv -\frac{\partial^2 M(H_a,H_b)}{\partial H_a \partial H_b} \qquad \text{(eq. 3.2)}$$

and plotted in rotated coordinates from (H_a, H_b) to $H_c = (H_b - H_a)/2$ and $H_u = (H_b + H_a)/e$ where H_u corresponds to the distribution of interaction fields, and H_c the distribution of switching fields.[38, 40]

The recent development of FORC diagrams has allowed the detailed investigation of coecivity spectra, interactions, and domain states of fine particle magnetic systems. In addition, this method dramatically increases the speed of the calculation and return results that are identical to the existing slower conventional methods.

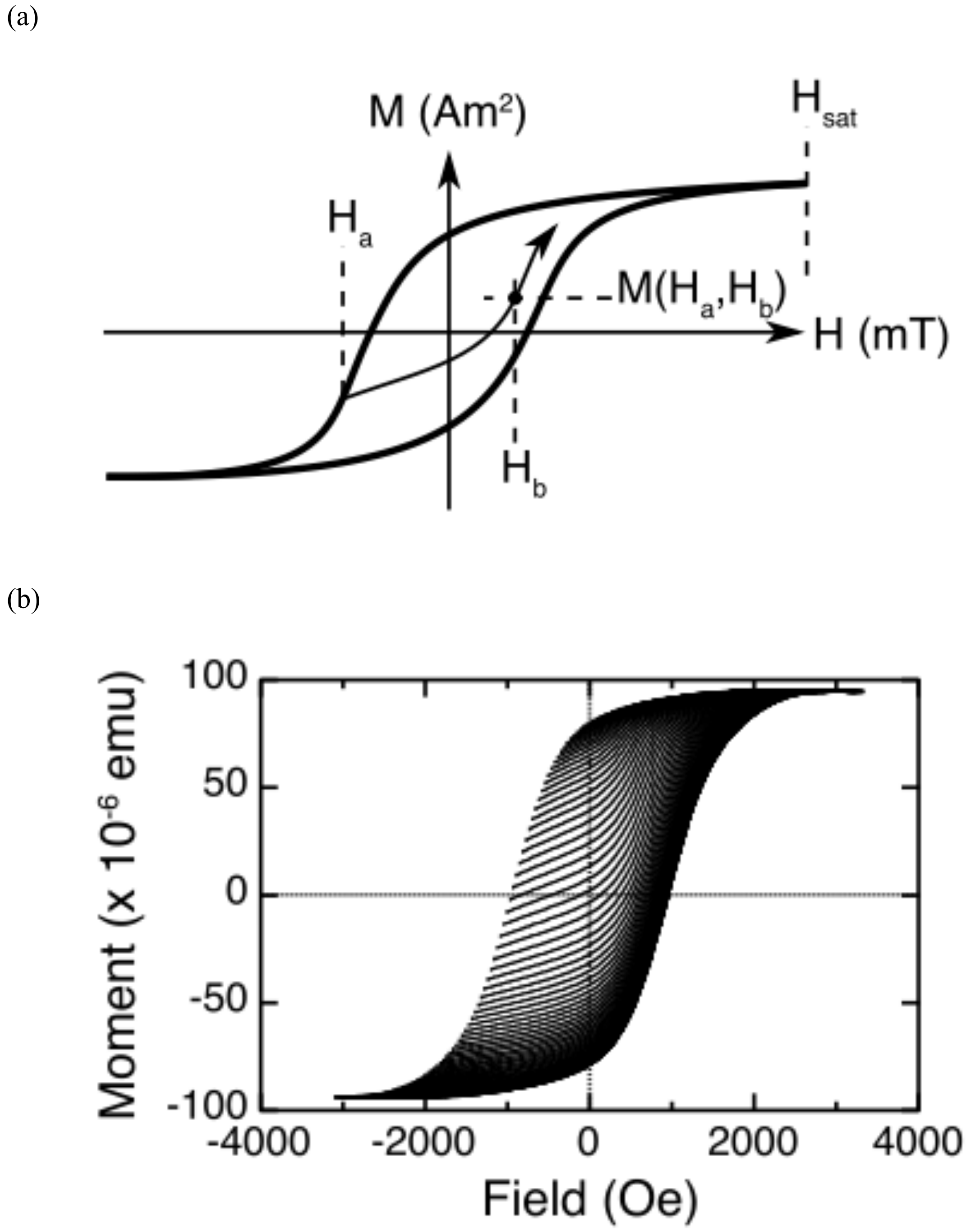

Figure 3.2 Definition and measurement of a single FORC (a) and a set of FORCs (b)[41]

3.3. High Resolution Scanning Transmission Electron Microscopy (STEM)

Probing the local atomic structure, chemical composition and atomic bonding of the battery materials is crucial to understand the complexities of bulk materials and interfaces upon electrochemical reactions. Transmission electron microscopy (TEM), especially with the recently developed techniques such as aberration correctors and fast imaging cameras, has become one of the best techniques to probe these parameters at micron to atomic scale, under both static and in-situ electrochemical operations.

Especially, the scanning transmission electron microscope (STEM) is a very powerful and highly versatile instrument capable of atomic resolution imaging and nanoscale analysis. The basic concept of a STEM is relatively simple — a high-energy electron beam is focused down to a small spot and fired through a thin sample. Signals from scattered electrons and ionized atoms are recorded as the beam is scanned across the sample. Chemical and bonding information along each projected atomic column can be obtained by measuring the energy lost by transmitted electrons to core and valence excitations at each point.[42-43]

The key to this instrument is the formation of an electron probe of atomic dimensions, using the same detectors as a traditional TEM. A bright field detector and an annular dark field detector collect scattered electrons. As the angle of the annular dark field detector is increased away from the transmitted beam, the atomic number dependence of the image contrast is increased. This configuration is often referred to as a Z-contrast or high-angle annular dark field (HAADF) image.[44]

In addition, it can be combined with electron energy-loss spectrometry (EELS) to analyze the energy distribution of inelastically scattered electrons from the specimen. It enables the STEM to characterize complex interface problems in LiBs using analytical and imaging techniques with atomic resolution.

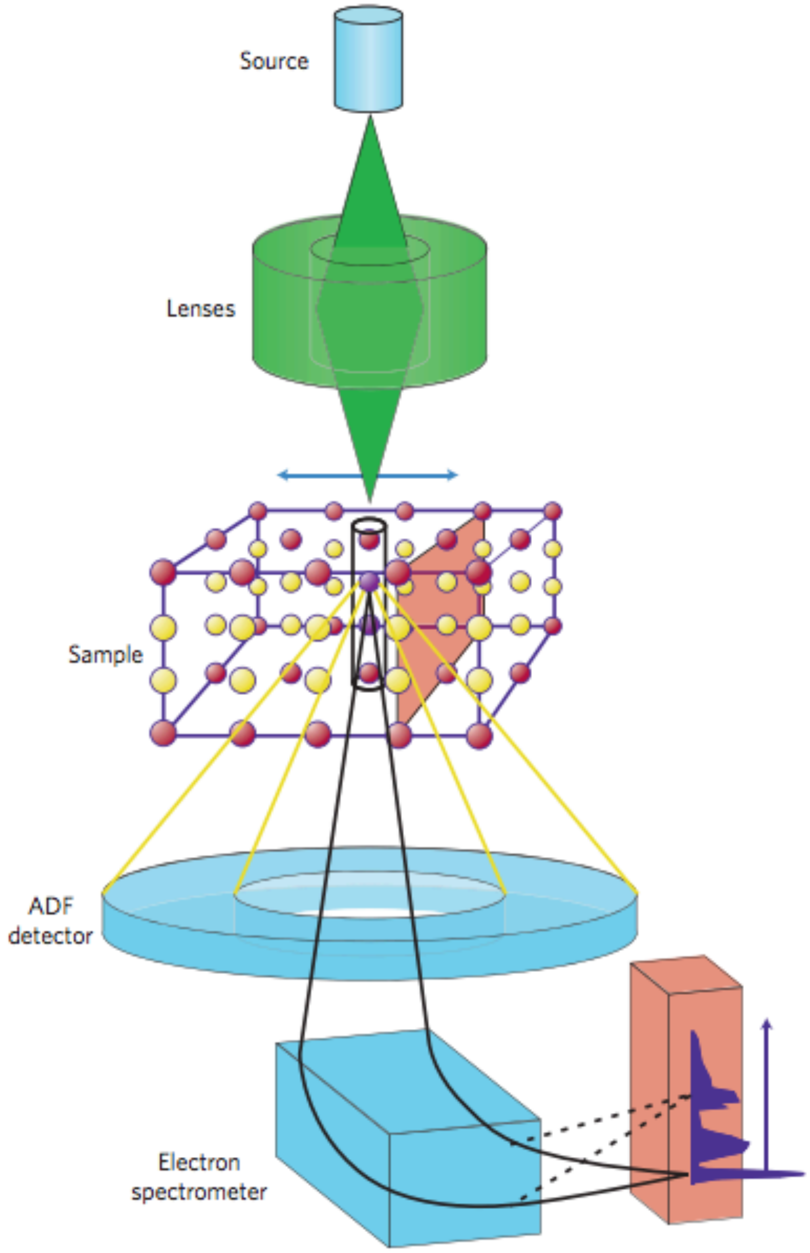

Figure 3.3 Major elements of a scanning transmission electron[43]

Chapter 4. *In situ* Non-aqueous Nucleation and Growth of Next generation Rare Earth Free Permanent Magnets

Using a controllable wet chemical approach, polyol process, we developed a cobalt carbide nanomagnet consisting of an assembly of Co_2C and Co_3C nanoparticles as an alternative to rare earth permanent magnets (PMs). The thermodynamically stable mixed phase cobalt carbide nanoparticels are shown to be acicular in morphology. Their exchange-coupled magnetic interaction possessing high maximum energy product (15.84 MGOe) and room temperature coercivity (2.9 kOe) was confirmed through vibrating sample magnetometer (VSM) and first order reversal curves (FORCs). This nanomagnet has drastically improved their magnetic properties compared to the pure bulk material. In addition, to fully optimize the phase formation and magnetic performance, *in situ* time resolved X-ray absorption spectroscopy (TR-XAS) measurement is applied. By studying nucleation and growth evolution during the polyol process, a clearer understanding of the different phase formation mechanics and magnetic properties was elucidated.

4.1. Introduction

A ferromagnetic material based upon nanoscale cobalt carbide had been recently shown to exhibit unusually large coercivities and energy products, $(BH)_{max}$.[28, 45] This nanoscale cobalt carbide is especially attractive since it provides a rare-earth-free alternative to currently existing high performance permanent magnets. The particular properties realized by this material are highly dependent upon the processing conditions, where coercivity is shown to vary inversely with saturation magnetization. Therefore, developing a fundamental understanding of the effect of those conditions on the material's magnetic properties is critical to translate its initial findings into a realistic candidate, which can compete with rare-earth based magnets. Elucidation and control over nucleation and growth at the nanoscale has been of notable interest over the past decade since many chemical and physical properties can be vastly different than their bulk counterparts.[23, 46] This is particularly true in the case of cobalt carbide, which has an anomalously high magnetic energy density at the nanoscale. Through *in situ* time resolved x-ray absorption spectroscopy (TR-XAS), we show that the nucleation and growth of metastable cobalt carbide via the polyol process proceeds through thermodynamically stable cobalt nuclei up to a critical size; below this critical size, carbide formation is kinetically favored while above that size, metal is the more likely outcome. We also demonstrate how the concentration dependences follow general nucleation and growth theories.

In recent years, there has been extensive research into the fabrication of nanocrystalline metals with uniform size and shape by utilizing several processing techniques such as: thermal decomposition, photochemical reduction, pulsed laser ablation, as well as several chemical synthesis methods.[47-49] In particular, the chemical synthesis methods offer a more efficient route to obtaining nanocrystalline material of tunable size and shape. The polyol process, in which metal salts are reduced by a polyalcohol, has provided a simple and versatile approach to producing well-defined nanoscale materials by effectively separating the nucleation and growth steps.[20, 50-51] Nevertheless, despite many reports elucidating mechanisms for the growth of nanoparticles with enhanced properties, wet chemical synthesis methods remain an art rather than a science. As such, many methods to manufacture nanocrystalline materials have failed to reach the industrial level. A major complication is the variation of the kinetics depending on the synthetic parameters such as a sensitive dependence on pH, metal precursor concentration, temperature, capping agents, and reaction time. To get a precise synthetic system at the level needed for large-scale production, a more detailed study of the nucleation and growth kinetics is needed. *In situ* TR-XAS has been recently proven to be a powerful method to monitor the dynamic structural changes and kinetics during the formation of nanocrystalline materials. As *in situ* techniques are becoming more commonplace in research, reports on the direct monitoring of the nucleation and growth of nanocrystalline metals at room temperature using *in situ* TR-XAS are being developed.[52] Many reports describe room temperature photoreduction of catalytically active materials such as gold colloids, platinum, rhodium, and palladium.[53-57] Despite these recent attempts to monitor the nucleation and growth of nanocrystalline materials, there still lacks direct observation of high-temperature solution based syntheses. This is of particular importance, as most systems used to synthesize nanocrystalline materials require high operating temperatures in addition to complex reaction chemistries.

Here we report the kinetics of nucleation and growth for cobalt metal and carbide nanocrystals formed using a polyol process, with reaction temperatures > 300 °C, using a custom designed reactor. Recently, cobalt carbide nanoparticles have attracted considerable attention as potential rare-earth-free permanent magnets due to their anomalous magnetic enhancement seen at the nanoscale.[28, 45] The nanoparticles offer unusual magnetic properties, a high maximum energy product and coercivity, and these properties change with particle size, morphology and ratio of mixing particles. In order to effectively control these variables and thereby optimize the magnetic properties of the system, a detailed understanding of the effects of changes in synthesis parameters is essential. The important role of surfactants and reaction duration on the crystallographic structure and magnetic properties of cobalt carbide has been illuminated.

4.2. Experimental

All Chemicals were used without any further purification for synthesis of cobalt carbide nanoparticles. In a typical procedure, 0.1 M cobalt chloride ($CoCl_2 \cdot 6H_2O$, guaranteed reagent, Spectrum Chemical) as a cobalt precursor is dissolved in 100 ml of tetraethylene glycol (TTEG; $C_6H_{18}O_5$, Spectrum Chemical), followed by the addition of potassium hydroxide (KOH, ≥ 85%, ACS reagent, Sigma-Aldrich). In a typical cobalt carbide reaction, a cobalt precursor salt ($CoCl_2 \cdot 6H_2O$) and KOH are dissolved in TTEG within the designed *in situ* reactor equipped with stirrer and a reflux condenser and heated to 300 ^{o}C. The reaction was allowed to proceed for up to 2 h.

Powder X-ray diffraction (XRD) patterns of the cobalt metal and carbide nanoparticles were obtained at the X16C high-resolution powder diffraction station at the National Synchrotron Light Source. Retrieved samples for powder XRD were sealed in Lindemann glass capillaries. X-rays of approximately 0.7 Å wavelength were selected by a channel-cut Si (111) monochromator, calibrated for each run with NIST standard reference material 1976 ceramic corundum plate. The sample was spun during data collection to insure good particle counting statistics. Diffracted X-rays were analyzed by a single Ge(111) crystal before a commercial scintillation counter. Measured intensity was normalized to incident flux, measured by an ion chamber in the incident beam path open to the atmosphere. Data were collected in step-scan mode, with collection time typically linearly proportional to diffraction angle 2θ. Rietveld refinements of crystalline phases of Co_2C and Co_3C were performed with TOPAS-Academic software. The non-crystalline structure of the Co sample was modeled with DIFFaX. More details are given in the supplementary information. Morphological features were examined by a transmission electron microscope (TEM) and a field-emission scanning electron microscope (FESEM). SEM images were collected using a Phillips XL30 ESEM at an accelerating voltage of 20 kV. High-resolution TEM images and selected area electron diffraction (SAED) patterns were taken on a JEOL 3000F transmission electron microscope operated at 300 kV. The samples for TEM studies were prepared by drying a drop of the aqueous suspension of nanoparticles on a carbon-coated copper grid (Ted Pella, Redding, CA).

For the time-resolved *in situ* analysis, we developed *in situ* TR-XAS reactor. Figure 4.1 shows schematic drawing of designed reactor cell. The reactor was made with Aluminum (Al) in order to withstand the high operating temperatures along with the high alkaline synthetic conditions required for reaction; the Al reactor also distributes the heat evenly, thereby minimizing local temperature variations. A polyimide film window allows for fluorescence mode analysis. Implanted cartridge heaters connected with a temperature probe and a copper tubing cooling system within the reactor wall help precisely control heating and cooling. The in situ study involves analyzing the x-ray absorption near edge structure (XANES) and the extended x-ray absorption fine structure (EXAFS) of the Co K-edge (7709 eV). We monitor the fluorescent x-ray intensity (I_f)

using a Passivated Implanted Planar Silicon (PIPS) detector, where $\mu(E) = I_f/I_0$. To obtain real time data, each full XAS spectrum was obtained in 100 ms using quick extended x-ray absorption fine structure (QEXAFS) mode at Beamline X-18B of the National Synchrotron Light Source. In this setup, the angle of the crystal monochromator is rapidly oscillated during scans.

Magnetic properties were measured using a Quantum Design-Versalab vibrating sample magnetometer (VSM). The Hysteresis loop was carried out using a maximum magnetic field of 3 kOe, with a field sweep rate of 100 Oe/s. Isothermal remanence magnetization (IRM) plots were collected from 0 to 10 kOe with step of 100 Oe. The direct current demagnetization (DCD) plots were collected in the same manner as the IRM plots, except that the particles were first saturated in a field of -30 kOe. A Henkel plot was then created by $\delta M = (M_{DCD}-M_R+2*M_{IRM})/M_R$. A set of FORCs was obtained by: (1) saturating the sample by applying a field Hmax = 20 kOe, (2) Reducing the field to a return value H_r, where $H_r < H_{max}$, (3) Increasing H to Hmax again and measuring the magnetization M (H, H_r), (4) Repeating steps (2) and (3) for decreasing values of H_r where $H_r > -H_{max}$. The decrease magnetic field step was set to be 100 Oe and then a set of approximately 100 FORCs was generated.

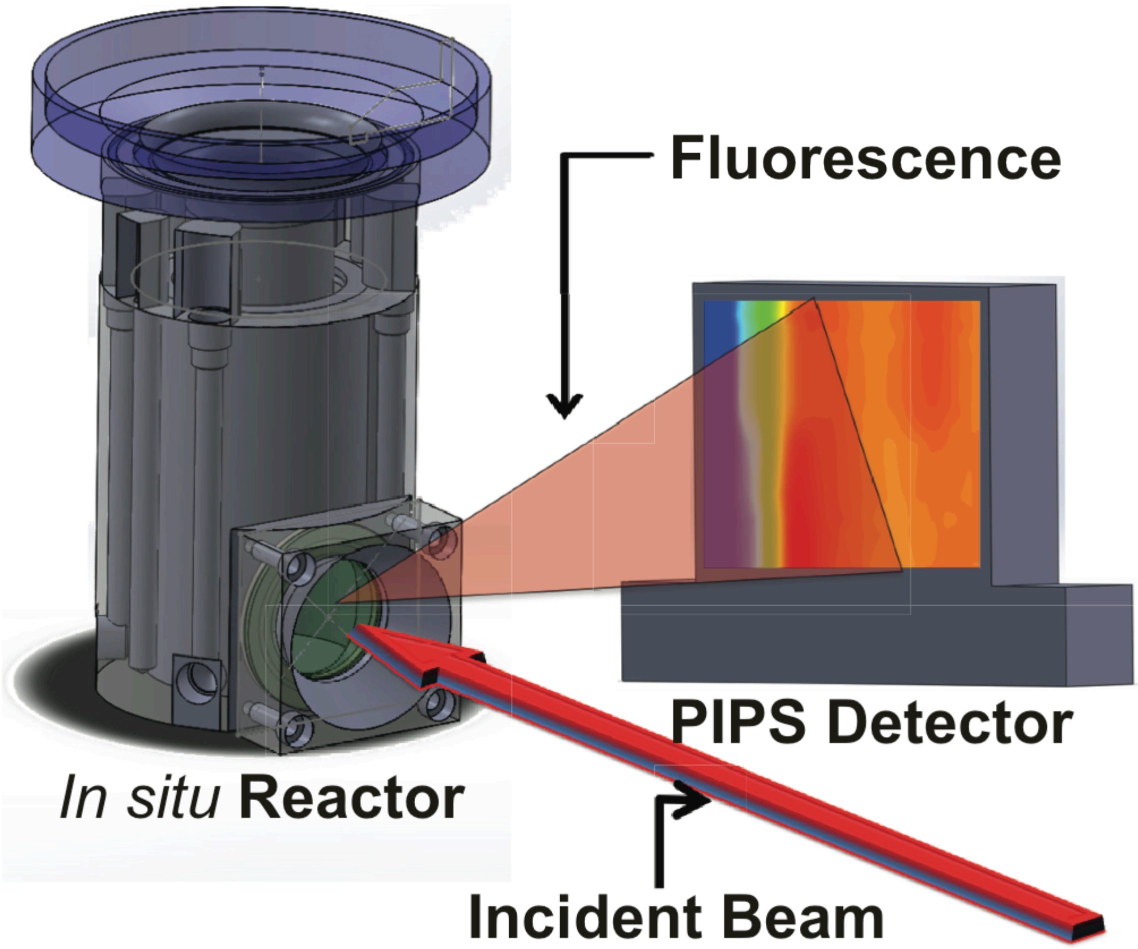

Figure 4.1 Diagram of a designed in situ cell for measurement of time-resolved XAS

4.3. Results and Discussion

4.3.1. Polyol Synthesis of Cobalt Metal and Carbide

A major attraction of the polyol process is the ability to vary the polyalcohol chain length, which in-turn enables control over the operating temperatures. For example, the operating temperature of ethylene glycol is about 198 °C while triethylene glycol is about 285 °C. The operating temperature is merely a few degrees below the boiling point (bp) of the solvent, where the polyalcohol is the most reactive[19, 23-24]. The synthesis of cobalt carbide has been shown to require high operating temperatures, > 300 °C, and thus TTEG was the polyol solvent of choice (bp = 325 °C)[28, 45]. From our previous study[28], we have already shown that the delicate control of the specific carbide phase can be obtained through the addition of various amounts of KOH in the solution. Increasing the hydroxide concentration results in an increase in the polyethylene glycol (PEG) chain length and it can cause variations in the nucleation dynamics. To investigate the concentration of metal salt and reducing agent dependence on the kinetics and formulate a mechanism, nanoparticles were synthesized with two different reaction conditions. Detailed conditions are described in Table 4.1. Varying synthetic parameters resulted in either the formation of the thermodynamically stable Co^0 or the metastable carbide phase. The structural properties of resulted nanoparticles were investigated using *ex situ* synchrotron XRD. In Figure 4.2(a), the powder XRD pattern of Co metal could not be fit as one or more crystalline phases. Bulk Co has a hexagonal close packed (HCP) equilibrium structure at ambient conditions and has a martensitic transition to face centered cubic (FCC) at high temperatures; the subtle energy difference between the two phases leads to a variety of metastable and intergrowth forms[58-59]. DIFFaX[60] was used to model such structures, with parameters adjusted to produce qualitative agreement with the data shown in Figure 4.2(a). In this model, the characteristic dimensions of domains of each type were ~8 atomic layers, and the triangular close-packed layers had a lateral extent on the order of 75 atoms. The nearest neighbor distance within and between layers was 2.50(1) Å. Note the stronger, sharper peaks where FCC and HCP peaks coincide, and the clear broadening and suppression of the HCP (012) and (013) peaks at $2\theta = 27.2°$ and 35.3°, respectively. The fit is not sufficiently good to be regarded as a structural model for the phase, but it is a useful first approximation. All the reflections shown in Figure 4.2(b) can be indexed in the orthorhombic system using the *Pnnm* and *Pnma* space group. Rietveld refinements of crystalline phases of Co_2C and Co_3C were performed with TOPAS-Academic software.[61] The results of the Rietveld crystallographic analysis and crystal structures of the cobalt carbide samples are given in the Table 4.2 and Figure 4.3.

Figure 4.4(a) and (b) depict SEM images of the resultants at two different synthetic conditions. SEM observations show agglomerated particle clusters, consisting acicular or rod-like morphology. An interesting feature of cobalt carbides was that they tended to stack vertically on their edges; therefore, they formed flower-like architectures. To obtain structural information, we conducted high-resolution TEM studies, shown in Figure 4.5(a) and (b). A thin layer of carbon is consistently observed at the edge of the cobalt metal particles (Figure 4.5(c)). A similar observation was found through the micro-Raman measurement (See Raman spectra in Figure 4.6). The HRTEM image in Figure 4.5(a), which was taken near the [001] zone axis, with a 0.22 nm d-spacing value, corresponds to the cobalt metal on the (100) plane. The [010] direction was found to typically lie along the long axis of the Co_3C crystallites in Figure 4.5(b). The lattice spacing was also determined to be about 5.0 Å along that direction. Aggregated nanometer-scaled crystals were observed with magnetic domain boundaries through Lorentz microscopy (in Figure 4.7). The inset in Figure 4.5(b) shows a typical SAED pattern recorded by directing the electron beam perpendicular to the flat faces of an individual particle. The SAED pattern shows the corresponding diffraction pattern, indexed to the [0 1 0] direction of Co_3C.

Table 4.1 Description of the conducted experiments

Reaction	KOH (g)	CoCl2 (g)	$[Co^{2+}]/[OH^{-}]$
Cobalt Metal	0.2	0.6	0.69
Cobalt Carbide	0.8	0.6	0.17

Table 4.2 Crystallographic details of the sample Co carbide

Phase	Co_2C
Space Group	*Pnnm* (#58)
Lattice Parameters (Å)	*a* = 4.371(1), *b* = 4.478(1), *c* = 2.881(1)
Mass Fraction	28(1)%
Atomic positions	Co: 4*g* 0.268(2), 0.346(1), 0
	C: 2*a* 0, 0, 0
Minimum bond length (Å): Co-C	1.89(1)
Co-Co	2.46(1)
Phase:	Co_3C
Space Group	*Pnma* (#62)
Lattice Parameters (Å)	*a* = 5.000(1), *b* = 6.739(2), *c* = 4.465(1)
Mass Fraction	72(1)%
Atomic positions	Co1: 8*d* 0.192(1), 0.063(1), 0.329(1)
	Co2: 4*c* 0.030(1), ¼, 0.836(1)
	C: 4*c* 0.960(1), ¼, 0.378(1)
Minimum bond length (Å): Co-C	1.73(2)
Co-Co	2.46(2)
Scherrer size parameter (restrained common to both phases)	220(10) Å
X-ray wavelength	0.69978(3) Å
R_{wp} [a]	5.06 %
R_{exp} [a]	1.87 %
GOF [a]	2.70

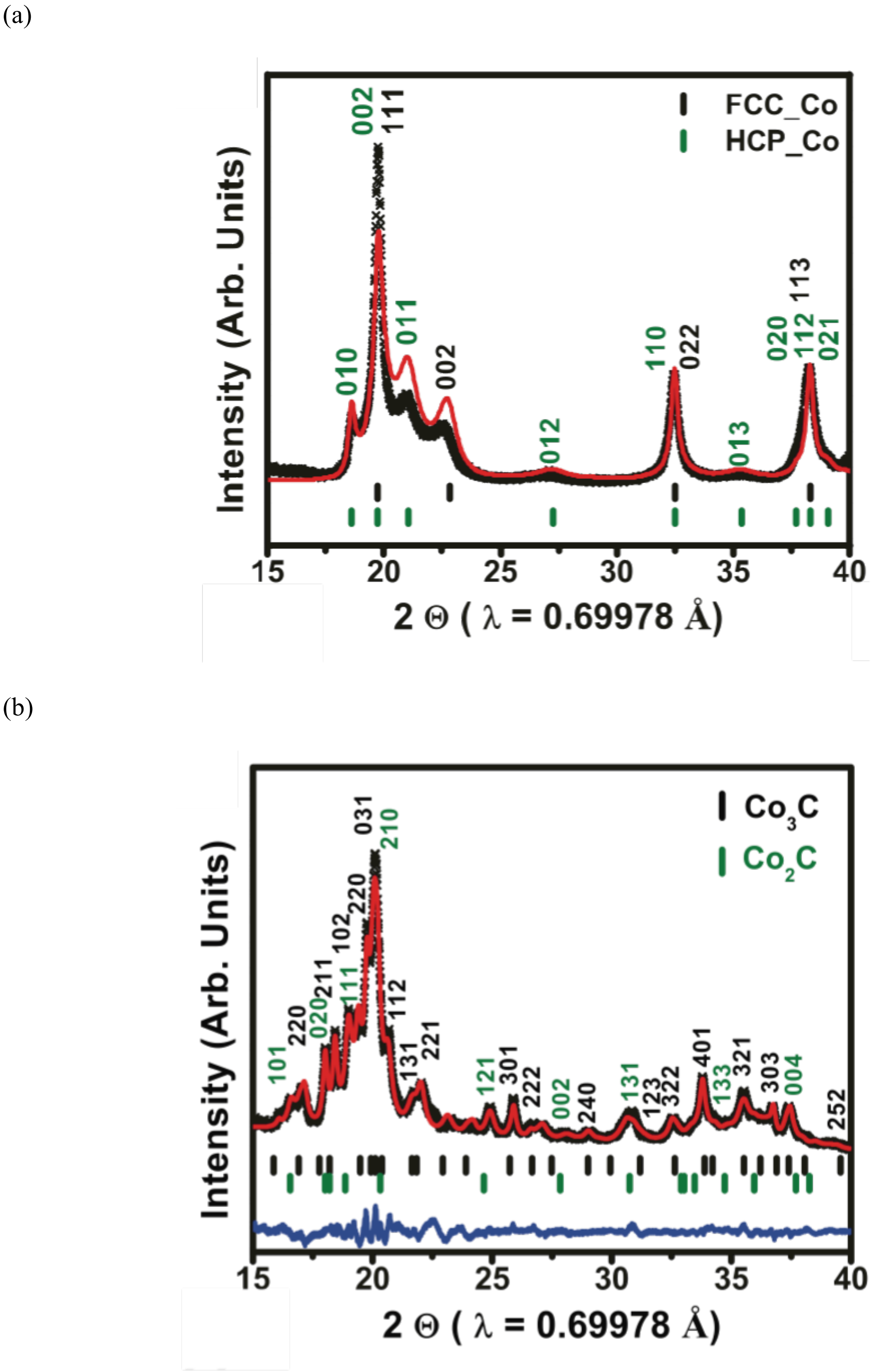

Figure 4.2 High-resolution powder x-ray diffraction patterns for Co metal (a) and carbide (b)

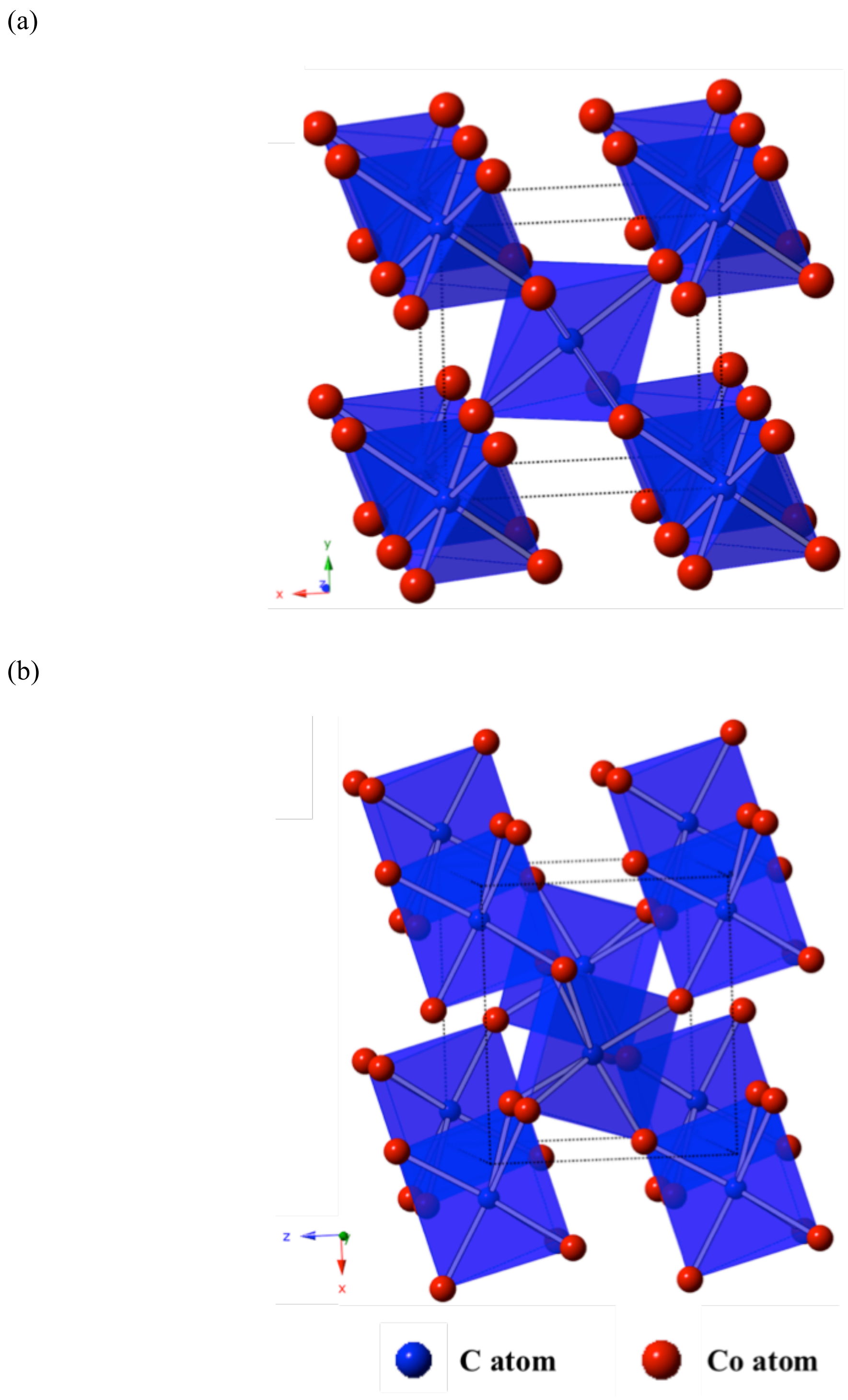

Figure 4.3 Crystal structures for Co_2C (a) and Co_3C (b)

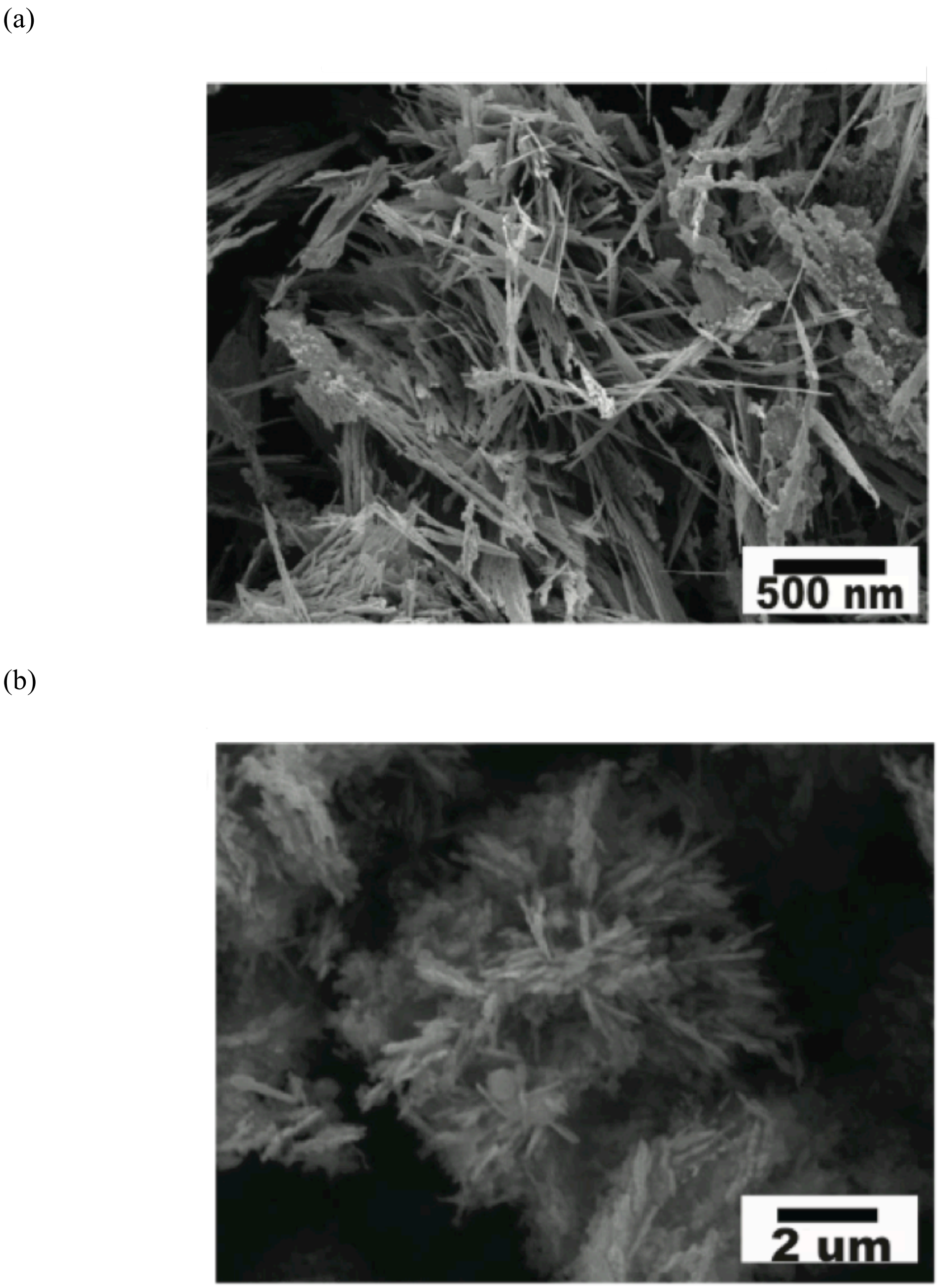

Figure 4.4 Scanning electron micrographs of Co metal (a) and carbide (b)

(a)

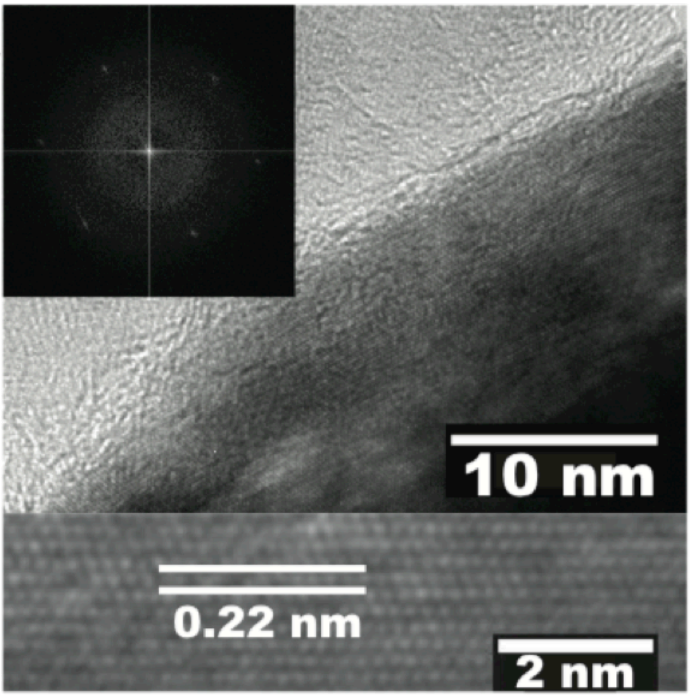

(b)

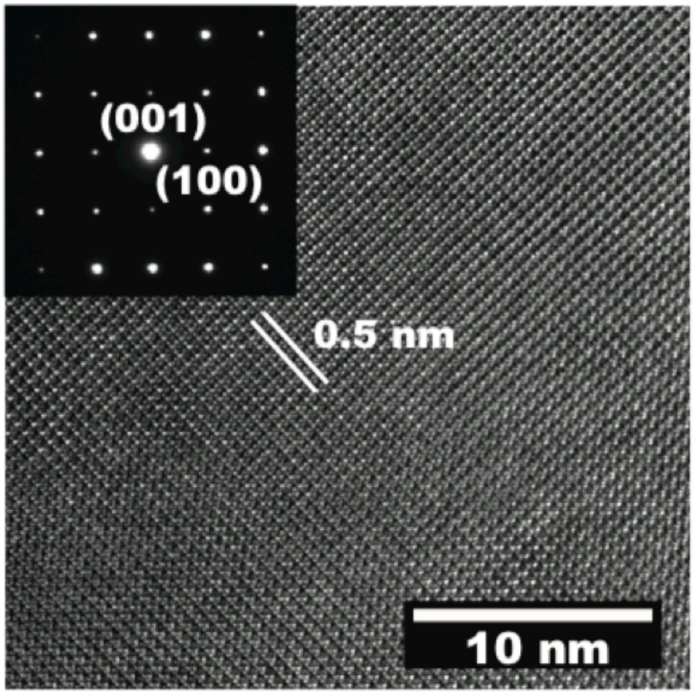

Figure 4.5 High-resolution TEM images and insets of SAED patterns for representative of Co metal (a) and carbide (b)

(a)

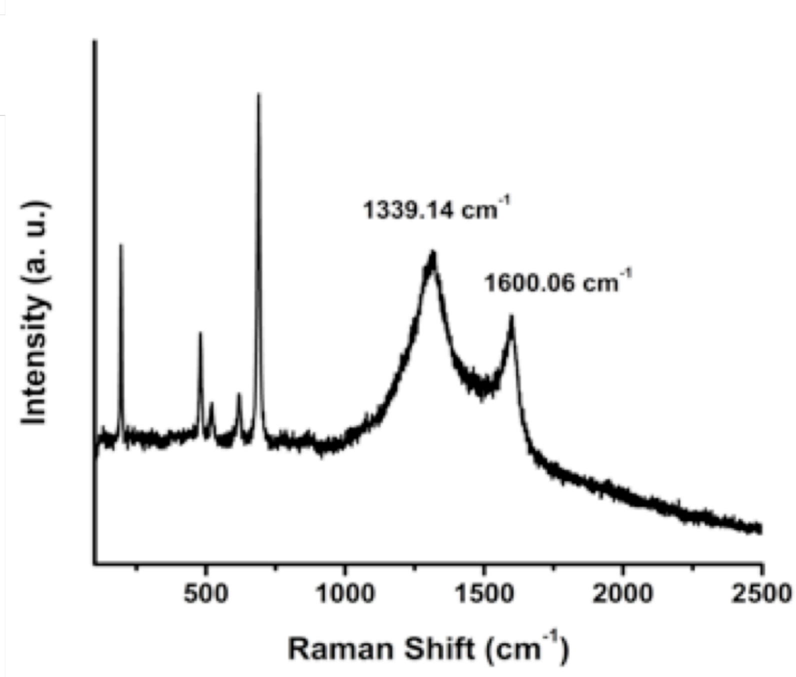

(b)

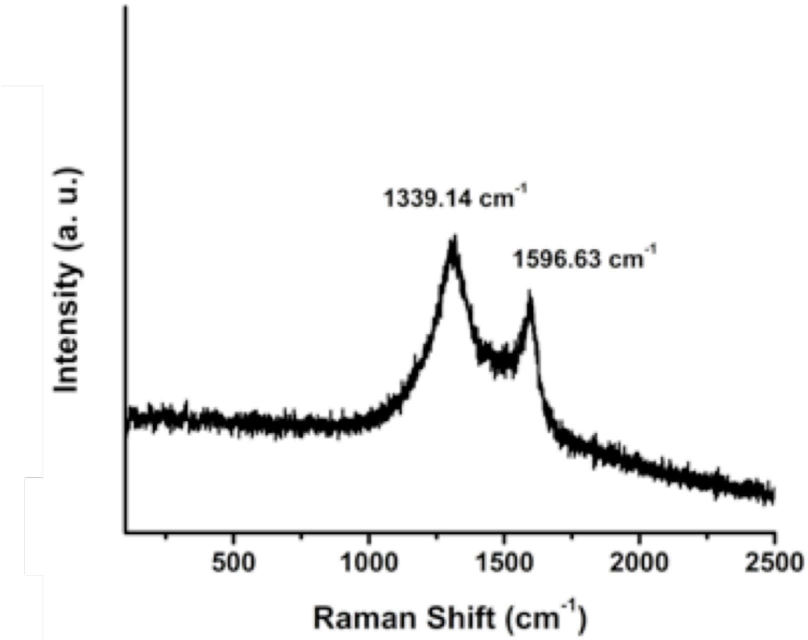

Figure 4.6 Raman spectra of the Co metal (a) and carbide (b) showing two types of D-G bands

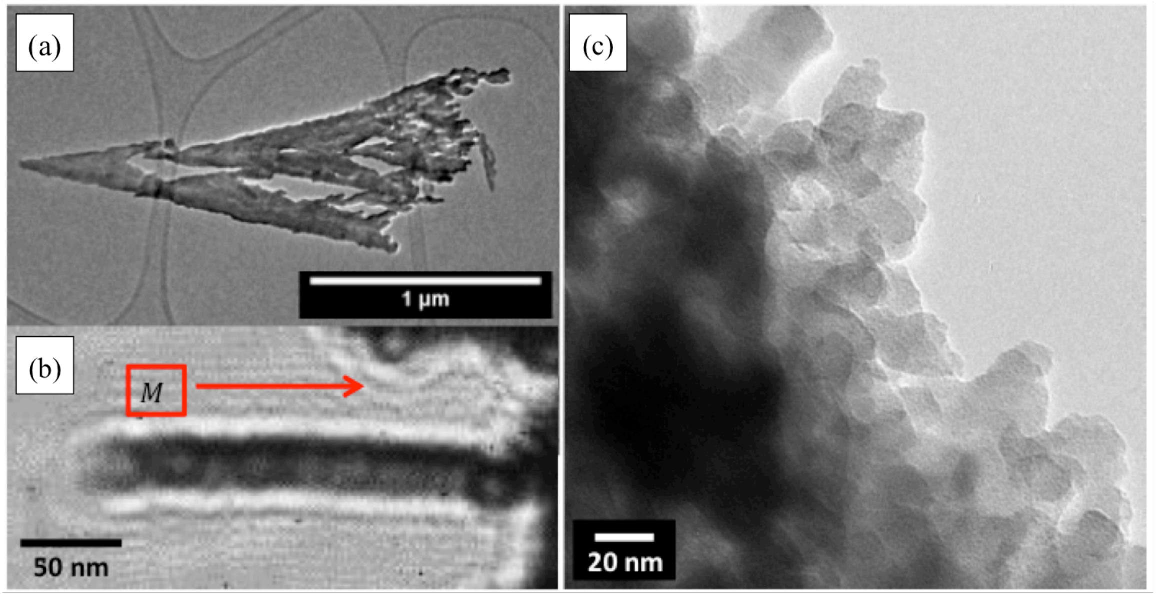

Figure 4.7 (a)-(c) Lorentz micrographs of Co carbide particles

4.3.2. Magnetic Properties of Cobalt Metal and Carbide

The magnetic behaviors of synthesized cobalt carbide nanoparticles were investigated and compared with synthesized cobalt metal. While the cobalt metal shows a high saturation magnetization with a low coercivity, the carbide sample has a high coercivity (~2.9 kOe). That leads a 70% increase in the energy product ($BH_{max}^{Co-carbide} \approx$ 15.84 MGOe) as shown in Figure 4.8. Henkel plots (in Figure 4.9(a) and (b)), which can be obtained from Isothermal remanent magnetization (IRM) and direct current demagnetization (DCD) tests, were carried out to better investigate the interaction mechanism and associated strength in these two systems based on Stoner-Wohlfarth theory: $\delta M=(M_{DCD}-M_R+2*M_{IRM})/M_R$[62-63], where M_R represents the remanent magnetization. Both the cobalt metal and carbide show a positive δM value, which refers to a dominant short-range exchange interaction. The highest intensity peak appears around the coercivity field, where the angle $\emptyset$ between two single magnetic particles becomes largest[64]. In Figure 4.10(a) and (b), first order reversal curves (FORCs) provide information pertaining to the switching field distribution and give insight into interaction mechanisms between particles in the system[35-36]. FORC contours are generated by calculating the second derivative, $\rho(H,H_r) \equiv -\frac{1}{2}\frac{\partial^2 M(H,H_r)}{\partial H_r \partial H}$. The local coercivity field (H_c) and bias interaction field (H_u) are obtained by a coordinate transformation: $H_c = (H - H_r)/2$ and $H_u = (H + H_r)/2$, where the H_r is the coercivity of the remanence. For assemblages of randomly orientated, non-interacting, single domain (SD) grains, the FORC diagram displays an asymmetric "boomerang" shape contour line with the central intensity peak[36]. The negative deviations of ρ on the H_u axis reveal that exchange interaction is dominant in both cobalt metal and carbide systems, which are in accordance with the Henkel plot results. The non-uniform and spread tails of the switching field distribution on the H_c axis in cobalt metal provides evidence of asynchronous reversal behavior caused by polydisperse grain sizes and anisotropy within the system[65]. However, the cobalt carbide system has a single-phase magnetization reversal, at 3 kOe, indicating an exchange-coupled system with a narrow size distribution.

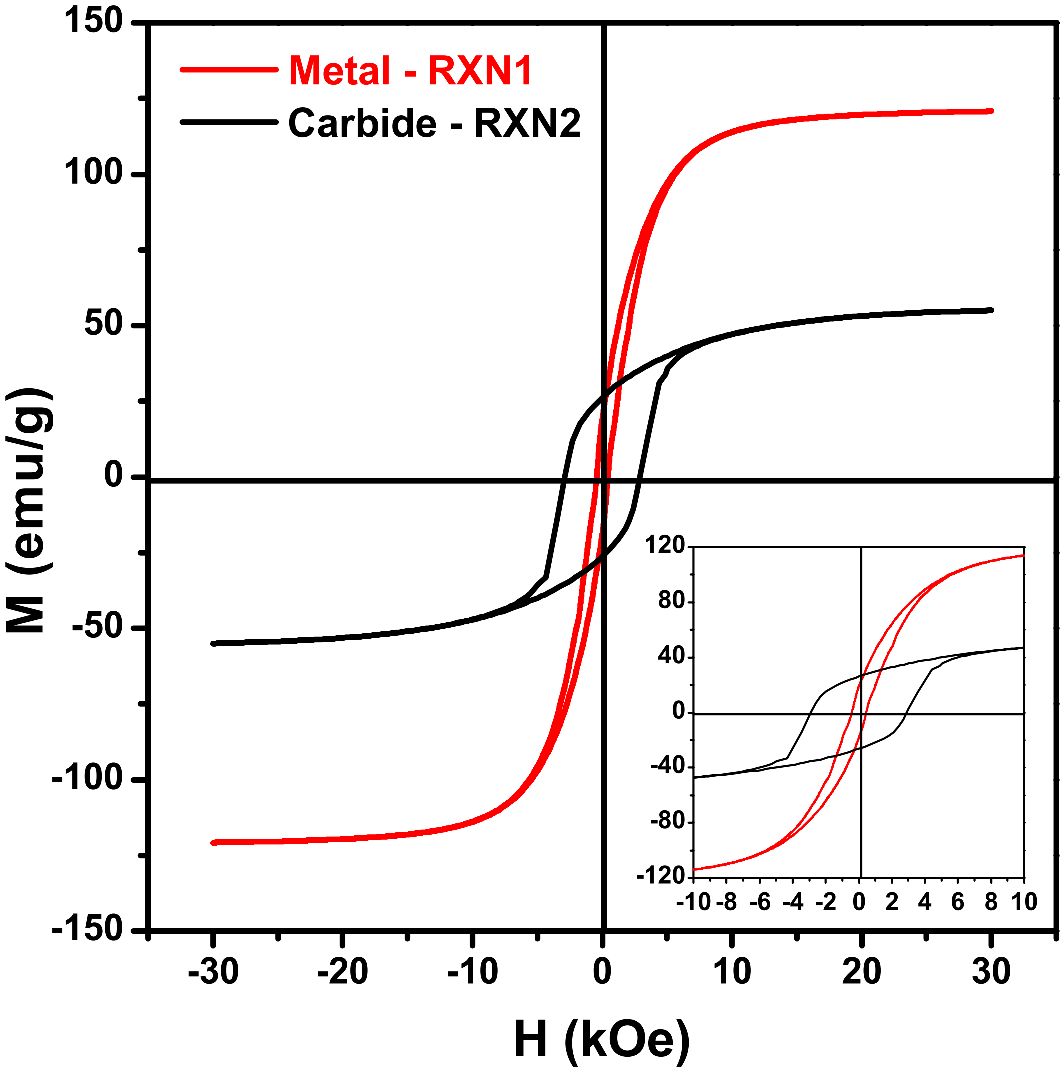

Figure 4.8 Hysteresis loops obtained from a VSM measured operating at room temperature for Co metal (red) and carbide (black) nanoparticles

(a)

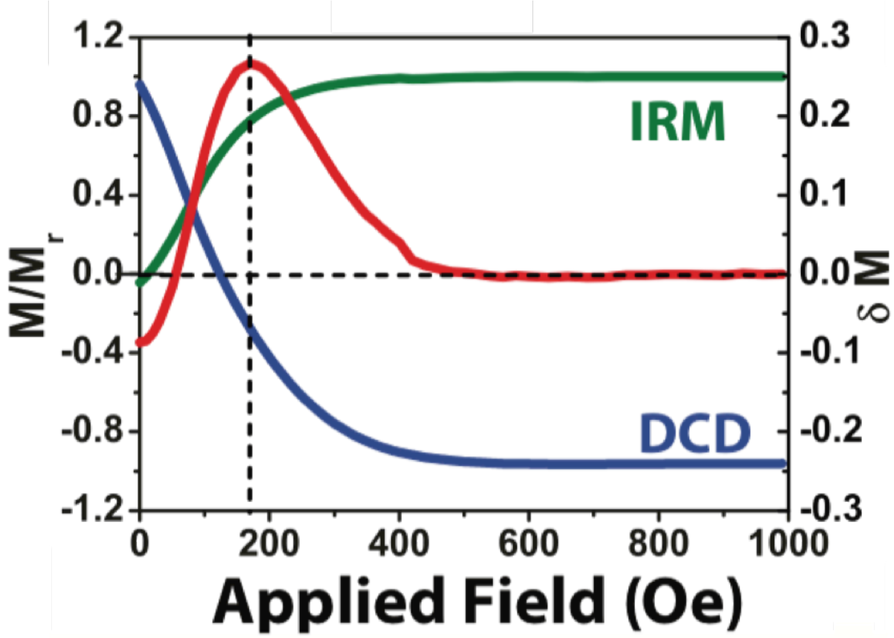

(b)

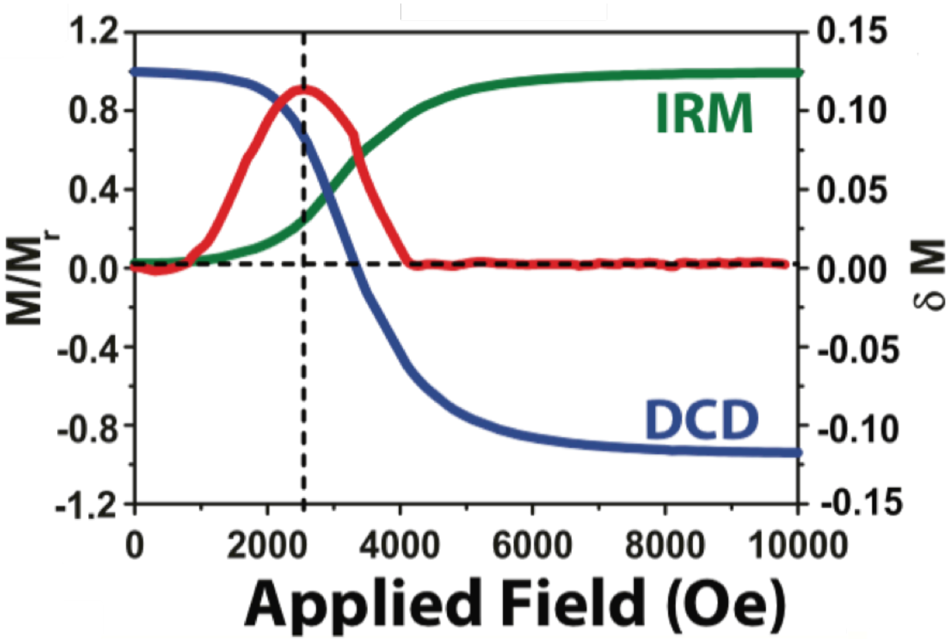

Figure 4.9 The isothermal remanence (IRM), DC demagnetization (DCD) remanence curves, and Henkel plots for Co metal (a) and carbide (b)

(a)

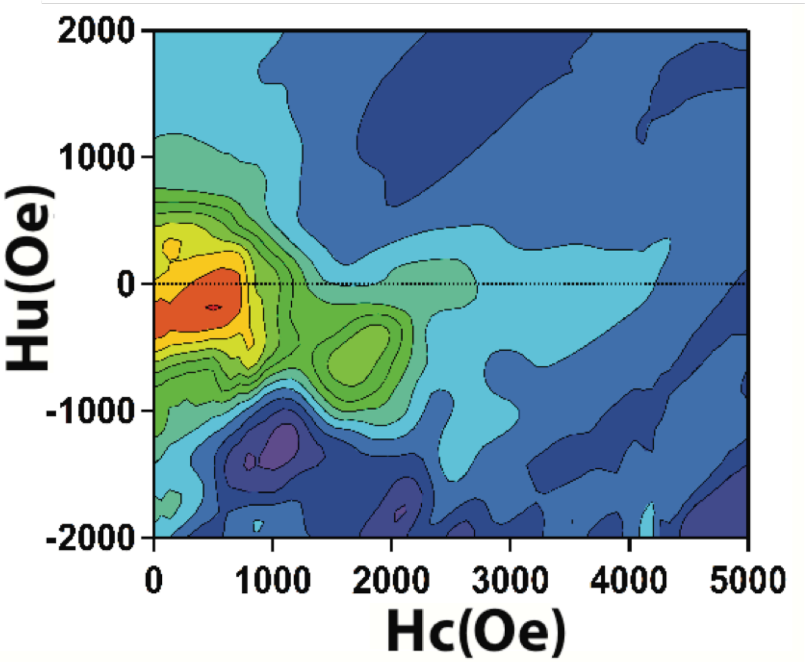

(b)

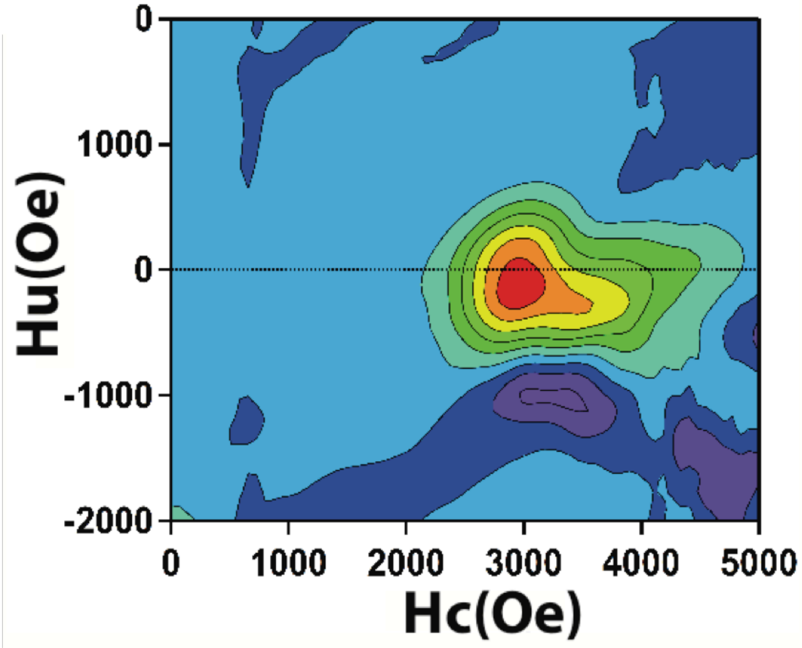

Figure 4.10 First-order reversal curve (FORC) diagrams for Co metal (a) and carbide (b)

4.3.3. Nucleation and Growth Model by In situ TR-XAS Measurement

To reveal how the synthetic conditions affect nanoparticle synthesis, the dynamics of the cobalt metal and carbide formation were investigated as a function of reaction time. In order to analyze the formation kinetics by using the appropriate rate equation, we proposed the overall reaction mechanism as shown in Figure 4.11, where the metal nanoparticle formation is a two-step process[23]. The initial reaction rate, k_1, designates the ligand exchange forming the cobalt-glycolate species, which occurs once the metal salt precursor is dissolved in the polyol. The reaction rate, k_2, covers the progressive conversion of cobalt-glycolate to Co^0 utilizing the electrons from the carbon center to form a double bond with the oxygen atom[23]. The time evolution for Co K-edge *in situ* TR-XAS spectra during polyol process for total reduction time of 100 min are plotted in Figure 4.12(a) and (b) using a color scale for the spectrum intensity. To clearly show the reduction of Co^{2+} to Co^0, selective XANES and EXAFS spectra are presented in Figure 4.13(a) and (b). As presented in XANES spectra, the magnitude of Co^{2+} absorption around 7715 eV largely disappeared after intermediate state and shifted towards lower energy in both reactions, corresponding to metallic Co^0 by the polyol process. It can be also confirmed through the EXAFS spectra of the *in situ* reactions that the absence of the Co-Cl contribution and the presence of the Co-Co contribution for the final phase are consistent with the reduction of Co^{2+} to Co^0. By checking the white line intensity μ (E_{CoCl2}=7709 eV) and intrinsic peak - $E_{Co\text{-}Metal}$=7757 and $E_{Co\text{-}Carbide}$=7784 eV attributed primarily to Co-Co and Co-C bond respectively (See Figure 4.14 and 4.15) - quantitative kinetic values were analyzed from the *in situ* TR-XAS spectra. Concentration data as well as the fitting curves derived from reaction models are shown in Figure 4.16. The induction period is observed for the first 1250 and 500 s in Figure 4.16(a) and (b), respectively. This duration corresponds to the accumulation of the critical concentration of Co atoms necessary for the nucleation to occur in the original LaMer model[27]. Distinctly, in Fig. 4.16(b), the rapid onset of the nucleation (~ 500 s) resulted in a smaller induction period over the cobalt metal formation. The formation of cobalt metal and carbide phases shows a strong dependence on the induction time within the nucleation stage. To obtain detailed rate constants from the raw data curve fitting, the Avrami-Erofe'ev (AE)[66-67] and Finke-Watzky (FW)[68] models were applied. The kinetic studies of the solution based nucleation and growth of crystals are often described by the AE model, expressed as mole fraction term:

$$\alpha = 1 - \exp\left[-(kt)^n\right]$$

On the other hand, the FW 2-step model[68] is able to provide quantitative rate constants corresponding to the nucleation and growth process respectively. The FW 2-step model can be described without explicit concentration-dependence terms[53];

$$\alpha = 1 - \frac{k_1 + k_2'}{k_2' + k_1 exp[(k_1 + k_2')t]}$$

With these models, we determined the reaction rates via least squares fitting of the concentration data derived from *in situ* TR-XAS (Table 4.3). It is found that the induction period is drastically shortened with a decrease of $[\mathrm{Co}^{2+}]/[\mathrm{OH}^-]$. Our fitting results clearly show a difference in nucleation rate, k_1. Comparing k_1 of the cobalt metal and carbide formation, k_1^{carbide} is much larger than k_1^{metal}. It has been shown that hydroxyl ions provide nucleation sites for the formation of metallic particles.[69] This fact demonstrates that more seeds will be formed since there are enough nucleation sites, leading to the very rapid nucleation rate at high concentration of hydroxyl ions, which results in much smaller particle size. A critical size of Co^0 nuclei is essential to forming the desired carbide phase, as we believe that the formation of cobalt carbide is due to a surface reconstruction/diffusion of C atoms into the Co structure by Fisher-Tropsch reaction with the source of carbon monoxide being the aldehyde formed during the reduction of cobalt[70-73]. In Figure 4.17, the graph depicts the hypothesized pathways as described in the nucleation and growth kinetic model based on the fitted parameters. The plateau region, observed in Fig. 4.16(b), supports our previous assessment that once the critical nanosized Co nuclei are formed, they immediately act as a catalyst, whereby the carbon monoxide is catalytically decomposed to C atoms. This reaction permits carbon diffusion into the Co interstitial sites through a surface diffusion mechanism and hence results in formation of cobalt carbide[28, 45]. Therefore, the cobalt nuclei should have a critical maximum size, which can be achieved with a fast enough nucleation rate to enable them to fully incorporate carbon into their structure. Recently, it is reported that when two final phases, Co metal and carbide in our case, compete from the same dissolved precursor at the beginning of the reaction, the phase, with the lower energy barrier, prefers to form more rapidly as the rate of nucleation is proportional to $e^{-\Delta G/k_B T}$, where ΔG is the Gibbs free energy, k_B is the Boltzmann constant and T is temperature[74]. We believe that the fast rate of nucleation helps to form cobalt carbide phase, which has a lower energy barrier than metal.

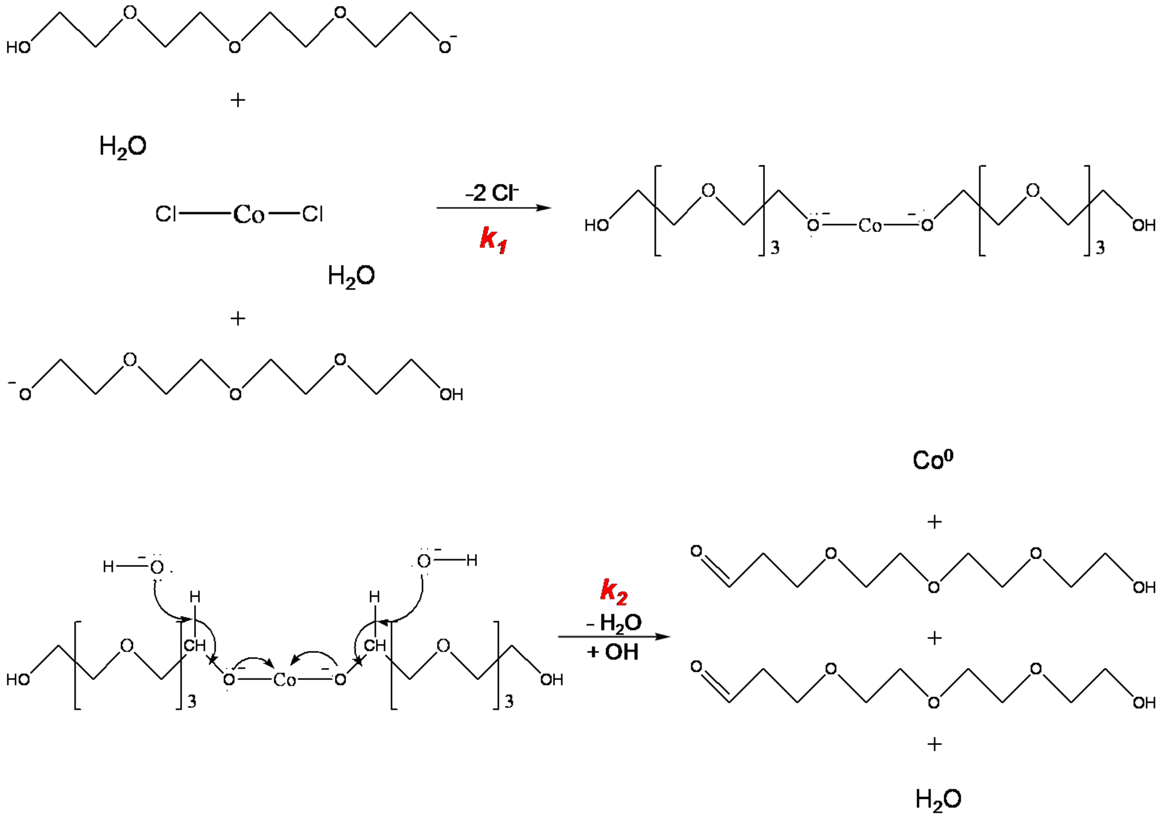

Figure 4.11 Proposed mechanism for the formation of Co nanoparticles synthesizes from TTEG solution of $CoCl_2$ in the presence of KOH

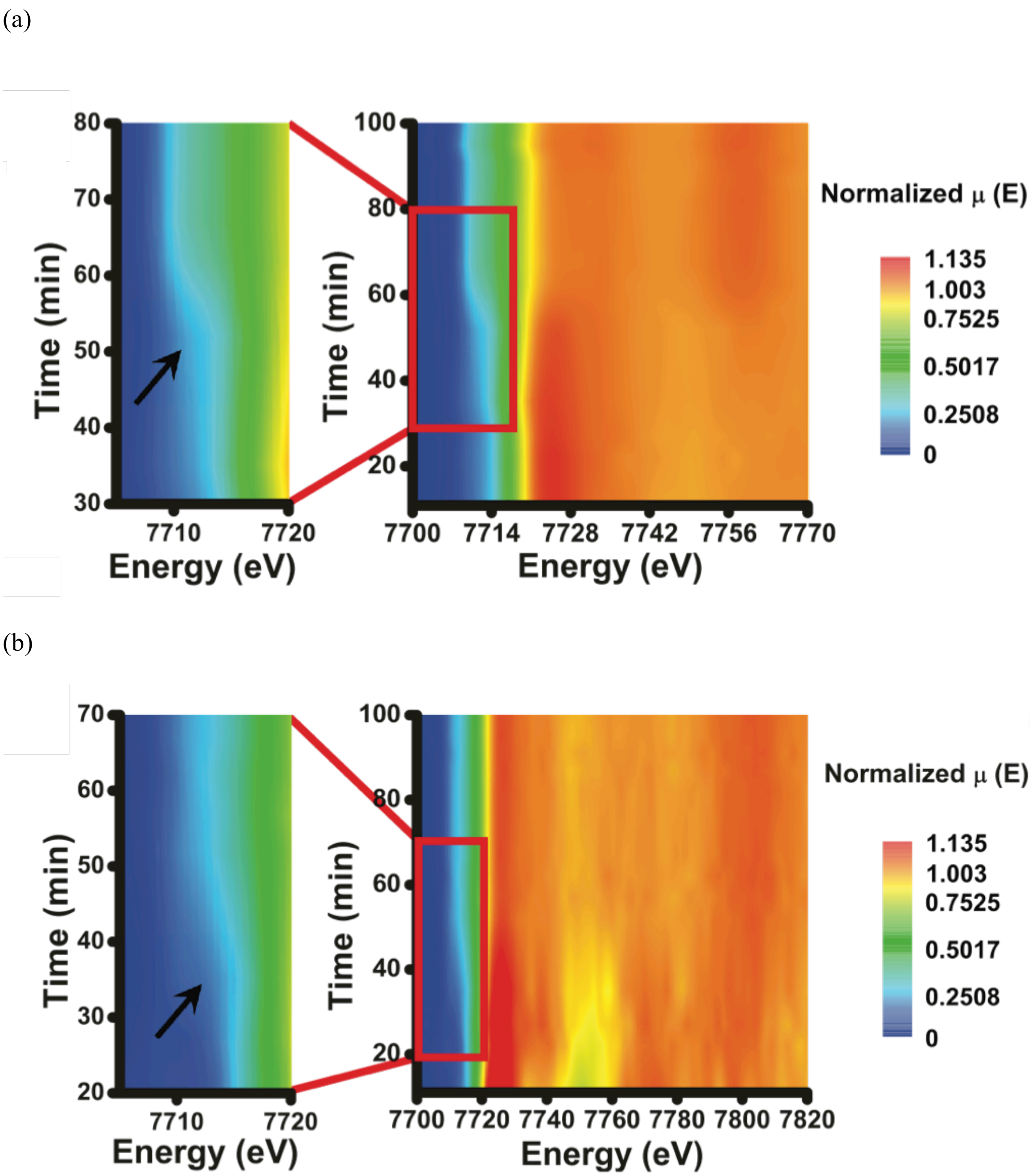

Figure 4.12 (a) Time evolution as a function of the reduction time for Co K-edge XANES spectra and color scale for the spectra intensity for Co metal formation. (b) Time evolution as a function of the reduction time for Co K-edge XANES spectra and color scale for the spectra intensity for Co carbide formation

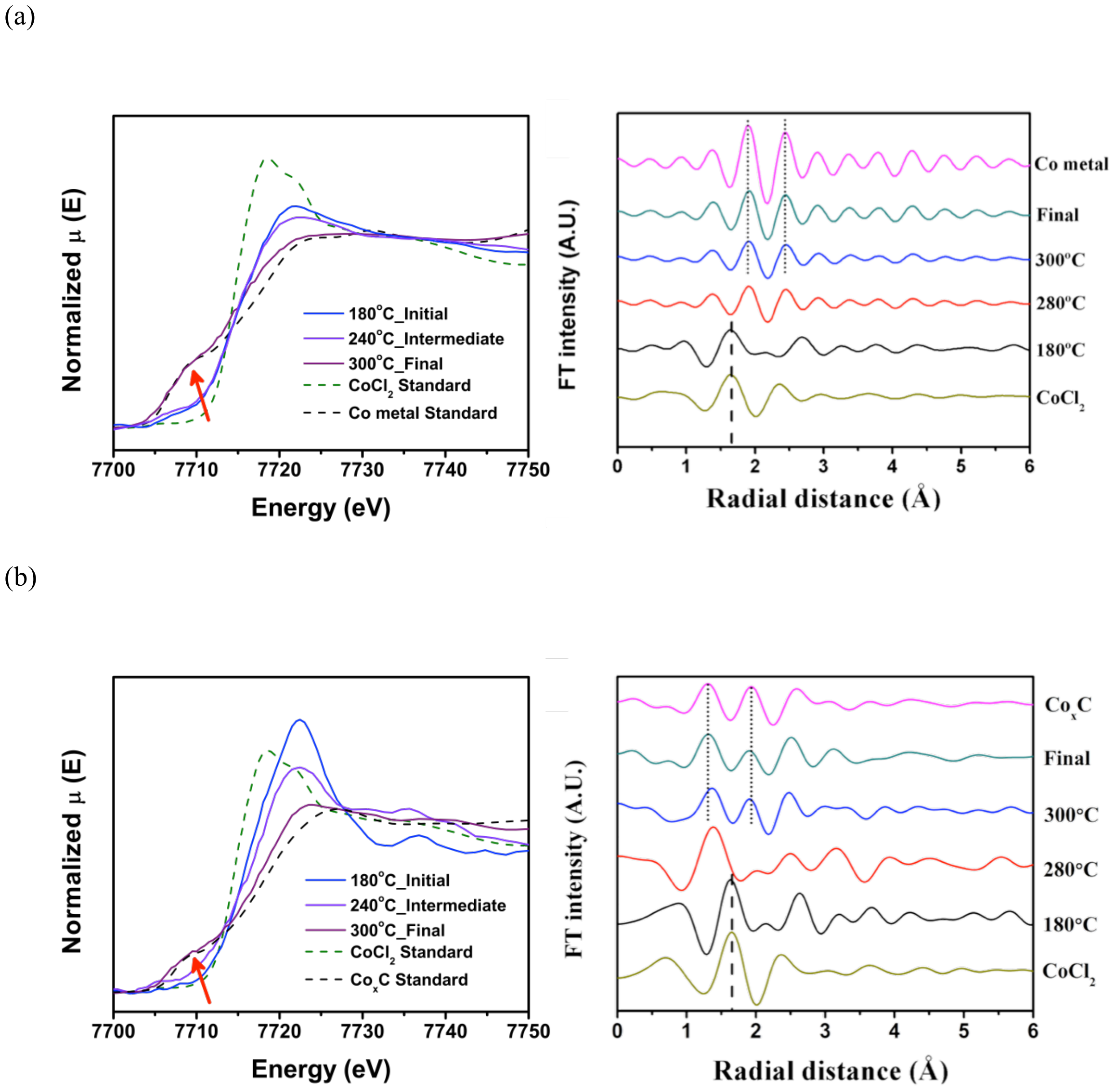

Figure 4.13 XANES and EXAFS spectra at Co K-edge of initial, intermediate and final state during in situ Co metal (a) and Co carbide (b) reactions including $CoCl_2$, Co_xC and Co metal powder standards

(a)

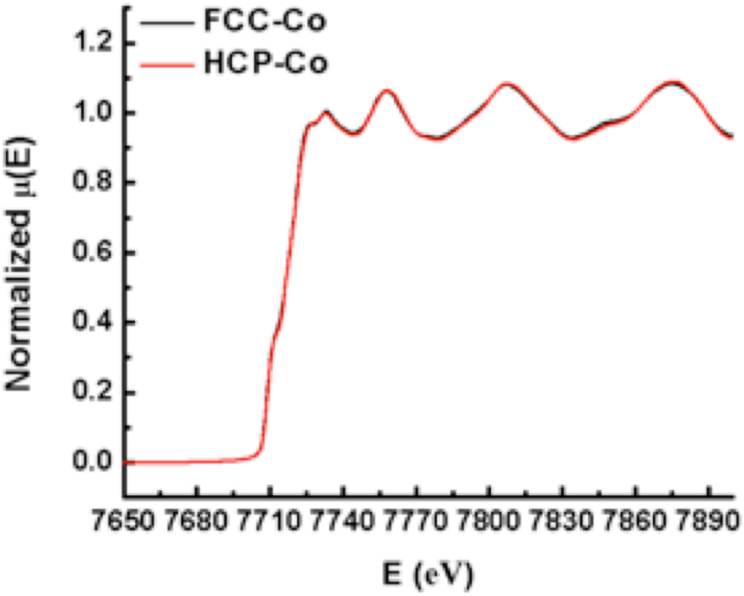

(b)

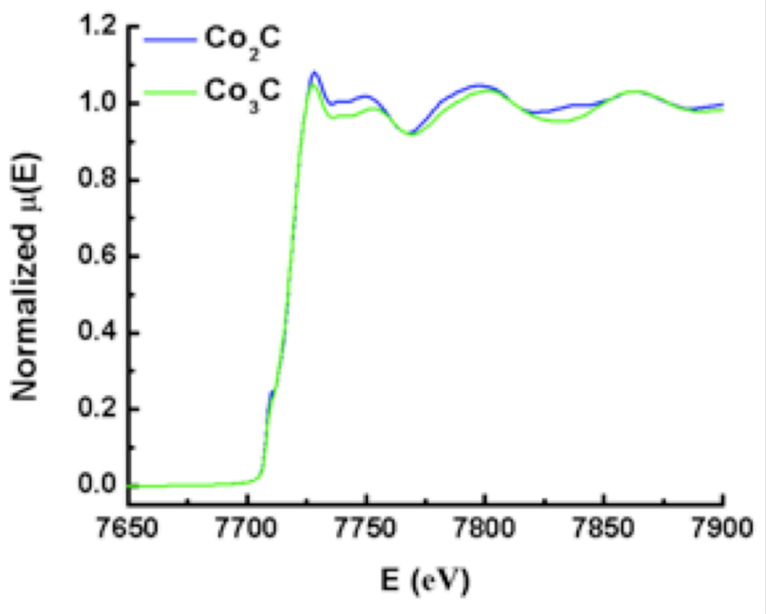

Figure 4.14 *Ex situ* Co K-edge XANES spectra for Co metal (a) and Co carbide (b) after running reactions

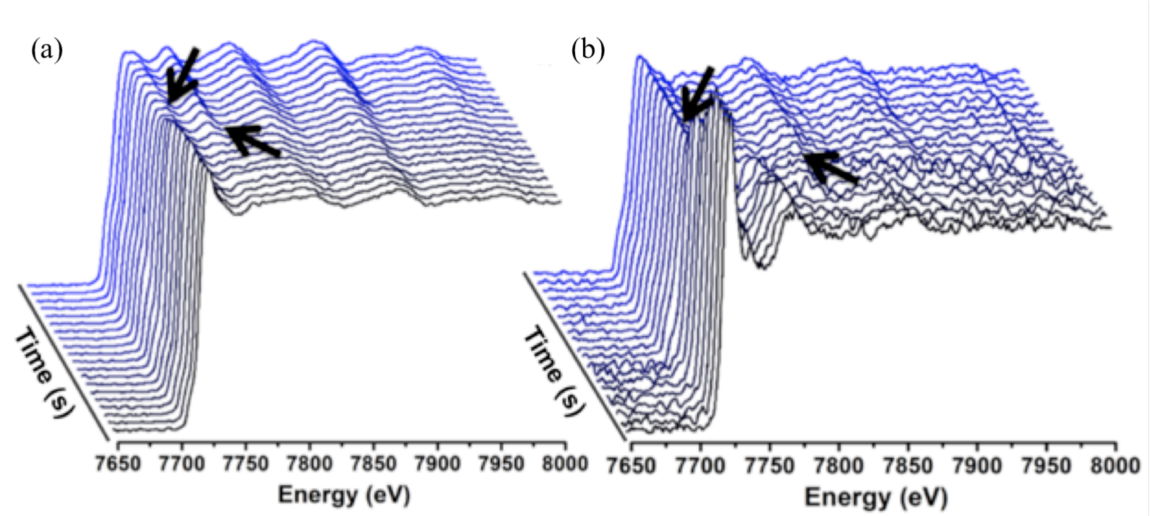

Figure 4.15 Time evolution as a function of the reduction time for Co K-edge XANES spectra for Co metal (a) and Co carbide (b)

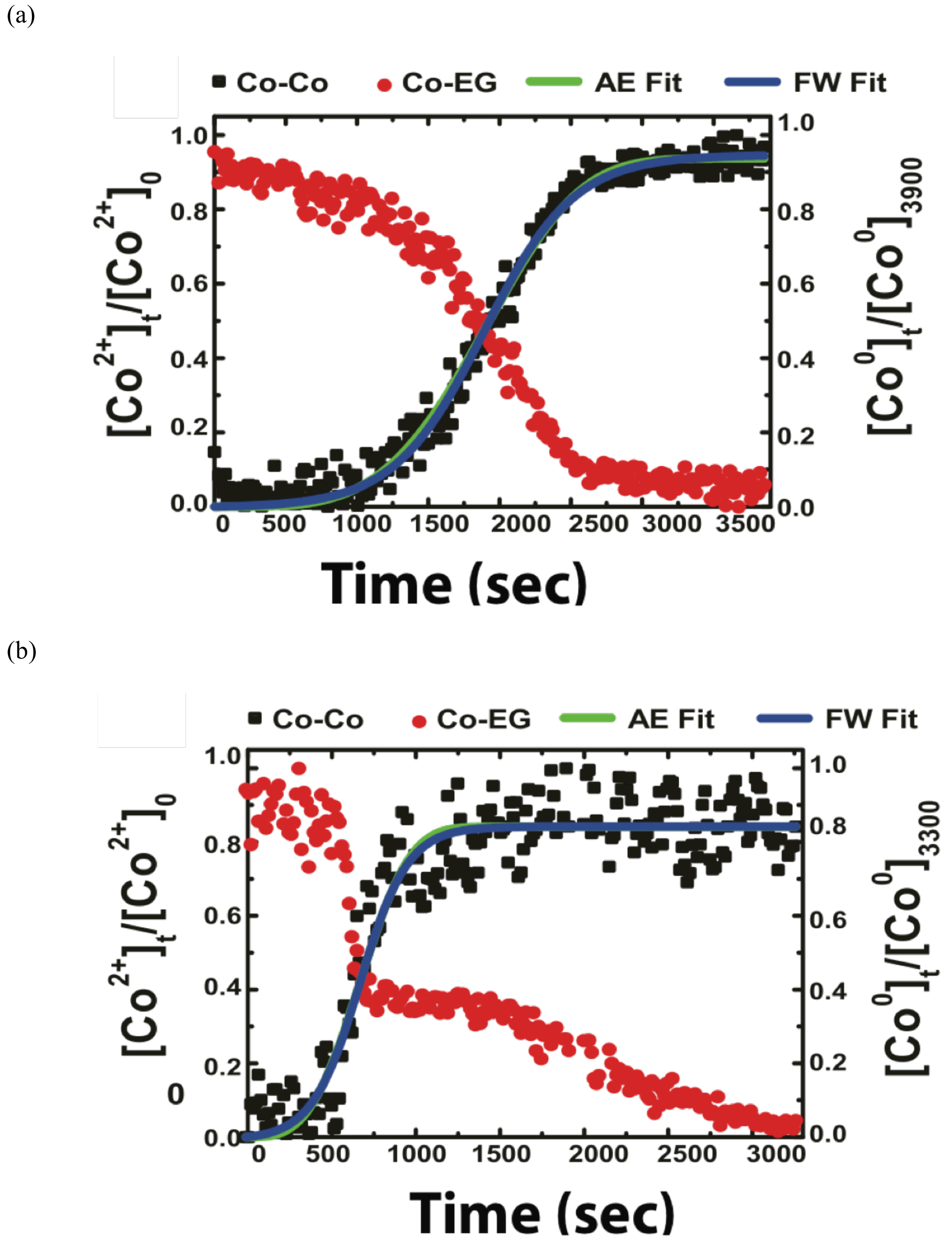

Figure 4.16 Plots of $[Co^{2+}_{precursor}]_t/[Co^{2+}_{precursor}]_0$ and (**a**) $[Co^0_{metal}]_t/[Co^0_{metal}]_{3900}$, and (**b**) $[Co^0_{carbide}]_t/[Co^0_{carbide}]_{3300}$ as a function of the reduction time on the basis of the temporal change of normalized μ. Curve fitting to the experimental data was carried out on the basis of the AE or FW model for the kinetics

Table 4.3 Fitting results based on the AE and FW equation for Co-metal and Co-carbide formation

Reaction	Sample $[Co^{2+}]/[OH^{-}]$	AE model		FW model	
		k (s^{-1})	n	$k_{1,obs}$ (s^{-1})	$k_{2,obs}$ ($s^{-1}M^{-1}$)
Cobalt Metal	0.69	6.726×10^{-4} ± 0.4369 %	4	1.205×10^{-6} ± 6.0072 %	6.242×10^{-3} ± 0.4681 %
Cobalt Carbide	0.17	1.319×10^{-3} ± 0.4549 %	3	5.872×10^{-5} ± 8.0722 %	6.990×10^{-3} ± 2.1459 %

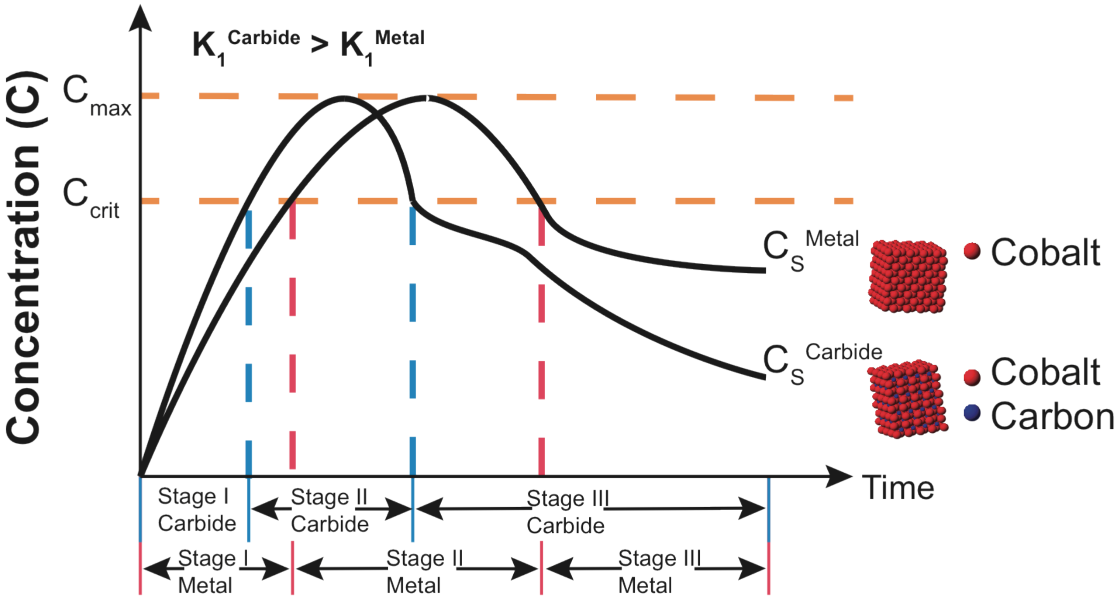

Figure 4.17 The different pathways as described in the nucleation and growth kinetic model

4.4. Conclusion

We have demonstrated the polyol synthesis of mixed phase cobalt carbide (Co_2C and Co_3C) nanoparticels having high coercivity (~2.9 kOe) and magnetic moments of more than 50 emu/g. The magnetic properties of cobalt metal and carbide exchange-coupled interaction system were explored. Furthermore, the effects of reaction parameters on magnetic properties and composition of resultants was examined. The in situ TR-XAS measurements and analysis has been clearly shown that hydroxyl ions provide nucleation sites for formation of metallic particles. By changing the $[Co^{2+}]/[OH^-]$ concentration ratio, while keeping cobalt content constant, the resultant particles exhibited different structural and magnetic properties due to their nucleation and growth rate variation. The methods applied in this study can be used to tune synthesis parameters in order to achieve strongly exchange-coupled nanoparticles in similar systems. In particular, the in situ methods, and the insights they provide on the synthesis kinetics, permit materials scientists to significantly narrow down the very large parameter space that exists in optimizing synthesis protocols for the purpose of making large batches of magnetic nanoparticels. Thus, the result reported in this study is an important step in attenuating the critical-materials aspects of rare-earth elements and satisfying the ever-increasing demand for permanent magnets for clean technology applications.

Chapter 4, in full, is a reprint of the material “In Situ Non-aqueous Nucleation and Growth of Next Generation Rare-Earth-Free Permanent Magnets” as it appears in the Physical Chemistry Chemical Physics, Hyojung Yoon, Aoran Xu, George E. Sterbinsky, Darico A. Arena, Ziying Wand, Peter W. Stephens, Ying Shirley Meng, and Kyler J. Carroll, 2015, 17, 1070. The dissertation author was the primary investigator and author of this paper. All the experiment and author of this paper. All the experiment and writing were performed by the author.

Chapter 5. Mitigating Surface Structural Instability of High Voltage Spinel Cathode Materials in Li-ion Batteries

Although high voltage spinel $LiNi_{0.5}Mn_{1.5}O_4$ is considered to be a promising high-energy and high-power density cathode material for Li-ion batteries, it exhibits poor cycle life and capacity degradation, especially at elevated temperatures. In this work new findings on structural stability affecting the electrochemical longevity of the $LiNi_{0.5}Mn_{1.5}O_4$ material are discovered using a combination of *in situ* synchrotron X-ray absorption spectroscopy and double-aberration-corrected scanning transmission electron microscopy. We elucidate cation migration and subsequent surface structural changes at the atomic level. Combining the DFT + U calculations with our experimental observations, a correlation between these structural instabilities and the capacity degradation is established. It is found that a well-maintained surface structure with low surface energy could be obtained by through a synthetic route. This study yields new insights on novel material design principles for preventing capacity degradation in transition metal oxide materials for energy storage in high voltage Li-ion batteries.

5.1. Introduction

In the past decade, $LiNi_{0.5}Mn_{1.5}O_4$ (LNMO), one of derivatives of 4 V-spinel $LiMn_2O_4$ (LMO) electrode, has gained a lot of research attention as a promising candidate for powering electric vehicles and grid energy storage that could facilitate the use of renewable energy in larger scale applications.[75-78] Cation substitution for Mn by divalent metal ions in the spinel lattice has proven to be an effective way to improve the electrochemical performance of LMO by providing the stable 3D channels of Li-ion diffusion. Although Ni-doped LNMO demonstrates a high operating voltage (~4.7 V vs. Li) and better structural stability compared to the parent material, LMO, the poor cycle and capacity fading still remain to be the major challenges in its widespread usage.[32, 79-84] To meet the recent demands, it is of critical importance to ensure that the LNMO material can be cycled at high rates and high temperature with fast Li insertion-extraction kinetics. The basis of lithium-ion battery (LiB) operation is intercalation reactions in which guest ions are inserted and extracted from interspace within a host lattice without significantly altering the structure itself. Despite the fact that there are minimal changes to the lattice during intercalation at low voltages (< 4.4 V), undesirable restructuring of the lattice is often accompanied by phase transition at high voltages. It is one of the major factors that limits the kinetics and reversible energy density of LiB. Intensive investigation has been conducted on the crystal structure of bulk LNMO by X-ray diffraction (XRD), neutron diffraction, nuclear magnetic resonance, and Raman spectroscopy.[85-86] Based on bulk structural observations during extended storage or an electrochemical cycling, several mechanisms have been proposed for the lattice restructuring: (1) lattice modifications accompanied by the Jahn-Teller distortion,[87-89] (2) cation mixing between Li and Mn, and (3) loss of crystallinity via the dissolution of Mn^{2+} ion into the electrolyte.[90-92] These structural studies provide valuable information to better understand the reaction mechanisms in the bulk. However, a detailed understanding regarding the surface structural stability of the LNMO is still lacking, which involves a local redox process initiated by oxidation of the electrolyte and catalyzed by the electrode surface.[76, 93] Under these circumstances, Mn dissolution is known to cause the most detrimental effect on structural stability.[94-97] In particular, it can lead to surface phase transformation from spinel to rock-salt structure,[87, 98-100] as well as loss of crystallinity upon cycling,[80, 101-103] which is known to limit the capacity retention. In-depth investigations are necessary to identify the evolution of the surface structure changes associated with Mn dissolution.

We utilize a variety of short- and long-range structural surface sensitive techniques to assess the importance of chemical-physical characteristics on the capacity fade of high voltage LNMO material upon cycling. Polyol process (*P-*) is chosen to synthesize LNMO materials compared to the conventional sol-gel method (*SG-*), because polyol medium itself acts not only as a solvent in the process, but also as a stabilizer, limiting particle growth and prohibiting agglomeration.[104-106] More importantly, this innovative synthesis process provides a superior reducing environment for synthesizing LNMO materials,[107] which can play a vital role in obtaining high-performance LNMO material with high energy density. Total electron yield (TEY) and fluorescence yield (FY) synchrotron X-ray absorption spectroscopy (XAS) were used to confirm the surface and bulk local structural changes. Additionally, electron energy loss spectroscopy (EELS) and high-angle annular dark-field scanning transmission electron microscopy (HAADF-STEM) quantifies surface structural changes.

5.2. Experimental

$LiNi_{0.5}Mn_{1.5}O_4$ nanoparticles with same stoichiometries were prepared *via* two different synthetic methods: (1) conventional sol-gel method[108-110] and (2) polyol process.

As for *Sol-gel methods,* the sol solution were prepared from the stoichiometric mixture of $Ni(CH_3COO)_2{\cdot}4H_2O$ (Aldrich), and $Mn(CH_3COO)_2{\cdot}4H_2O$ (Aldrich) in distilled water. The solution of $LiOH{\cdot}2H_2O$ (Aldrich) in distilled water and aqueous solution of citric acid was added dropwise to the metal precursor mixture stirring continuously. Next, the pH of the mixed solution was adjusted to 7 by adding an ammonium hydroxide solution. As-prepared sol solution was dried at 70 °C with a vigorous mechanical stirring. After gel formation, the precursor was further dried overnight under vacuum oven at 120 °C for overnight, eventually, the resulting gel precursors were decomposed at 500 °C for 12 hours in air and then calcinated at 900 °C for 14 hours in air, in sequence.

In case of *Polyol process,* $Ni(CH_3COO)_2{\cdot}4H_2O$, $Mn(CH_3COO)_2{\cdot}4H_2O$, $LiOH{\cdot}2H_2O$, and citric acid were added to 100 ml tetraethylene glycol (TTEG) in a stoichiometric molar ratio. The mixture was heated at 280 °C for 3 h in a round bottom flask connected to a refluxing condenser to ensure full activation of the polyol medium. The resulting solution was centrifuged several times with methanol and subsequently dried at 80 °C for overnight. The resulting precursors were decomposed at 500 °C for 12 hours in air and then calcined at 800 °C for 1 hour in air.

Powder x-ray diffractions (XRD) of all samples were collected by a laboratory x-ray diffractometer (XRD, Bruker D8) using a Cu K_α radiation. The data was collected by continuous scanning of a detector covering an angular range from 10.0° to 80.0° with a scan rate of $0.02°\ s^{-1}$ and wavelengths of λ= 1.54 Å. The Rietveld refinement was done by FullProf.

The amount of cation dissolution into the electrolyte was analyzed by inductive coupled plasma atomic emission spectroscopy (ICP-OES Perkin Elmer Plasma 3700). A custom-made three-electrode cell was disassembled in argon filled glovebox and the electrolyte was collected and separated from the other battery components. The ICP-OES equipped with two monochromators covering the spectral range of 167-785 nm with a grated ruling of 3600 lines/mm. The system is capable of analyzing materials in both organic and aqueous matrices with a detection limit range of less than 1 part per billion.

The particle size and morphologies were checked using field emission-scanning electron microscope (FE-SEM, Phillips, XL30) at an acceleration voltage of 15 kV after sputter-coating all the samples with iridium for 6s.

For the composite electrode fabrication, the slurry consisting of 80 wt.% active materials, 10wt. % acetylene carbon black, and 10 wt.% poly(vinylidene fluoride) (PVdF) in N-methyl pyrrolidone (NMP) was coated on a aluminum foil current collector, and then dried overnight in a vacuum oven at 80 °C, and followed by punching and pressed uniaxially. As-prepared electrodes were dried again at 80 °C for 6 hours before storing them in an argon-filled glovebox (H_2O level of <1 ppm) (MBraun, Germany) before cell assembly. For the electrochemical characterizations, lithium metal (Aldrich) was used for the negative (counter) electrode, and Celgard model C480 separator (Celgard Inc., US) was used as a separator. The electrolyte was a 1- M solution of lithium hexafluorophosphate ($LiPF_6$) in a 1:1 volume mixture of ethylene carbonate (EC) and dimethyl carbonate (DMC). The cell used for the electrochemical tests was assembled in a glove box (MBraun, Germany) filled with purified argon gas. The as-prepared cell was charged and discharged between constant potential of 3.50 V and 4.85 V (*vs*. Li/Li^+) at a rate of C/10 (the theoretical specific capacity of 146.72 mAh g^{-1} of $LiNi_{0.5}Mn_{1.5}O_4$ spinel material was assumed). An Arbin battery cycler was employed to carry out all of the galvanostatic cycling tests.

Electron microscopy was carried out using the double aberration-corrected scanning TEM (TEAM 0.5) microscope operated at an acceleration voltage 80 kV installed at the National Center for Electron Microscopy (NCEM) at Lawrence Berkeley National Laboratory (LBNL). The images were recorded on a 3 mm diameter specimen mounted to a double-tilt holder in a conventional stage that enables a tilting range of ± 20-25 ^{o} in combination with the ultrahigh-resolution pole-piece lens employed. All annular dark-fiels STEM micrographs were recorded in TEAM 0.5 with a convergence angle of 30 mrad and a probe size of ~1.5 Å after fine-tuning of the probe corrector at 80 kV. All EELS spectra shown in this work were acquired from a square area of ~0.5 × 0.5 nm with an acquisition time of 3 sec and a collection angle of 35 mrad. To minimize possible electron beam irradiation effects, EELS data were acquired from areas without pre-beam irradiation. Mn L_3 to L_2 intensity ratio analysis was done by averaging over 8 to 12 spectra using the method described by Wang et al.[111]

In situ XAS experiments were carried out at beamline X-18B at the National Synchrotron Light Source (NSLS). A Si (111) double-crystal monochromator detuned to 30 % of its original maximum intensity to eliminate the high-order harmonics. Mn K-edge (~ 6539 eV) XAS spectra were collected simultaneously in both fluorescence yield (FY) mode, utilizing a gas ionization chamber as a detector, and in total electron yield (TEY) mode under He gas flow. The cycled cathode electrodes were first washed by with DMC solvent and then mounted on the sample holder of a specially designed cell.[112]

Reference spectra of Mn foil were used to maintain energy calibration. X-ray absorption near edge structure (XANES) and extended X-ray absorption fine structure (EXAFS) data were analyzed by the ATHENA software package.[113] The extracted EXAFS signal, $\chi(k)$, was weighted by k^3 to emphasize the high-energy oscillations and then Fourier-transformed in k-ranges of 2.5 to 7 $Å^{-1}$ for Mn to obtain the magnitude plots of the EXAFS spectra in R-space (Å). For the time-resolved *in situ* analysis, a previously reported in situ XAS reactor was used (presented in Chapter 4).[106] The *in situ* study involves analyzing the X-ray absorption near edge structure (XANES) of the Mn K-edge (~ 6539 eV). We monitor the fluorescent X-ray intensity (I_f) using a Passivated Implanted Planar Silicon (PIPS) detector, where $\mu(E) = I_f/I_0$.

The DFT+U calculations we adopt here treat core electrons by projector augmented-wave method as implemented in the Vienna ab initio simulation package (VASP). The rotationally invariant approach of the on-site Hubbard U given by Liechtenstein et al. is utilized at the Mn sites. The U value, Ueff = U-J = 4.84 eV, is chosen similar to a previous study. All calculations are performed with a plane wave cutoff of 420 eV. A bulk thickness of around 15 Å and a vacuum thickness around 15-20 Å are always adopted. The surface calculations parameters are fixed to the relaxed bulk values, and only the atomic positions are allowed to relax.

5.3. Results and Discussion

5.3.1. Materials Properties and Electrochemistry of the $LiNi_{0.5}Mn_{1.5}O_4$/Li Battery System

Extraordinary capacity retention and cyclablility at an elevated temperature are achieved for *P*-LNMO as opposed to the conventional *SG*-LNMO. Figure 5.1 illustrates evaluated electrochemical Li-insertion properties of *SG*- and *P*-LNMO electrodes between 3.50 and 4.85 V vs. Li at the C/10 rate in both ambient and elevated temperature (55 °C) conditions. Typical galvanostatic charge-discharge curves of spinel phase materials were recorded. Both materials displayed a plateau at approximately 4.7 V vs. Li and delivered a discharge capacity of ~120 mAh g^{-1} after the first charge (in Figure 5.2). To assess the stability, we selected an aggressive test profile where the cells were cycled at 55 ^{o}C. As expected, both compounds experienced capacity fading during cycling, as a result of side reactions between the electrolyte and cathode active materials. It is proposed that Mn^{3+} ions at the surface undergo a disproportionation reaction, $2Mn^{3+} = Mn^{2+} + Mn^{4+}$, and the Mn^{2+} tends to dissolve into the electrolyte causing a degradation of the cell performance. At the elevated temperatures, these reactions are highly accelerated and a drastic fade in capacity profiles is noted. The cell based on SG-LNMO retained only 40 % of its initial capacity after 100 cycles, whereas P-LNMO showed excellent capacity retention of 90 % during the same cycling period. ICP-OES measurement (Figure 5.3) was followed to determine the amount of Mn dissolution into electrolyte after cycling, which has been well acknowledged as a major failure mechanism of LNMO positive electrodes.[101-102, 114] However, based on our SEM results, *SG*- and *P*-LNMO samples had similar morphologies with an average particle size of approximately 200 nm (70 – 280 nm) as shown in Figure 5.4. All of the XRD peaks in Figure 5.5 could be indexed using the space group *Fd-3m*, showing the same long-range ordered structure (Rietveld refinement results are listed in Table 5.1 and 5.2, respectively). Both LNMO spinel materials showed a cubic close packed structure where lithium is in the tetrahedral sites and nickel and manganese are disordering in the octahedral sites. From these classical bulk material characterizations, we have not noticed any significant distinction between *SG*- and *P*-LNMO; therefore, we further investigated the local atomic structures and the effect of transition metal (TM) dissolution via synchrotron XAS and aberration-corrected STEM techniques with EELS analysis.

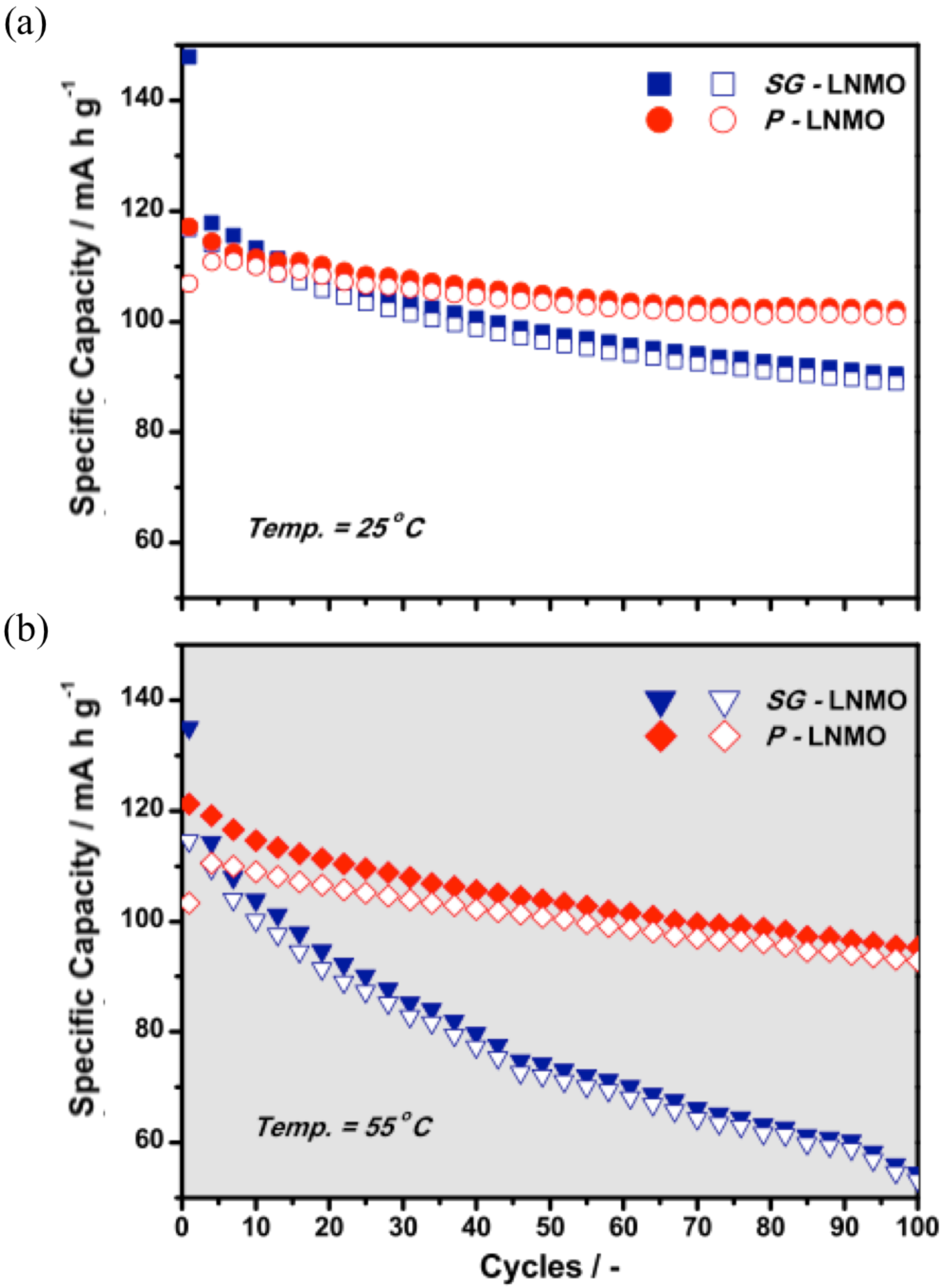

Figure 5.1 Dependence of charging and discharging capacity retention on number of cycles at 25 and 55 °C

(a)

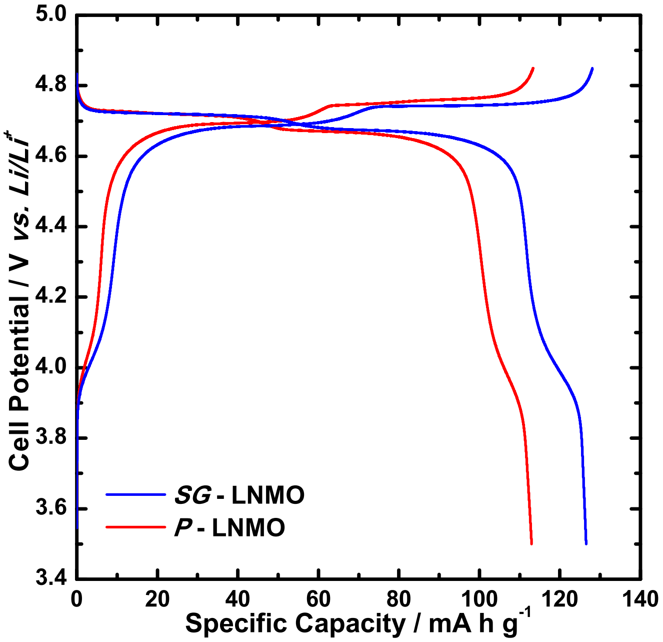

(b)

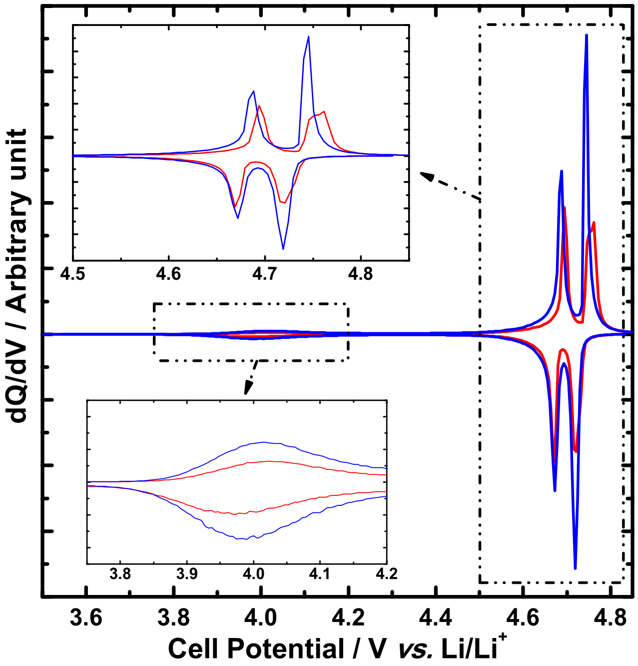

Figure 5.2 (a) Electrochemical charge and discharge voltage profiles between 3.50 and 4.85 V (vs. Li/Li$^+$) (b) Differential capacity, dQ/dV, of both sol-gel and polyol materials

(c)

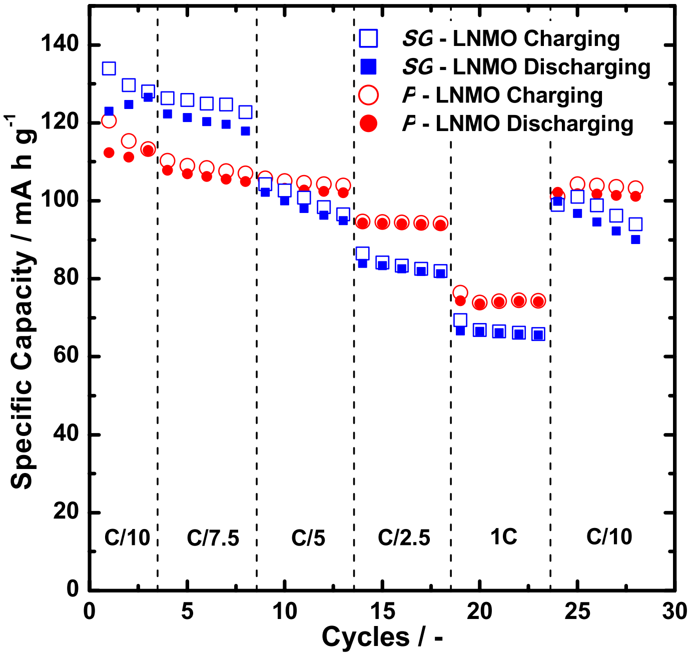

Figure 5.2 (c) Variation of capacity retention with various discharging rates obtained for $LiNi_{0.5}Mn_{1.5}O_4$ powders synthesized via sol-gel and polyol methods (continued)

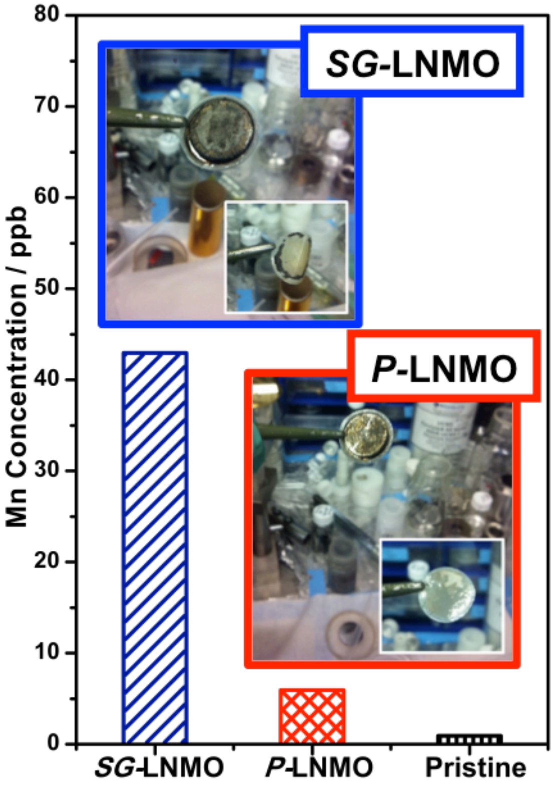

Figure 5.3 ICP-OES analysis of the Mn dissolution into the electrolyte with the cell aging

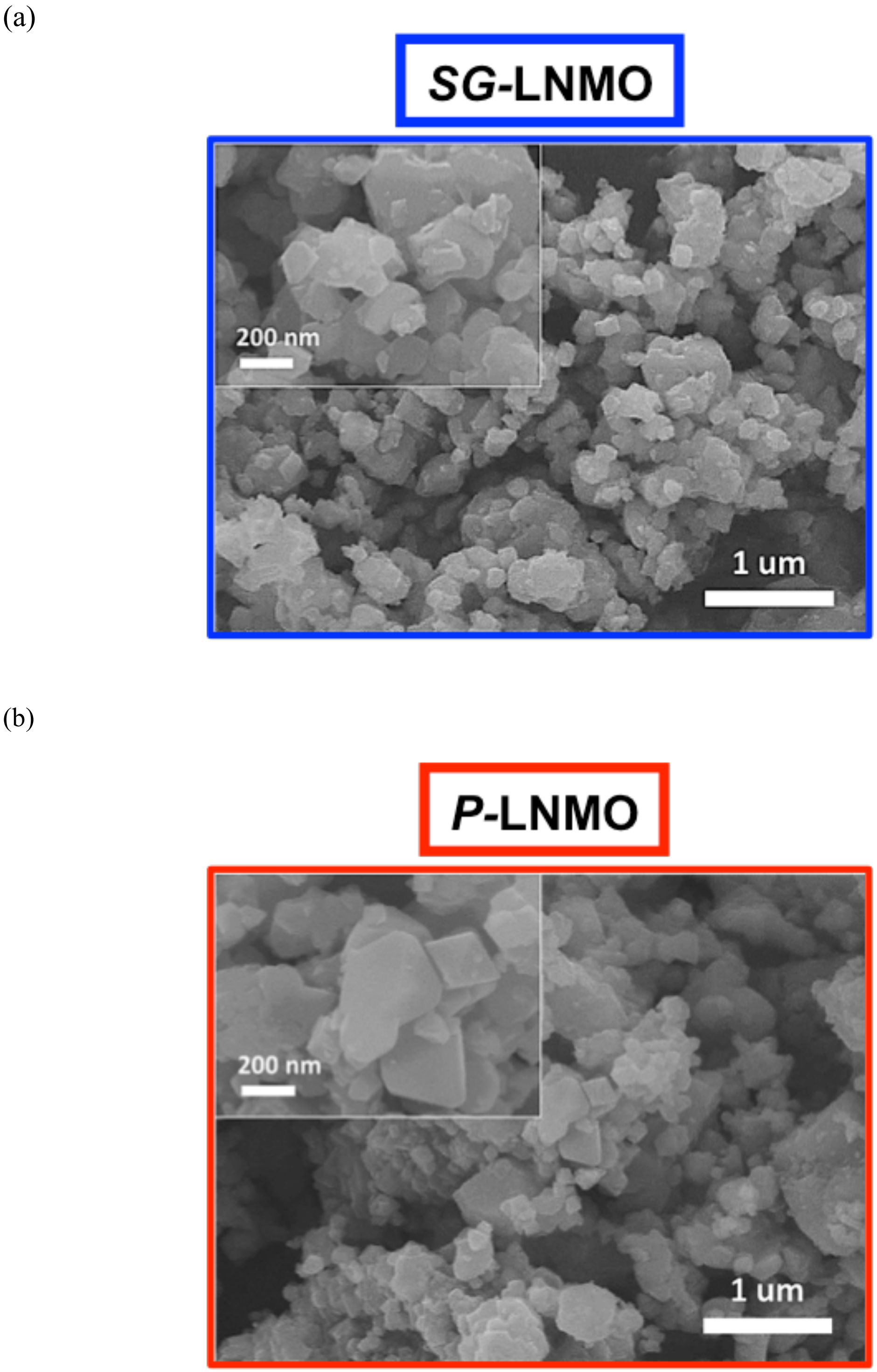

Figure 5.4 Scanning electron micrographs of $LiNi_{0.5}Mn_{1.5}O_4$ powders synthesized via a sol-gel method (a) and polyol method (b)

(a)

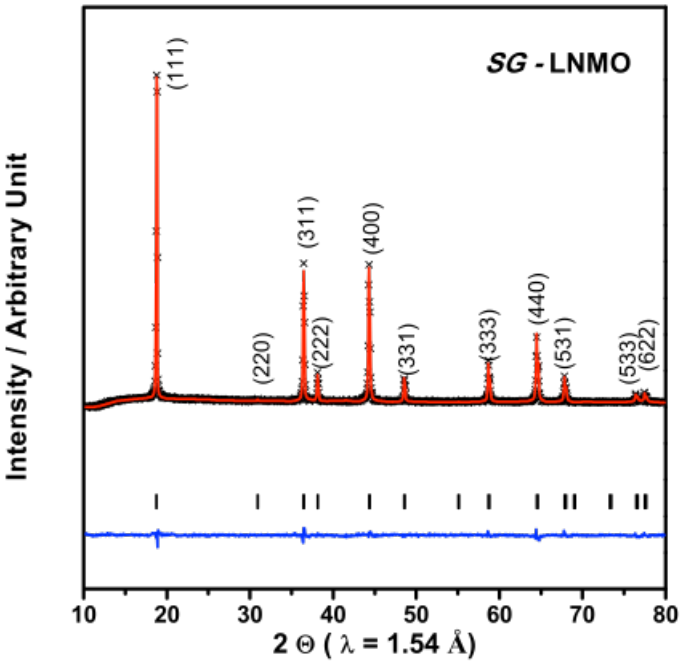

(b)

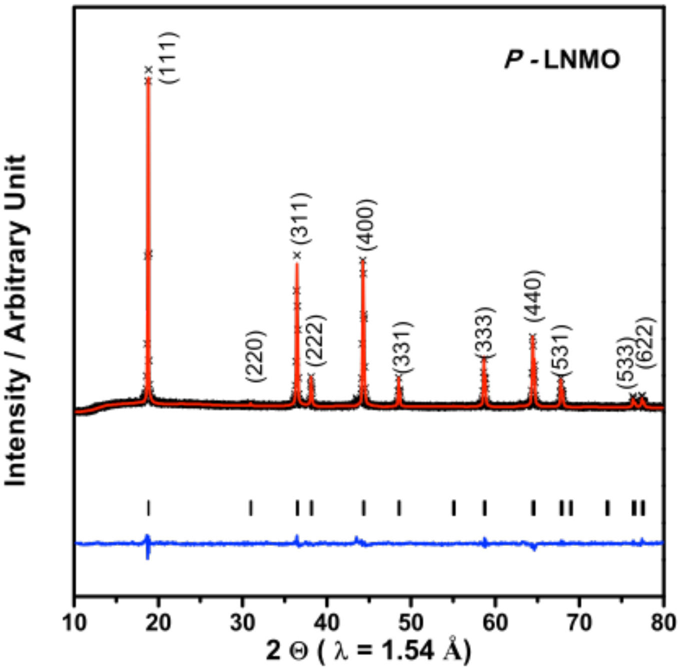

Figure 5.5 The Rietveld refinement results from X-ray diffraction patterns collected from $LiNi_{0.5}Mn_{1.5}O_4$ powders synthesized via a sol-gel method (a) and polyol method (b)

Table 5.1 Lattice parameters, atomic positions, and site occupancies results from Rietveld refinement of sol-gel powders

Z	Site	X	Y	Z	Occ.
Li	**8b**	**0.37500**	**0.37500**	**0.37500**	**0.98610**
Ni	**8b**	**0.37500**	**0.37500**	**0.37500**	**0.01390**
Li	**16c**	**0.00000**	**0.00000**	**0.00000**	**0.01390**
Ni	**16c**	**0.00000**	**0.00000**	**0.00000**	**0.48610**
Mn	**16c**	**0.00000**	**0.00000**	**0.00000**	**1.50000**
O	**32e**	**0.23987**	**0.23987**	**0.23987**	**4.00000**

a = b = c = 8.173926 Å , α = β = γ = 90 ° , F d -3 m

R_{wp}: 1.88 %, R_b: 5.784 %

Table 5.2 Lattice parameters, atomic positions, and site occupancies results from Rietveld refinement of polyol powders

Atom	**Site**	**X**	**Y**	**Z**	**Occ.**
Li	**8b**	**0.37500**	**0.37500**	**0.37500**	**0.97522**
Ni	**8b**	**0.37500**	**0.37500**	**0.37500**	**0.02478**
Li	**16c**	**0.00000**	**0.00000**	**0.00000**	**0.02478**
Ni	**16c**	**0.00000**	**0.00000**	**0.00000**	**0.47522**
Mn	**16c**	**0.00000**	**0.00000**	**0.00000**	**1.50000**
O	**32e**	**0.23904**	**0.23904**	**0.23904**	**4.00000**

a = b = c = 8.165595 Å , α = β = γ = 90 ° , F d -3 m

R_{wp}: 2.95 %, R_b: 5.467 %

5.3.2. Local Atomic-level Crystal Structure of LNMO Before and After Cycling

Aberration-corrected STEM is used to investigate the local atomic-level crystal structures. Multiple regions were selected for this study to check the consistency of the results. Representative HAADF-STEM images of the pristine and cycled *SG*- and *P*-LNMO (at the discharge state after 20 cycles between 3 and 4.85 V vs. Li) which were taken along the [110] crystallographic direction are shown in Figure 5.6. In this direction, the position of TM heavy atomic columns can be clearly identified as a diamond configuration. Although Li would be invisible to HAADF-STEM, measurable intensities on these columns imply the presence of anti-site TM defects. A well-defined spinel structure in the bulk of both pristine materials extends on the surface as presented in Figure 5.6(a) and (b). However, the HAADF images of the cycled *SG*-LNMO (Figure 5.6(c)) show contrasting changes on the surface of atomic columns corresponding to the surface structural changes. Local atomic-level defect structures are observed only in the surface regions (~2 nm) of *SG*-LNMO compared to the bulk structures. On the contrary, both the bulk and surface structures of *P*-LNMO after cycling (Figure 5.6(d)) still maintained the pristine spinel structure. Close examination of the cycled *SG*-LNMO surface regions (Figure 5.6(c)) at higher magnification indicate the presence of bright contrast in the tetrahedral Li sites and empty octahedral sites in the center of the diamond configuration. This contrast cannot appear because of the light elements such as Li or O due to their low atomic number Z which corresponds to the presence of the TM ion. Based on our HAADF images, the TM ions migrated into two different Li atomic sites of *SG*-LNMO, which resulted in local atomic structural changes. Tetragonal distorted spinel (Mn_3O_4) and rocksalt-like (MnO) structures can be formed when TM ions migrated into the tetrahedral and octahedral Li sites respectively. Especially, the Mn_3O_4 structure contains 1/3 soluble Mn^{2+} ions in the tetrahedral site, attributed to the Mn ion dissolution. Once the Mn_3O_4 is formed during cycling, the tetrahedral Mn^{2+} ions can dissolve into the electrolyte. This is in contrast to the cycled *P*-LNMO, which surprisingly maintained its original spinel structure. This is in agreement with excellent cycling performance of *P*-LNMO sample observed from our electrochemical (Figure 5.1(a)) and ICP-OES results, which is attributed to the stability of the surface structure of *P*-LNMO.

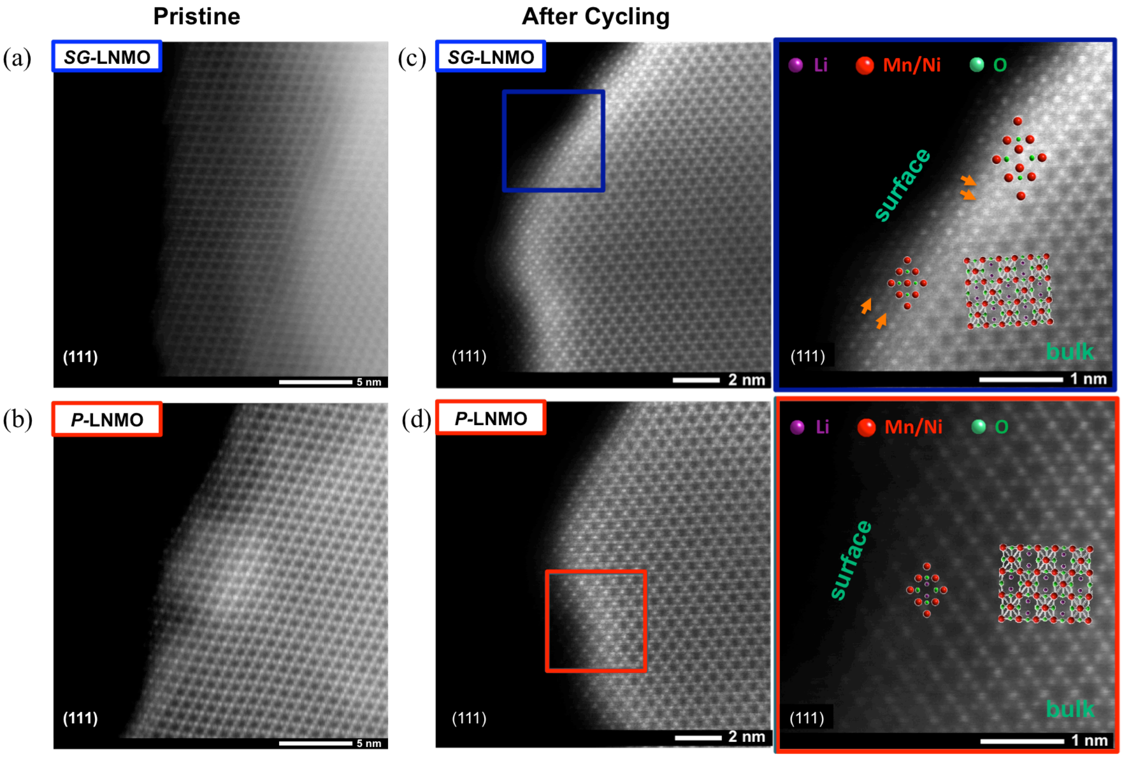

Figure 5.6 High resolution STEM images of the bulk and surface of pristine *SG*- (a) and *P*-$LiNi_{0.5}Mn_{1.5}O_4$ (b). 20th cycled *SG*- (c) and *P*-$LiNi_{0.5}Mn_{1.5}O_4$ (d) at high magnification taken along the [110] zone axis. The schematic crystal structures represent the Li ions (purple), transition metal ions (red) and oxygens (green)

5.3.3. Local Electronic Structure of the LNMO Before and After Cycling

In situ extended X-ray absorption fine structure (EXAFS) spectra for both charged/discharged *SG*- and *P*-LNMO were analyzed to provide in-depth insights into bonding variations of Mn during electrochemical cycling. EXAFS was performed in TEY and FY modes to obtain detailed analysis of local surface and bulk bonding variations, respectively. The absorption was measured using emitted electrons in TEY mode. TEY measurements can only probe the surface of a material (~3 nm) due to the shorter mean free path of electrons.[115-116] The Fourier-transformed (FT) Mn K-edge EXAFS spectra from both TEY and FY modes are shown in Figure 5.7. EXAFS spectra were k^3-weighted in k-space, but not phase-corrected FT, causing shorter bond lengths in the plots than for the actual ones. The FT magnitudes of pristine *SG*- and *P*-LNMO are also plotted in the bottom panels for references. The first peak is assigned to the single scattering path from Mn to the closest oxygen atoms (i.e., the Mn-O bond). The second and third peaks are assigned to Mn to the nearest TM atoms (Ni and Mn) occupying the octahedral sites and the second nearest TM occupying the tetrahedral sites (TM_{tet}). For the Mn K-edge results shown in FY mode, there were negligible alterations in both the Mn-O and Mn-TM bond length from the pristine to the 20th cycled state, indicating that Mn in the bulk of the material in *SG*- and *P*-LNMO materials is stable and maintains its original site, which is consistent with the HAADF images. However, the shift of the Mn-TM bond length and the emergence of the Mn-TM_{tet} can be observed during cycling in TEY mode, only for the cycled *SG*-LNMO. This further confirms the TM migration occurred during the cycling with the irreversible surface phase transition possibly to Mn_3O_4 and rocksalt-like structures, which caused shortening the bond length in the EXAFS spectra.

EELS spectra were acquired to further elucidate the bulk and surface structural changes by correlating the morphology with chemistry of the *SG*- and *P*-LNMO electrodes. Figure 5.8 compares the O K-edge and Mn $L_{3,\ 2}$-edge EELS spectra from surface and bulk of each pristine and cycled *SG*- and *P*-LNMO samples. The O K-edge fine structure of the cycled *SG*-LNMO sample from surface is different from the bulk. The O-K pre-peak almost disappeared on the surface of cycled *SG*-LNMO samples. This O pre-peak can be ascribed to the transition of 1 s core state to the unoccupied O-2p states hybridized with TM-*3d* states.[117-118] The decreased intensity of this peak, at energy loss of ~532 eV, on the cycled surface of *SG*-LNMO likely indicates the variation of unoccupied states of TM-*3d* and bonding lengths of TM-TM. These electronic structure changes correlate well with the atomic structure differences revealed by XAS result in TEY mode and the HAADF images of *SG*-LNMO. In addition, the L_3/L_2 intensity ratios of various manganese oxide standard samples have been measured as the reference for determining the valence state of the experimental samples (Figure 5.9). In *3d* TMs with d occupancies lower than $3d^5$, The L_3/L_2 intensity ratio is generally in a positive relationship with the d occupancy; i.e., inversely related to the oxidation state.[111-112, 119-120] Surprisingly, we observed an increased L_3/L_2 ratio for Mn after a few cycles, indicating the Mn oxidation state reduced. Furthermore, Mn reduction primarily occurred on the surface, which is associated with the pre-peak O K-edge loss of the *SG*-LNMO surface. It is notable that the electrochemically induced oxidation state gradients in Mn and the structural transition mainly occurred only at the surface a few atomic layers of *SG*-LNMO.

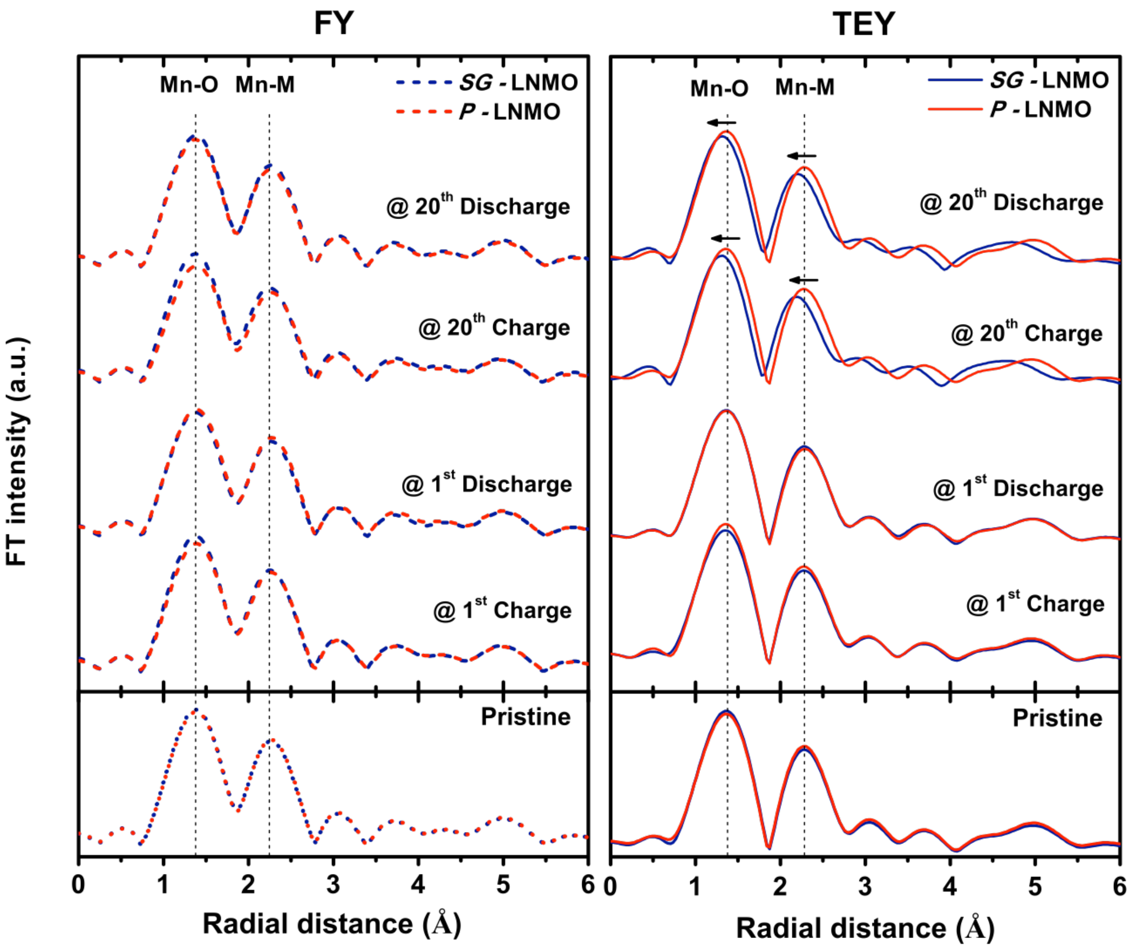

Figure 5.7 Fourier-transformed magnitude of Mn K-edge EXAFS spectra for fully charged and discharged at the first cycle and after 20 cycles with the pristine $LiNi_{0.5}Mn_{1.5}O_4$ spinel (bottom). Fluorescence yield (FY) and total electron yield (TEY) modes

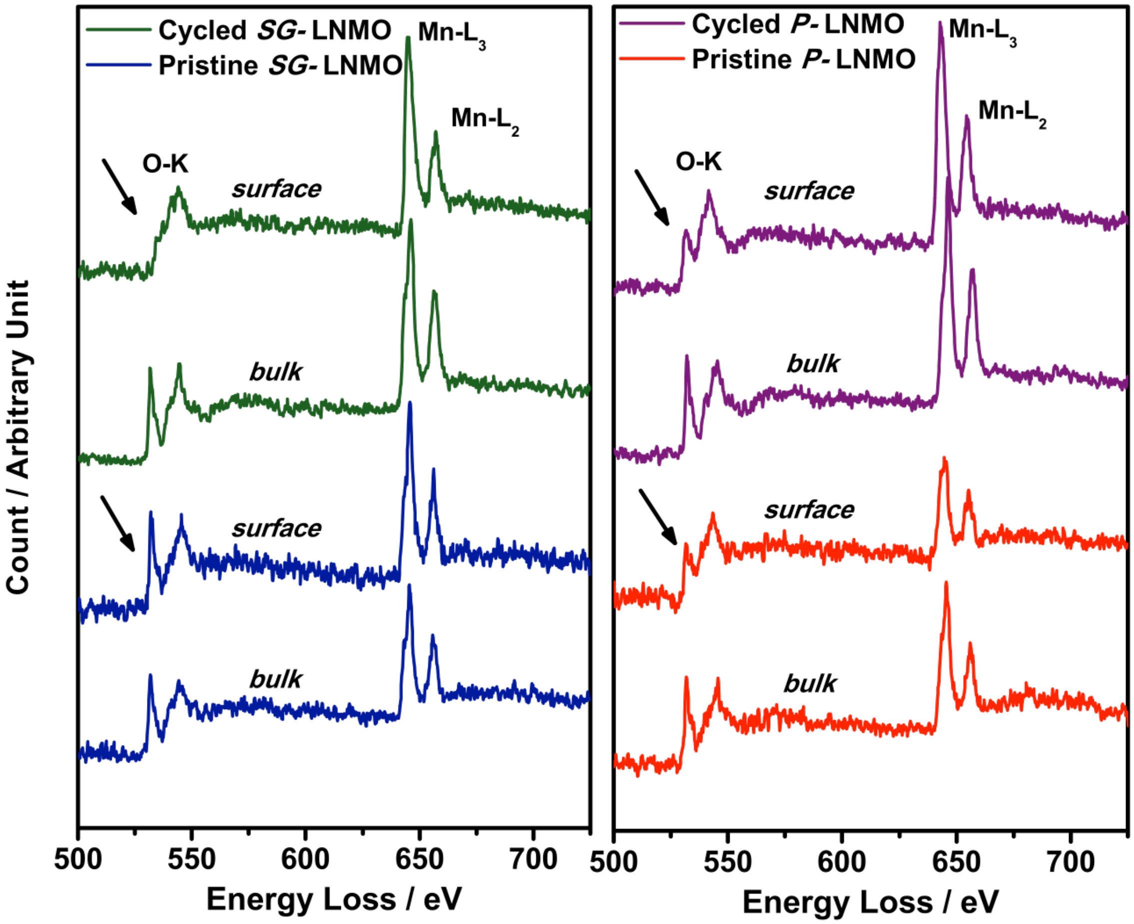

Figure 5.8 Representative EELS spectra of the O K-edge and Mn L-edge from the surface and bulk of $LiNi_{0.5}Mn_{1.5}O_4$ powders synthesized via sol-gel and polyol methods

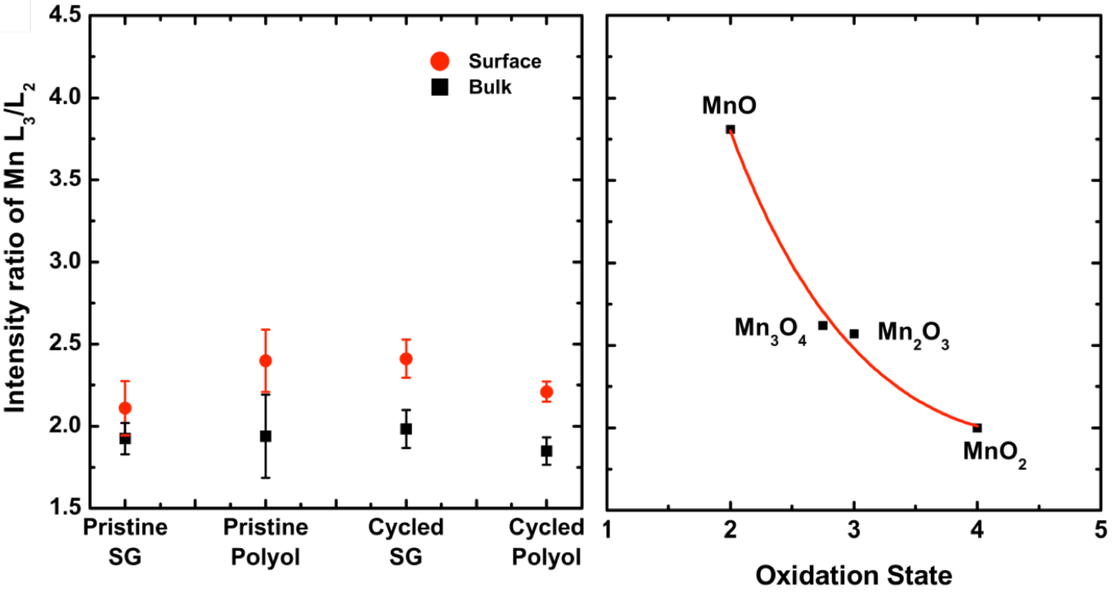

Figure 5.9 Plots of the intensity ratios of Mn L_3/L_2 calculated from the spectra

5.3.4. Origin of Different Surface Stability of the LNMO via Sol-gel and Polyol Methods

To understand how the Mn local environmental will affect the surface stability and electronic structure, we obtained electron density of states (DOS). Figure 5.10 displays the GGA+*U* calculated Mn *3d* DOS for *SG*- and *P*-LNMO. The advantage of the DFT calculations is that we can directly analyze the changes in geometric and electronic structure. Our time-resolved XAS measurements, as shown in Figure 5.11, demonstrate that an alkoxyacetate anion remains on the outer shell of the Mn cation only during the polyol process. Also, the STEM images confirm both *SG*- and *P*-LNMP is dominated by (111) surface of spinel. To further investigate the effect of existing organic molecular layer, calculations are done on bare (*SG*-LNMO) and alkoxyacetate adsorbed (*P*-LNMO) (111) surface as shown in Figure 5.12 imaginary model set up. In the projected DOS for the bare (111) *SG*-LNMO spinel surface (Figure 5.11(a)), the spin-up states in *3d* orbitals are fully occupied indicating Mn is in the divalent state as shown in the inset. It is well known for the Mn^{2+} ions dissolve into the electrolyte solution and deposit metal Mn on the surface of the negative electrode. In Figure 5.11(b), after applying alkoxyacetate adsorption onto the (111) surface, i. e. *P*-LNMO, the surface Mn is no longer divalent. The e_g orbitals are unoccupied and t_{2g} are half occupied which is consistent with the electron configuration of Mn^{4+}. Compared to the bare surface of *SG*-LNMO, the surface alkoxyacetate functional group can draw more electrons from the surface Mn ions, which results in the increased stability of higher Mn oxidation states on the surface of *P*-LMNO.

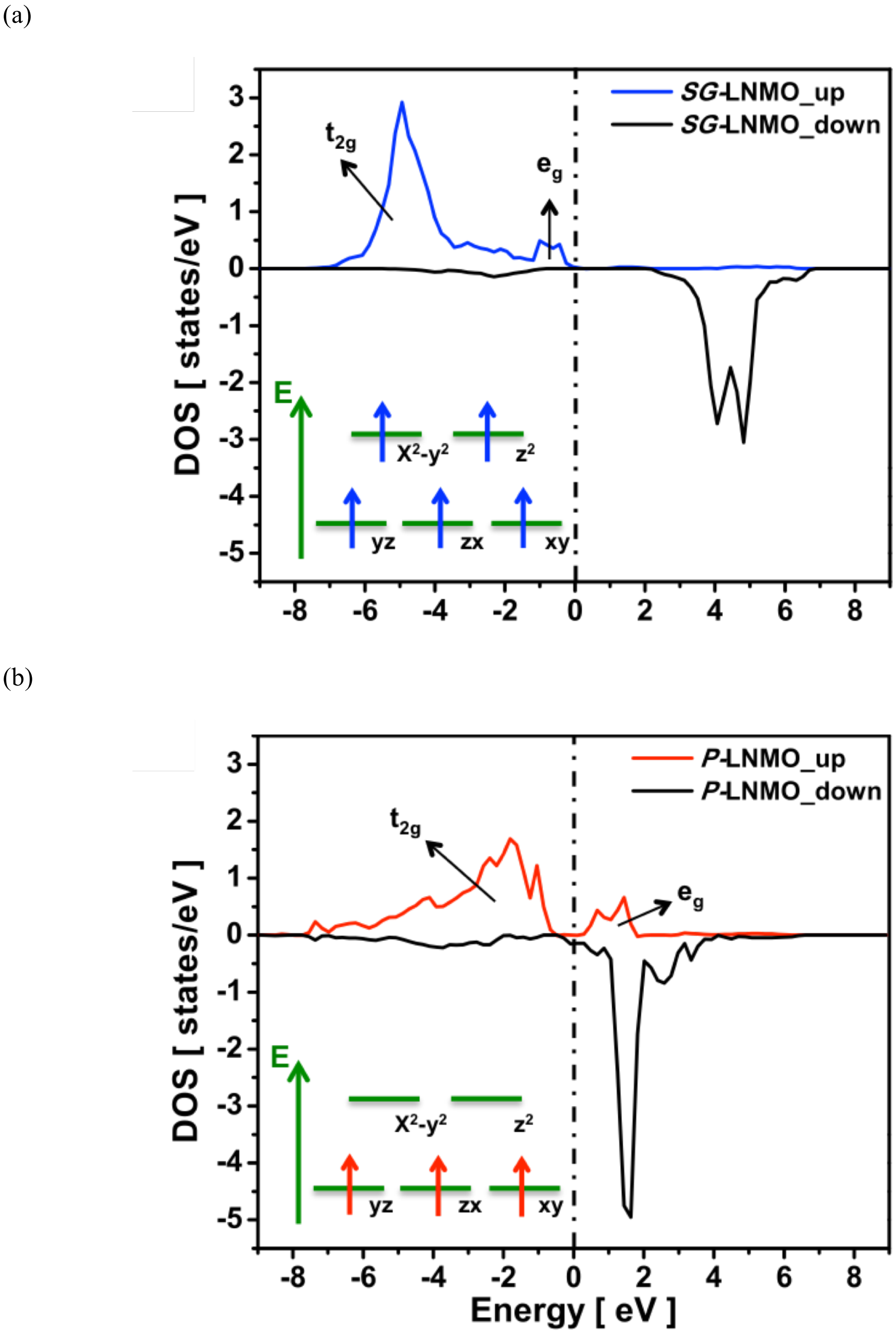

Figure 5.10 Density of state of surface Mn on bare (a) and acetate adsorbed (111) surface (b)

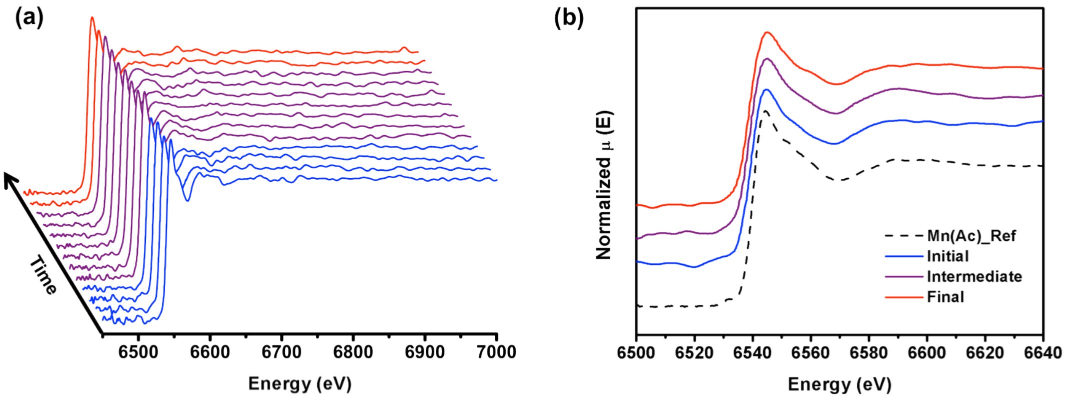

Figure 5.11 (a) Time evolution as a function of the reaction time for Mn K-edge XANES spectra during polyol process. (b) Selective XANES spectra of initial, intermediate and final stage including Mn(CH_3COO)$_2$ dissolved in TTEG

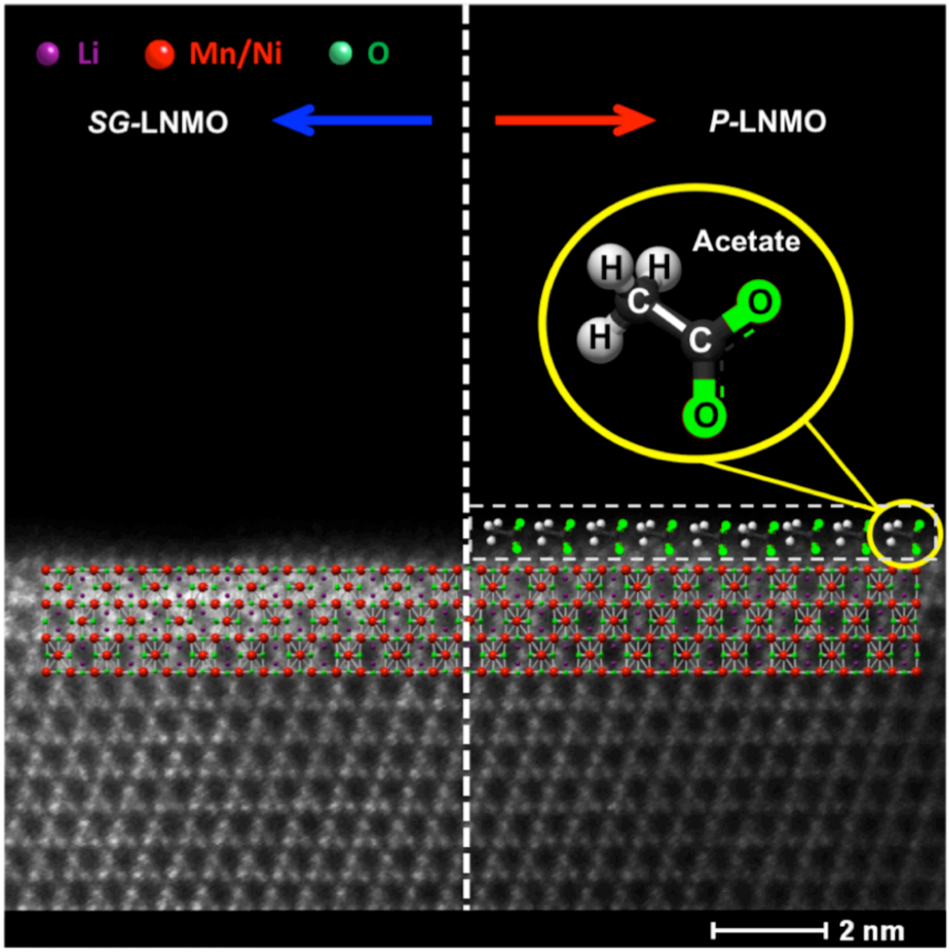

Figure 5.12 The imaginary model setup of the (111) surface: bare and with acetate adsorption

5.4. Conclusion

In conclusion, cation migration in LNMO spinel materials, which attribute to the instability of the surface structure and derivative phase transformation, has been revealed through a combination of *in situ* synchrotron XAS and C_s-corrected STEM with EELS analysis. TM ions were visualized directly as a diamond configuration along the [110] zone axis. Tetragonal distorted Mn_3O_4 spinel and rocksalt-like MnO phases were detected only at the surface regions of the cycled *SG*-LNMO particles, while *P*-LNMO maintained its original well-defined spinel structure. The *P*-LNMO materials show excellent cycling not only at ambient temperature, but also elevated temperature (~55 °C) conditions. According to first principles calculations, a stable surface of *P*-LNMO is established through an acetate-absorbed surface during the polyol synthesis even without any additional post processes, such as doping, coating or annealing. The structural changes between bulk and surface regions of the high-voltage cathode material undoubtedly influence the charge/discharge behavior and capacity fade in LiB. We anticipate that this novel synthetic approach should lead to the design and development of a wide range of other stable and safe, high-voltage intercalation compounds.

Chapter 5, in full, is currently under review for publication of the material "Mitigating Surface Structural Instability of High Voltage Spinel Cathode Materials in Li-ion Batteries" Hyojung Yoon, Hyun-Man Cho, Danna Qian, Mahsa Sina, Jim Ciston, Chengyu Song, and Ying Shirley Meng. The dissertation author was the primary investigator and author of this paper. All the experiment and writing were conducted by the author except computational calculations.

Chapter 6. Probing Defects and Electrochemical Properties in Polyol Synthesized High Voltage $LiCoPO_4$ Olivine Materials

In this chapter, $LiCoPO_4$ nanocrystals were synthesized via a polyol process and tested as cathode materials for 5 V lithium-ion batteries. X-ray diffraction patterns confirmed its orthorhombic phase in the *Pnma* space group without unwanted impurity phases. In this work, the role of defects in the crystal structure and perpetual decomposition of electrolytes were discussed to get more insight in capacity fading issues during cycling. Also, the antisite Co_{Li} defects along [010] crystallographic directions were investigated using annular dark scanning transmission electron microscopy (STEM). X-ray photoelectron spectroscopy (XPS) allowed us to determine the evolution of electrode/electrolyte interfaces upon cycling.

6.1. Introduction

There has been a constant drive to improve the specific energy and energy density of the lithium-ion batteries (LiBs) for large-scale energy storage system and future applications. It can be achieved by either choosing a cathode material that operates at a higher potential or has a higher specific capacity.[121] Among polyanion-type materials, $LiCoPO_4$ is a promising candidate because of its high redox potential (4.8V *vs.* Li^+/Li) and high specific capacity of 167 mAh/g,[122-123] resulting in an impressive specific energy of ~802 Wh/kg.[124-125] Though $LiCoPO_4$ has been extensively studied in recent years, the intrinsic low electronic conductivity and pronounced capacity fading upon cycling have not been completely understood yet to practical usage for the LiBs.[126-129]

The defects in crystals are an important factor governing the intrinsic properties of the material, such as mechanical strength, electronic conductivity, and mass diffusion rates.[130-131] Honma group have reported the intrinsic antisite point defects in $LiCoPO_4$ olivine material for the first time.[131] Their direct observation of the atom-by-atom structure confirmed cobalt (Co) atoms partly occupied the lithium (Li) sites, which hinders the diffusion of Li-ions[132-133] and the relocation of transition metal (TM) ion to the Li sites (TM_{Li}) inevitably influences the mass and the charge transport behavior of the olivine materials.[134-135] The concentration of defects in a crystal is determined by thermodynamics, materials synthesized via non-equilibrium routes generally contain higher concentrations of defects.[136-138] Therefore, careful choices of synthesis conditions or post-treatment methods are needed to control the level of defects and to tune the properties of materials. A polyol process, in which metal salts are reduced by a polyalcohol, is chosen since the method can provide a superior reducing environment[139] to producing well-defined $LiCoPO_4$ nanoparticles.[140-141] The $LiCoPO_4$ cathode materials also require an electrolyte with high oxidation stability to deliver its full capacity owing to the tendency of the electrolyte to continuously decompose in conventional organic electrolyte.[123, 142-143] Since the cyclic performance and rate capacity critically depend on the structural and phase transitions taking place during the charge-discharge cycle,[144-145] it is clear that fundamental knowledge of the underlying defects and instability of the $LiCoPO_4$ materials in $LiPF_6$-containing electrolyte solutions is needed.[146]

Herein, we report the electrochemical performance of $LiCoPO_4$ prepared by polyol synthetic routes and suggest the possible mechanisms of capacity fading through direct observation of crystal structures, especially structural defects at atomic-scale resolution. The atomic resolution high-angle annular dark field scanning transmission electron microscopy (HAADF-STEM) was used to confirm Co_{Li} antisite defects combining with powder X-ray diffraction (P-XRD) measurement upon electrochemical cycling. The local environment and oxidation states of decomposed species at the electrode/electrolyte interface were also investigated using X-ray photoelectron spectroscopy (XPS). Our results provide the better understanding of the capacity fading mechanism of the $LiCoPO_4$ cathode materials.

6.2. Experimental

$LiCoPO_4$ nanoparticles were synthesized by polyol process. Lithium dihydrogen phosphate (LiH_2PO_4) and $Co(CH_3COO)_2 \cdot 4H_2O$ were added to 100 ml tetraethylene glycol (TTEG) in a stoichiometric molar ratio (1:1). The mixture was heated at 280 °C for 3 hours in a round bottom flask connected to a refluxing condenser to ensure full activation of the polyol medium. The resulting solution was filtered and washed several times with ethanol and subsequently dried at 80 °C for overnight. The resulting precursors were decomposed at 450 °C for 12 hours. The pre-calcinated powders were prepared as a pellet for high temperature sintering. These samples were then calcinated at 800 °C for 12 hours in air. Samples were cooled in the furnace back to room temperature.

For the composite electrode fabrication, the slurry consisting active material $LiCoPO_4$ with 10 wt% acetylene carbon black and 10 wt% poly(vinylidene fluoride) (PVdF) in *N*-methyl pyrrolidone (NMP) were pasted on the aluminum foil current collector using a doctor blade and dried overnight in a vacuum oven at 80 °C overnight. The electrode discs were punched and pressed in a uniaxial way. For the electrochemical characterizations, lithium metal (Aldrich) was used for the negative (counter) electrode, and Celgard model C480 separator (Celgard Inc., US) was used as separator. The electrolyte was a 1 M solution of lithium hexafluorophosphate ($LiPF_6$) in a 1:1 volume mixture of ethylene carbonate (EC) and dimethyl carbonate (DMC). The cell used for the electrochemical tests was assembled in a glove box (MBraun, Germany) filled with purified argon gas (H_2O concentration < 1 ppm). The as-prepared cell was charged and discharged between constant potential of 2.80 and 4.95 V (*vs*. Li/Li^+) at a rate of C/10 (the theoretical specific capacity of 167 mAh/g of $LiCoPO_4$ spinel material was assumed). An Arbin battery cycler was employed to carry out all of the galvanostatic cycling tests.

Scanning electron microscope (SEM) (Phillips, XL30) and field emission transmission electron microscope (FE-TEM, JEM-2100F HR, JEOL) were employed in order to examine particle morphology and size distribution. The elemental distribution was determined using energy dispersive X-ray spectroscopy (EDS) equipped in the FE-TEM. Crystallinity of the samples was examined by X-ray diffraction (XRD) (Bruker D8) with Cu Kα radiation. XRD data was gathered in the range of $2\theta = 10 – 80°$, at a scan rate of 0.02 °/s. The refinement of the XRD data was carried out using the Rietveld method in the FullProf software package suite. Atomic resolution high-angle annular dark-field scanning transmission electron microscopy (HAADF-STEM) images were obtained using the double aberration-corrected scanning TEM (TEAM0.5) microscope operated at an acceleration voltage 80 kV installed at the National Center for Electron Microscopy (NCEM) at Lawrence Berkeley National Laboratory (LBNL). The images were recorded on a 3 mm diameter specimen mounted to a double-tilt holder in a conventional stage that enables a tilting range of ± 20-25° in combination with the ultrahigh-resolution pole-piece lens employed. X-ray photoelectron spectrometer (XPS, K-Alpha, Thermo Fisher Scientific, USA) analysis was performed with a monochromatic Al K_α X-ray source ($h\nu$ = 1486.6 eV) operating at pressure lower than 10^{-10} Torr. For high-resolution spectra, constant analyzer energy (CAE, pass energy: 50.0 eV) mode was applied, leading to a resolution of 0.1 eV. The acquired spectra were calibrated by with the binding energy of the hydrocarbon C1s (C–H) at 284.6 eV. The data were analyzed using the software CasaXPS and all peaks were fit using a Shirley-type background.

6.3. Results and discussion

6.3.1. Material Characterization of Polyol-synthesized $LiCoPO_4$ Nanoparticles

Representative morphology of the $LiCoPO_4$ powders synthesized via polyol process is shown in Figure 6.1. The primary particles are homogeneously dispersed and no secondary particles are observed through the SEM image. The average particle size is determined to be ~250 nm. TEM micrograph in Figure 6.1(b) reveals a closer aspect on one single nanoparticle. To confirm the presence of cobalt (Co), phosphorus (P), and oxygen (O) elements, EDS line scan were performed over the cross-section of the particle, with the corresponding TEM image. The blue, red and green spectra represent the counts of Co, P and O signals along the yellow scan line, respectively. The EDS spectra results clearly show the presence of Co, P and O elements in the nanoparticle. The uniformity of the elemental distribution was further verified by taking EDS maps on one single nanoparticle (Figure 6.1(c)). The signals from Co, P and O elements were detected uniformly across the whole nanoparticle, validating our synthesis method and indicating that all elements were well distributed.

To confirm the structural properties, the XRD pattern of the polyol-synthesized $LiCoPO_4$ nanoparticles was collected as shown in Figure 6.2. All diffraction peaks could be indexed as the orthorhombic space group *P n m a* using Rietveld refinement with unit cell parameters of a = 10.1951, b = 5.9201, and c = 4.6973 Å. The P atoms occupy tetrahedral sites, while the Li (4a) and Co (4c) atoms occupy octahedral sites in agreement with reported olivine structure.[147-148] It may be described as chains (along the *c* direction) of edge-sharing cobalt centered octahedral connected to one another by phosphate tetrahedral. These $(CoPO_4)^-$ are connected to one another by octahedrally coordinated lithium atoms along the *b* axis.[136, 149] Table 6.1 gives other fractional atomic coordinates properties obtained from the Rietveld analysis of the structures. It is evident from the XRD result that a pure phase of $LiCoPO_4$ nanoparticles has been successfully prepared *via* polyol process.

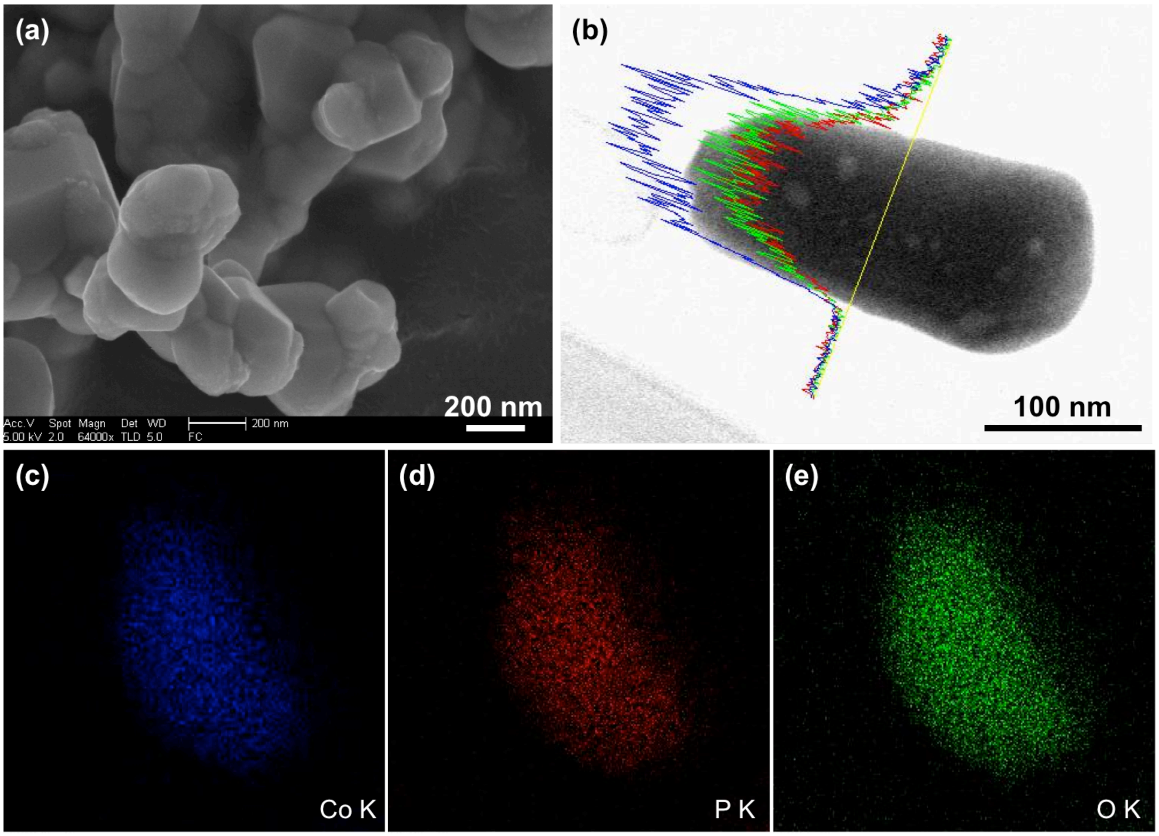

Figure 6.1 (a) SEM image of $LiCoPO_4$ powders synthesized via a polyol process. (b) TEM image of an individual nanoparticle. The blue, red and green lines represent counts of cobalt, phosphorus and oxygen signals along the yellow line. Element mapping of cobalt (c), phosphorus (d) and oxygen (e)

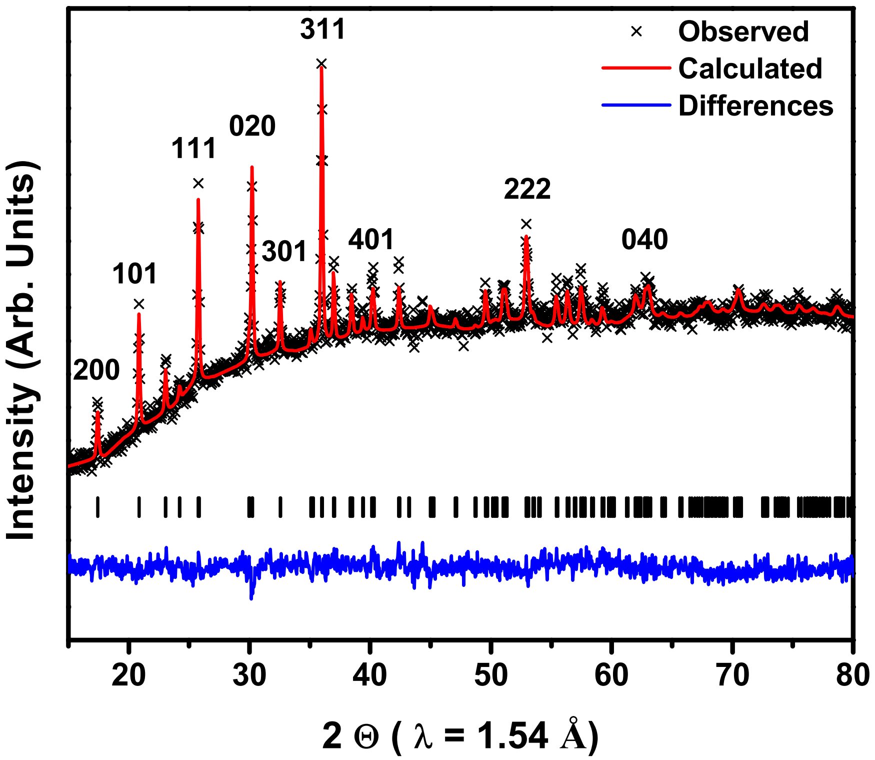

Figure 6.2 The Rietveld refinement results from powder X-ray diffraction patterns collected from the polyol-synthesized $LiCoPO_4$ powders. The black crosses represent the observed pattern, the red line corresponds to the calculated diffraction pattern and the blue is the difference pattern

Table 6.1 Lattice parameters, atomic positions and site occupancies result from Rietveld refinement of the polyol-synthesized $LiCoPO_4$ powders

Atom	**Site**	**X**	**Y**	**Z**	**Occ.**
Li	**4a**	**0.00000**	**0.00000**	**0.00000**	**0.94257**
Co	**4a**	**0.00000**	**0.00000**	**0.00000**	**0.05743**
Li	**4c**	**0.27633**	**0.25000**	**0.99971**	**0.05743**
Co	**4c**	**0.27633**	**0.25000**	**0.99971**	**0.94257**
P	**4c**	**0.09954**	**0.25000**	**0.43276**	**1.00000**
O	**4c**	**0.09951**	**0.25000**	**0.75438**	**1.00000**
O	**4c**	**0.44372**	**0.25000**	**0.22562**	**1.00000**
O	**8d**	**0.17416**	**0.02279**	**0.28619**	**1.00000**

a = 10.1951 Å, b = 5.9201 Å, c = 4.6973 Å , α = β = γ = 90 °
V= 283.510 Å^3, R_{wp}: 2.836%, R_b: 8.274 %

6.3.2. Electrochemical Properties of Polyol-synthesized $LiCoPO_4$ Nanoparticles

The electrochemical properties of the polyol-synthesized $LiCoPO_4$ have been explored by galvanostatic charge-discharge method. The typical voltage profiles at constant 0.1 C rate with cut-off voltage window of 2.8 to 4.95 V are depicted in Figure 6.3(a). The discharge profile exhibited a wide voltage plateau at around 4.75 V *vs.* Li/Li^+ with initial discharge capacity up to 105 mAh/g. One noticeable characteristic of the charging curves is the distinctive two voltage plateaus, corresponding to two-step Li deintercalations.[150-151] This two-step behaviour has been recently reported as Li ion extraction from $LiCoPO_4$ associating with the phase transitions: $LiCoPO_4 \Leftrightarrow Li_{0.7}CoPO_4$ (at ~4.8 V) and $Li_{0.7}CoPO_4 \Leftrightarrow CoPO_4$ (at ~4.9 V), respectively.[128] Polyol synthesis proved that although the first discharge capacity could be improved without conductive carbon addition or surface coating, the obtained discharged capacity is only 63 % of the theoretical value, which is 167 mAh/g after removal of one Li ion. In addition, the severe capacity fade of the $LiCoPO_4$ cathodes in the subsequent cycles is generally observed. The cycling performance of the polyol-synthesized $LiCoPO_4$ nanoparticles was also evaluated as shown in Figure 6.3(b). The discharge capacity is 30 mAh/g at 50th cycle with a constant current of 0.1 C rates. It only maintained 28.57 % of its initial discharge capacity. The drastic capacity fading were observed in the fist 5th cycles, and then the discharge retentions gradually become stable. The low discharge capacity and poor cycling stability of the $LiCoPO_4$ materials are believed due to the presence of antisite defects and the thermodynamic instability of the electrolyte at the high operation voltage close to 5 V *vs.* metallic Li. Thus, the prime challenge is to find out why the drastic capacity loss occurred to solve the problems.

(a)

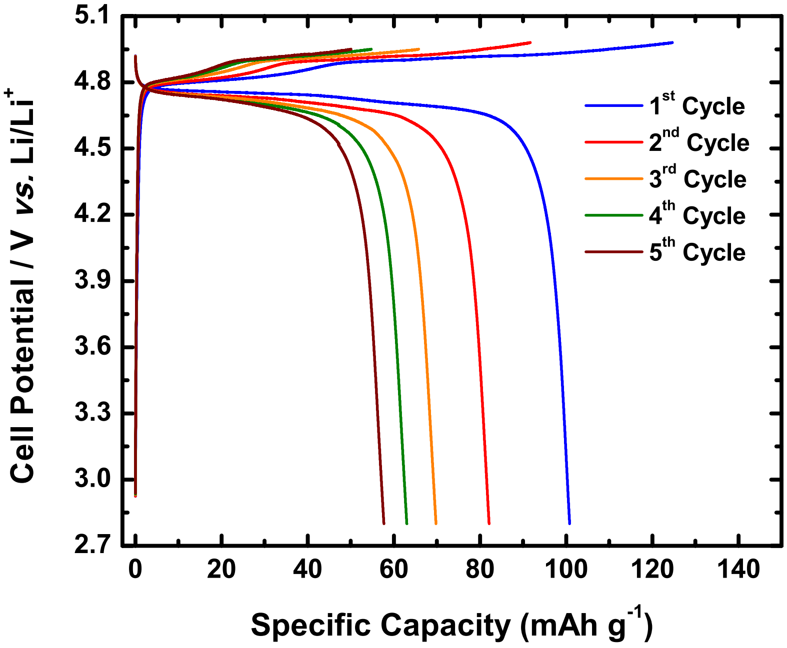

(b)

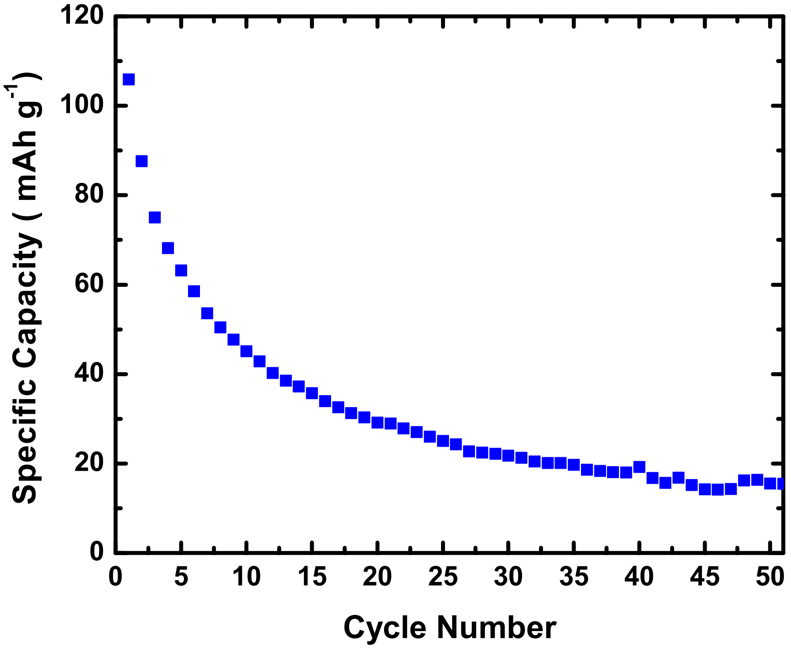

Figure 6.3 (a) Electrochemical charge and discharge voltage profiles between 2.80 and 4.95 V (*vs.* Li/Li$^+$); (b) Dependence of discharging capacity retention on number of cycles, the voltage range is 2.80 - 4.95 V (*vs.* Li/Li$^+$) at 0.1 C = 167 mAh/g

6.3.3. Antisite Defects in Polyol-synthesized $LiCoPO_4$ Nanoparticles

In the octahedrally coordinated cations, Li locates at edge-sharing M1 sites, and Co is found in the corner-sharing M2 sites. The cation exchange antisite defects between theses two octahedral M sites are the most favorable intrinsic point defects in the olivine structure, resulting blocking the Li-ion diffusion pathways.[131, 133] It can directly affect the cathode performance. Previous *P-XRD* refinement results confirmed that the $LiCoPO_4$ nanoparticels synthesized via polyol process have almost 6 % cobalt occupancy on the lithium site. Therefore, we turn to the study on the local variations, transition metal relocation, structural change, and their correlation to the capacity fading during the electrochemical cycling.

Figure 6.4 presents high-angle annular dark-field (HAADF) STEM images viewed along the [010] direction of the as-synthesized $LiCoPO_4$ nanoparitcles in comparison with the electrochemically cycled $LiCoPO_4$ samples. The [010] projection is most suitable to identify the position of Co, P, O and Li with separated aligned columns. The bright contrast produced by Co atoms can be clearly observed in a hexagon configuration under the HAADF STEM mode. The P atomic columns are adjacent to Co site. Because of the distance between them, Co and P could not be distinctively resolved and appear as coma-shaped. Li and O atoms are not sufficiently heavy to produce any contrast and thus are not visible. To make the link with crystal structure of the material, the 2-dimensional (2D) atomic arrangement of a unit cell is overlaid on the STEM images for direct comparison. One can note that the well-crystallized $LiCoPO_4$ olivine materials successfully obtained through the polyol process. However, the 2D atomic arrays are not perfectly matched with the images because of structural distortion of $LiCoPO_4$

nanoparticles. We can assume that the nanosized particles have crystal distortion than the bulk.[132-133] Since the Li atom itself does not produce any intensity, Co_{Li} defects make intensity increase in Li columns. The experimental observation of the samples by the HAAD STEM mode confirmed that few visible contrasts are found in the Li columns, indicating the lower degree of antisite defects in the pristine materials.

To confirm the low capacity and the fading being mainly attributed to the defects in crystal structure, the cathode materials after 30 electrochemical cycles were examined and its HAADF STEM image is shown in Figure 6.4(d). Despite the fact that the discharge capacity of $LiCoPO_4$ was 25 mAh/g at 30th cycle (Figure 6.3(b)), there is little discernible difference in the contrast observed over the Li columns. The contrast comparison further analyzed by line profile for both pristine and cycled samples. The line profiles extracted from the blue boxes are depicted in Figure 6.4(c) and (f). This gives an objective evolution of how much the contrast on the Li atomic column is increasing. These observations clearly indicate that the intensities on the Li site are not drastically changed before and after the cycling, revealing that the amounts of cobalt on the Li site are similar for both materials. The 8.5 % of antisite defects in bulk after cycling are also confirmed through the *ex situ* P-XRD measurement in Figure 6.5 and Table 6.2. This implies that TM relocation of $LiCoPO_4$ is not primarily responsible for the discharge capacity fade of the electrode.

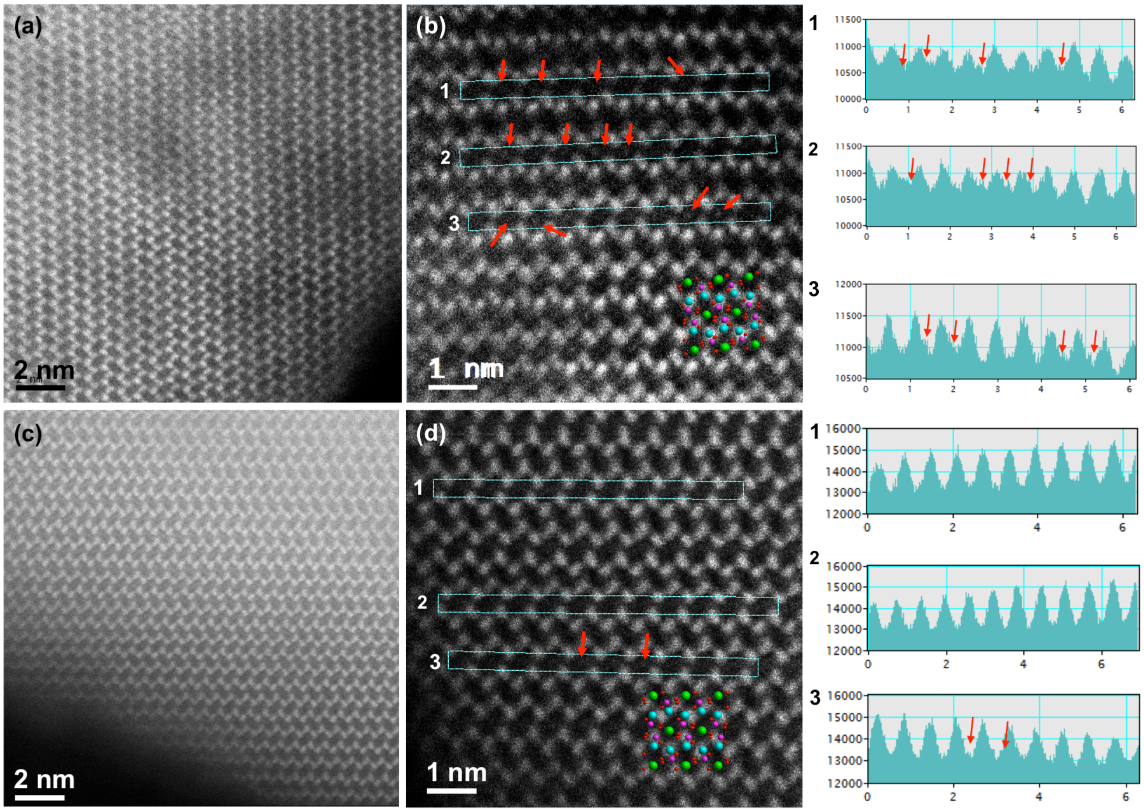

Figure 6.4 (a) High-resolution STEM images of the polyol-sytnehsized $LiCoPO_4$ nanoparticle taken along the [010] zone axis: (a) pristine and (c) after 20th cycles. Line profiles extracted from the areas depicted in the high-magnification images of pristine (b) and after 20th cycles. The schematic crystal structures represent the lithium (green), cobalt (blue), phosphorus (red), and oxygen ions (magenta)

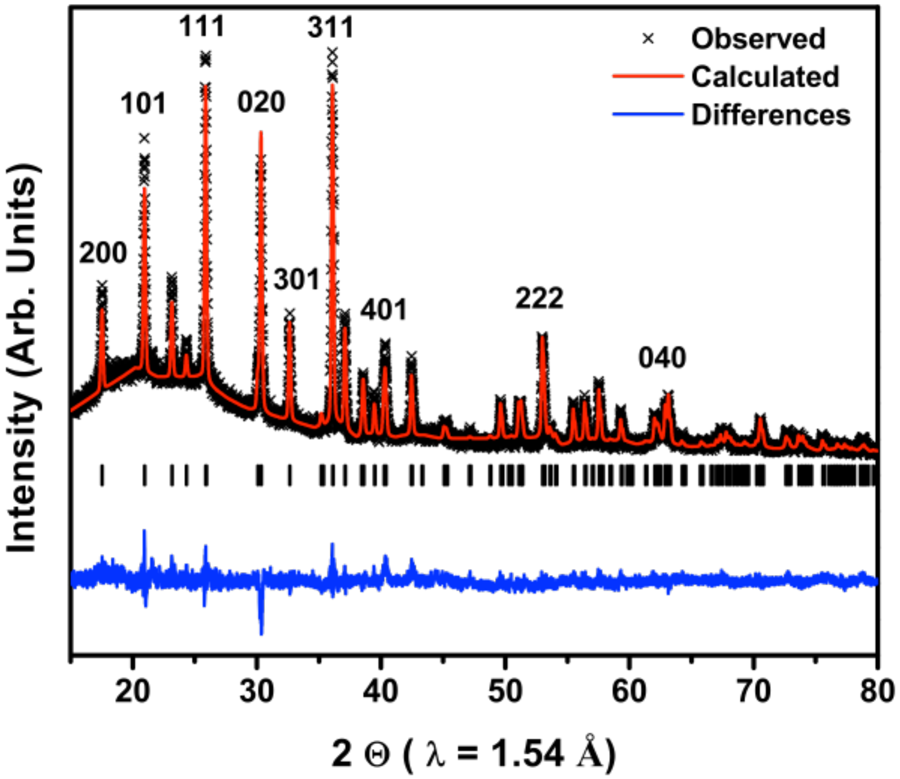

Figure 6.5 The Rietveld refinement results from powder X-ray diffraction patterns collected from the cycled $LiCoPO_4$ composite elctrode. The black crosses represent the observed pattern, the red line corresponds to the calculated diffraction pattern and the blue is the difference pattern

Table 6.2 Lattice parameters, atomic positions and site occupancies result from Rietveld refinement of the cycled $LiCoPO_4$ composite electrode

Atom	**Site**	**X**	**Y**	**Z**	**Occ.**
Li	**4a**	**0.00000**	**0.00000**	**0.00000**	**0.91496**
Co	**4a**	**0.00000**	**0.00000**	**0.00000**	**0.08504**
Li	**4c**	**0.27742**	**0.25000**	**0.98405**	**0.08504**
Co	**4c**	**0.27742**	**0.25000**	**0.98405**	**0.91496**
P	**4c**	**0.09620**	**0.25000**	**0.41784**	**1.00000**
O	**4c**	**0.10460**	**0.25000**	**0.75130**	**1.00000**
O	**4c**	**0.44177**	**0.25000**	**0.20787**	**1.00000**
O	**8d**	**0.17697**	**0.02921**	**0.29144**	**1.00000**

a = 10.1200 Å, b = 5.9188 Å, c = 4.7008 Å , α = β = γ = 90 °
V= 283.798 Å^3, R$_{wp}$: 8.183%, R$_b$: 12.542 %

6.3.4. Co^{2+}/Co^{3+} Redox Reaction and Electrode/Electrolyte Interface

X-ray photoelectron spectroscopy (XPS) measurements were conducted to investigate surface transformations at the cathode in behalf of electrochemical cycling. Typical signals of C1s, O1s, P2p, F1s, and Co2p core levels are detected based on the full scan spectra as shown in Figure 6.6(a)-(d).

Figure 6.6(a) shows Co 2p spectra of the pristine and cycled $LiCoPO_4$ composite electrodes. The Co2p spectra consist of two spin–orbit doublets characteristic, specifically $Co2p_{1/2}$ and $Co2p_{3/2}$ with intensity area ration of bout 2:1.[152-153] Each part consists of a main peak at the binding energy of 781.5 eV and 784.9 eV due to Co^{2+} ion and it also has observable “shake-up” satellite features (identified as “Sat.” in Figure5a).[154] After electrochemical cycling, there are no appreciable changes in the Co2p spectra. It is very close to that of the pristine $LiCoPO_4$ electrode. These results confirm that the Co is almost totally at the +2 oxidation state after a few electrochemical cycles.

The C1s spectra present the main peak at 284.8 eV corresponding to C-C carbon black and other peaks observed at 286.4, 289.2 and 291 eV are attributed to the PVdF binder ($-CH_2-/-CF_2-$, C-O and O=C-C environments of carbon). While no significant difference is observed in these spectra, XPS quantification reveals the 8% of increasing carbonate species after cycling. This can be Li_2CO_3 and/or lithium alkyl carbonate ($ROCO_2Li$), resulting from the decomposition of the electrolyte at the surface of the electrode.[152-153]

Figure 6.6(c) shows O 1s spectra of the pristine and cycled electrode. Both spectra revealed a main peak at 531.6 eV, which is attributed to oxygen atoms of the $(PO_4)^{3-}$ phosphate groups in $LiCoPO_4$ active materials. The spectra of the pristine sample also display a weak component at 533.2 eV assigned to contaminating oxygenated species adsorbed at the surface. The cycled electrode shows a noticeable increase of the high binding energy component at ~534 eV. This is expected spectrum for oxygenated species and Li alkyl carbonates deposited at the electrode/electrolyte interface resulting from electrolyte degradation.

The P 2p spectrum shown in Figure 6.6(d) present $2p_{3/2}$ and $2p_{1/2}$ doublet separated by ~0.9 eV with the $2p_{3/2}$ at 133.4 eV. The observation of only one P 2p doublet confirms the presence of one environment for the $(PO_4)^{3-}$ phosphate group of $LiCoPO_4$. While cycled $LiCoPO_4$ cathode still retains the main peak components of the P 2p spectrum, the increased of another peak at higher binding energy (~136 eV) can be noticed. It can correspond to the appearance of a partially fluorinated environment of phosphorus; $Li_xPO_yF_z$ of $Li_xPF_yO_z$, also from the degradation of either $LiPF_6$ or PF_5 salt respectively.[112]

Figure 6.6(e) shows the corresponding F 1s spectra of the pristine and cycled electrode. A drastic change is observed after electrochemical cycling. Both the spectra display unique peak at 687.7 eV attributed to the PVdF binder. However a significant additional peak at 685.2 eV appears at surface of the cycled electrode, which can be easily assigned to LiF, the major degradation compound of the salt $LiPF_6$. The amount of LiF deposited at the surface of the electrode is 64.57 %. This result suggests that the low capacity and the fading being possibly attributed to the electrolyte instabilities upon cycling.

(a)

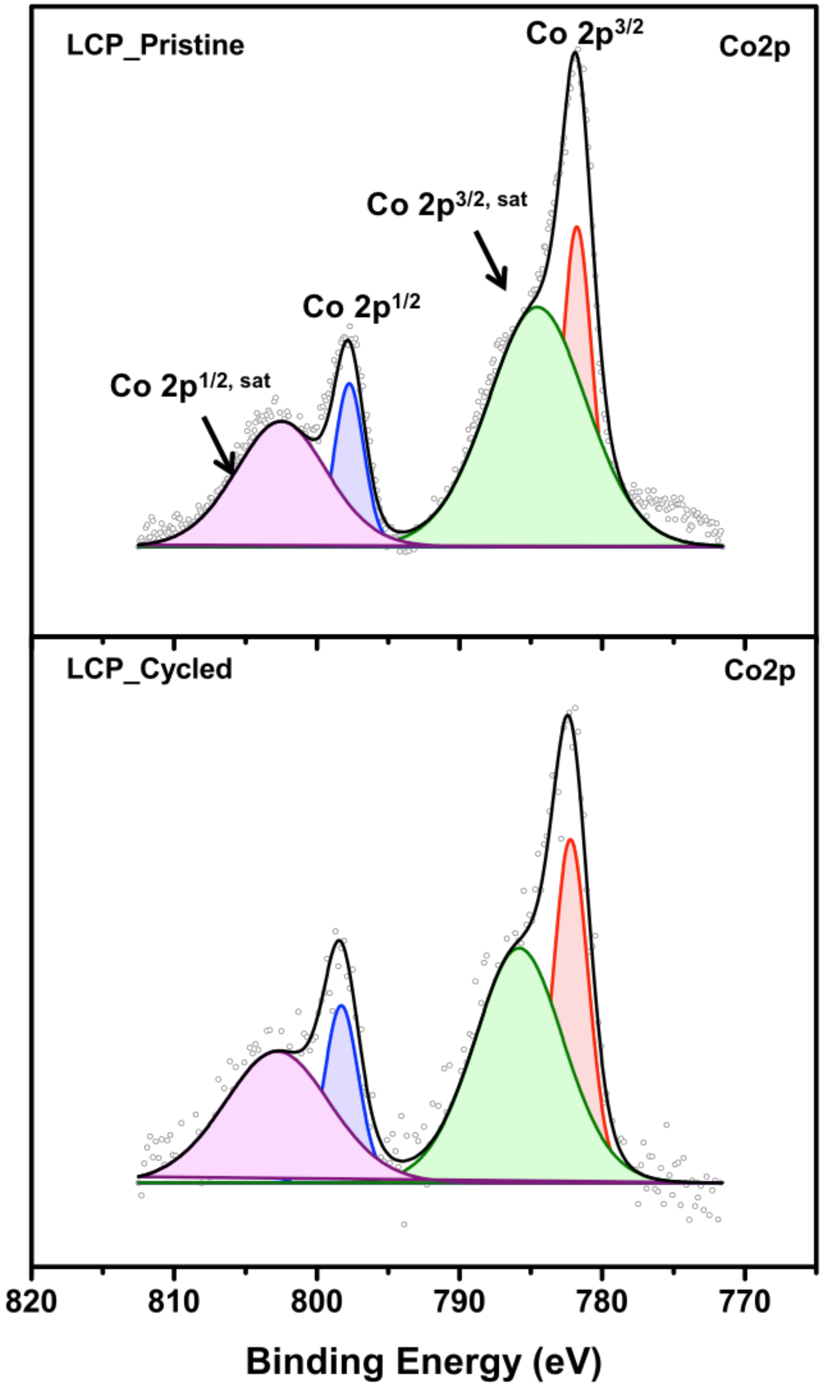

Figure 6.6 (a)-(e) XPS results for the Co2p, C1s, O1s, P2p, and F1s region scans of the pristine and cycled $LiCoPO_4$ composite electrode

(b)

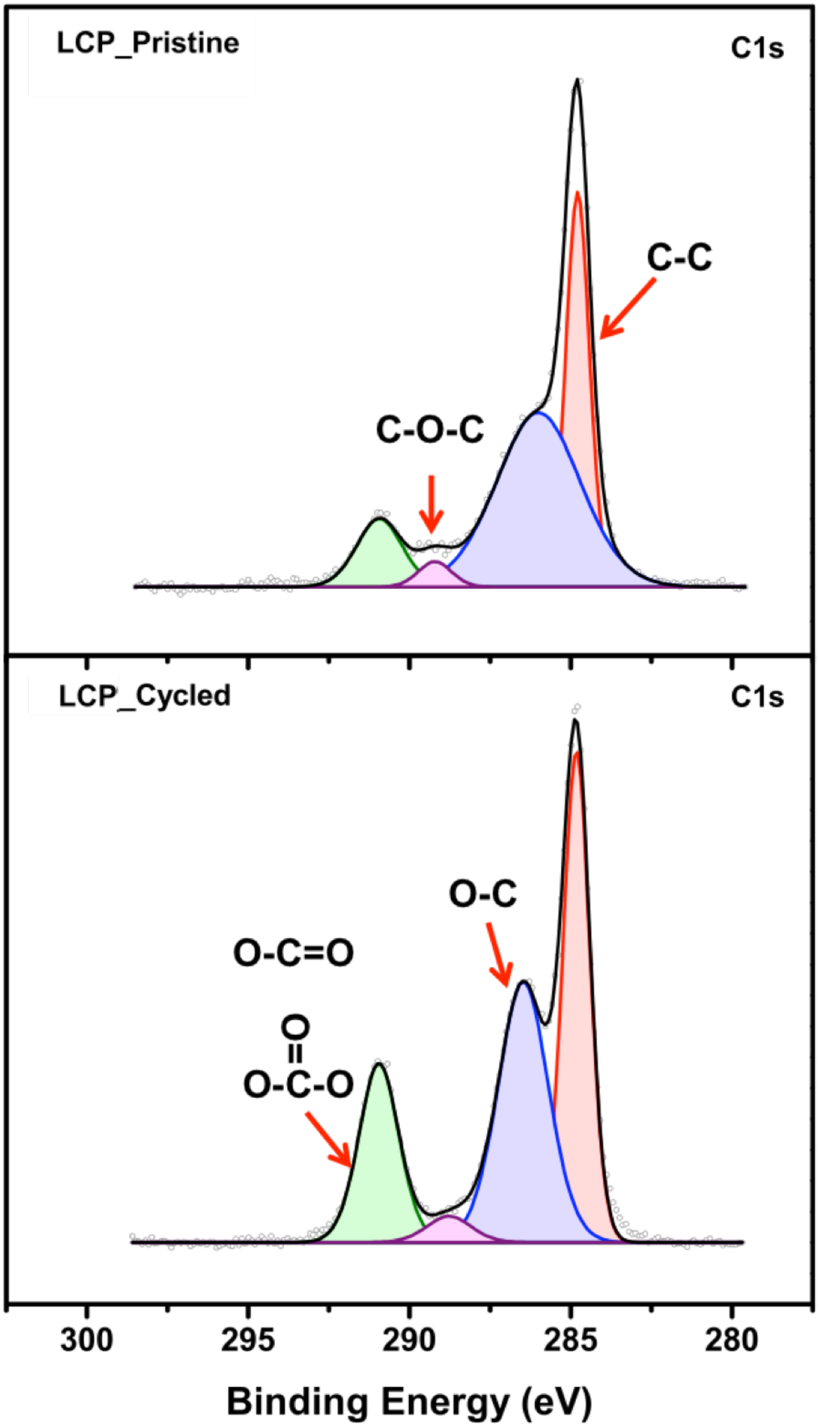

Figure 6.6 (a)-(e) XPS results for the Co2p, C1s, O1s, P2p, and F1s region scans of the pristine and cycled $LiCoPO_4$ composite electrode (continued)

(c)

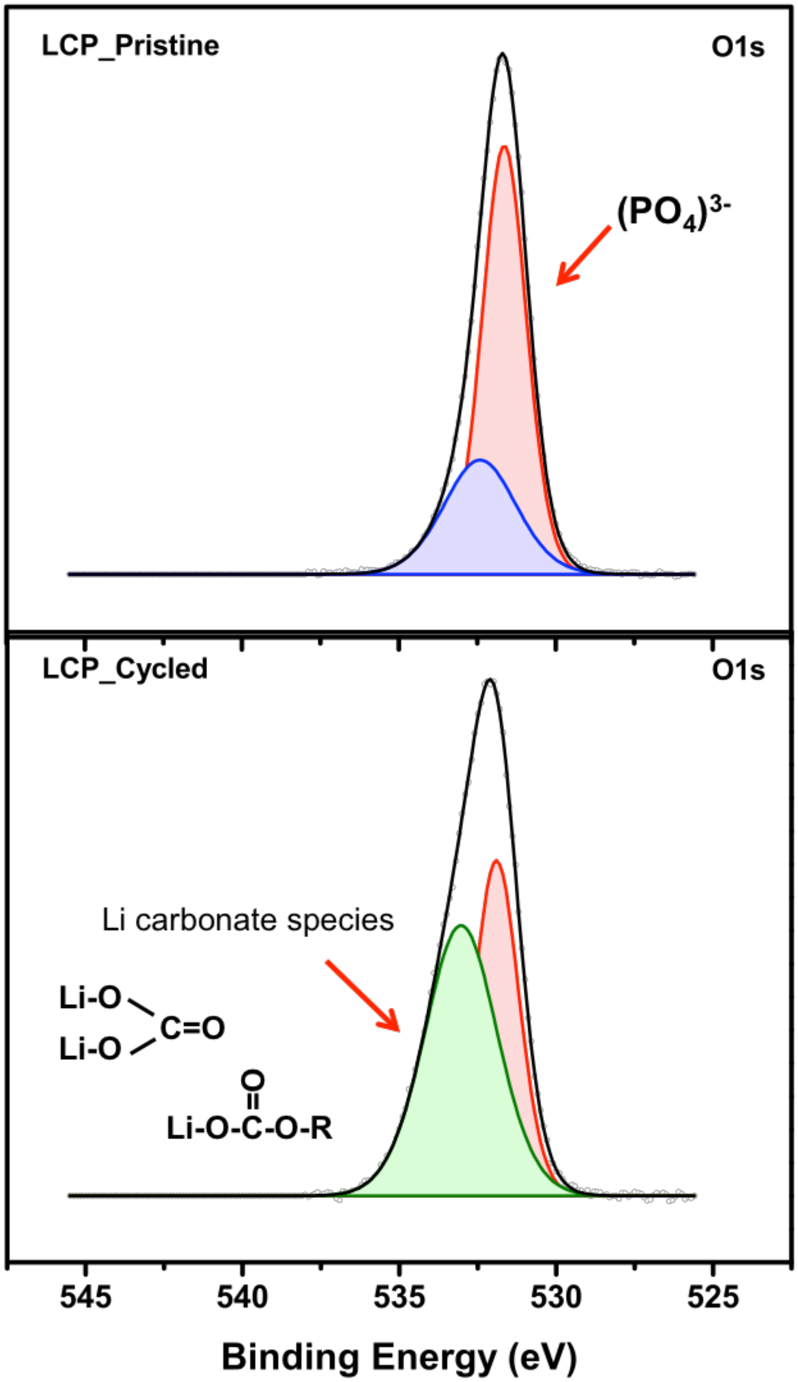

Figure 6.6 (a)-(e) XPS results for the Co2p, C1s, O1s, P2p, and F1s region scans of the pristine and cycled $LiCoPO_4$ composite electrode (continued)

(d)

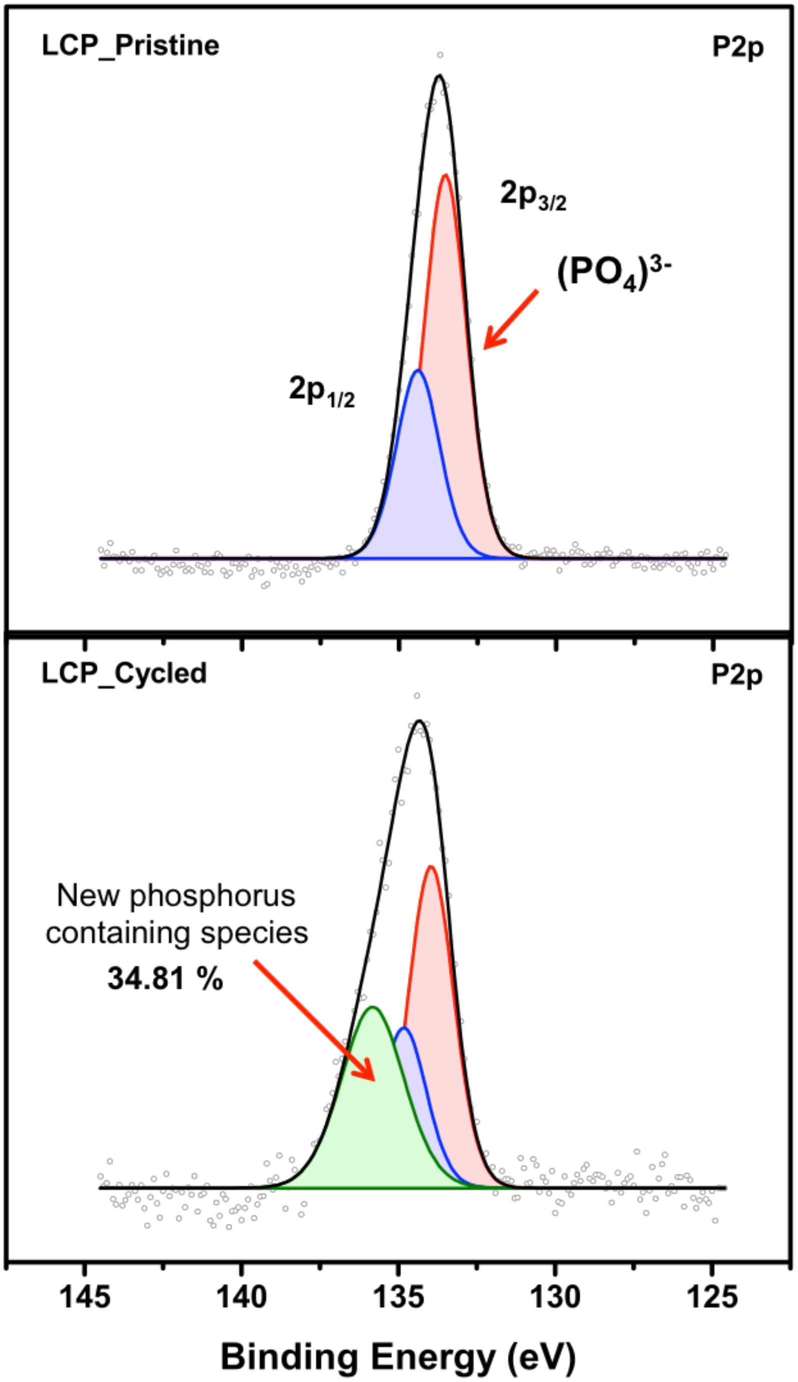

Figure 6.6 (a)-(e) XPS results for the Co2p, C1s, O1s, P2p, and F1s region scans of the pristine and cycled $LiCoPO_4$ composite electrode (continued)

(e)

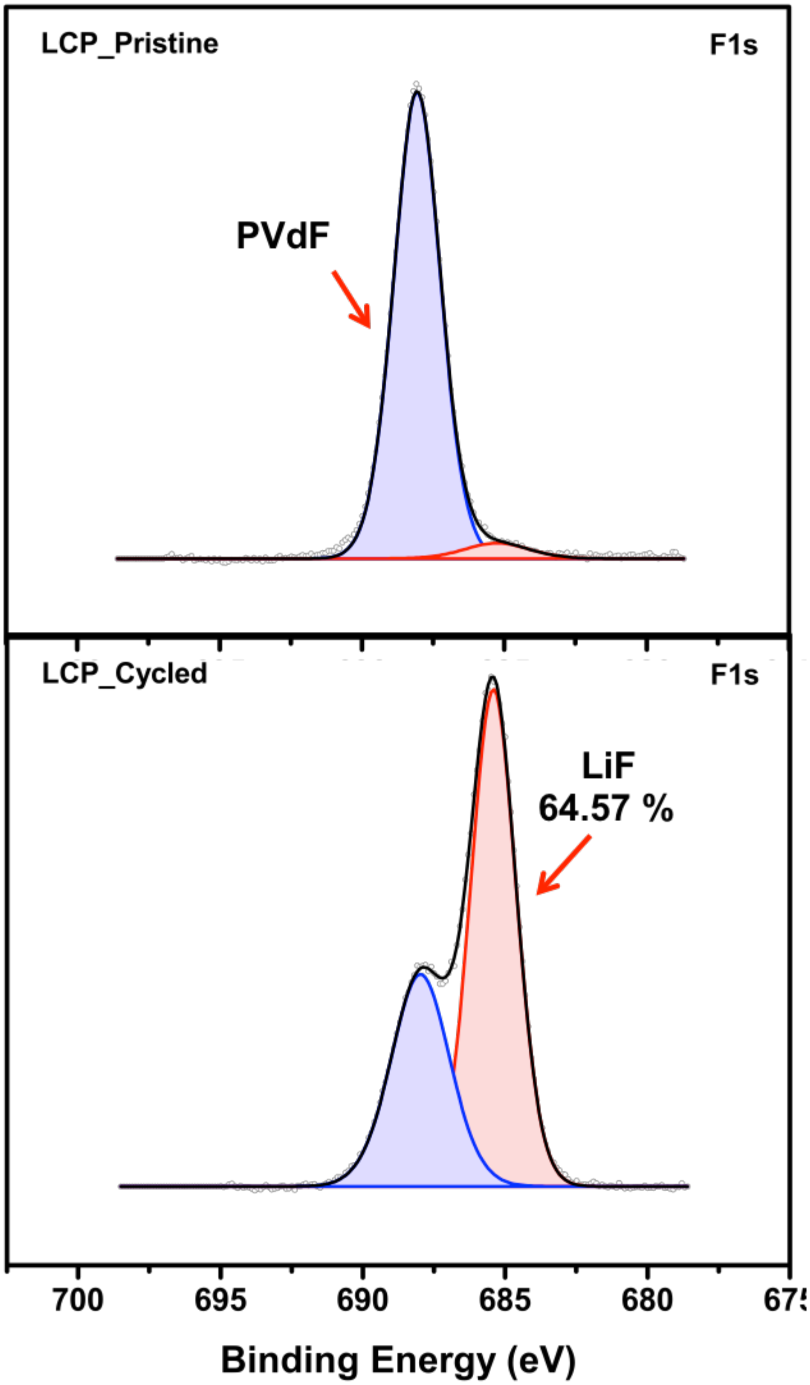

Figure 6.6 (a)-(e) XPS results for the Co2p, C1s, O1s, P2p, and F1s region scans of the pristine and cycled $LiCoPO_4$ composite electrode (continued)

6.4. Conclusion

In summary, we demonstrated a polyol process for the synthesis of $LiCoPO_4$ nanoparticels for high-voltage cathode materials. Pure phase olivine structured $LiCoPO_4$ have been successfully synthesized and their electrochemical performances were investigated in conventional organic electrolyte. Despite of the improved charge-discharge capacity of the material without any conductive surface coating, capacity fade during cycling is still significant. Atomic resolution HAADF STEM and surface sensitive XPS analysis reveal the structural and electrode/electrolyte interface evolution at the surface. Through the direct observation of Li-to-Co antisite exchange defects combining with XRD refinements, it can be confirmed that both the pristine and cycled materials do not contain any antisite defects in a significant proportion (i.e., pristine < 6% and cycled < 9%). Whereas, XPS analysis prove the increasing amount of Li alkyl carbonate species (Li_2CO_3 and/or CH_3OCO_2Li) and LiF upon cycling. These results suggest that the greater capacity fading under cycling might be due to the acceleration of the degradation of conventional electrolyte. Further work would include the investigation on the intrinsic evidence for phase transformation (LiCoPO4 – $Li_{2/3}CoPO_4$ – $CoPO_4$) and catalyzing electrolyte deterioration of the $LiCoPO_4$ lithium-ion battery system.

Chapter 6, in full, is currently being prepared for submission for publication of the material “Probing Defects and Electrochemical Properties in Polyol Synthesized High Voltage $LiCoPO_4$ Olivine Materials” Hyojung Yoon, Jessie Lin, Mahsa Sina, Hyeseung Chung, Jim Ciston, and Ying Shirley Meng. The dissertation author was the co-primary investigator and author of this paper. All the experiment parts were performed by the author.

Chapter 7. Probing the Surface Structure of Polyol-syntehsized High Energy $LiNi_xCo_yMn_zO_2$ Layered Cathode Material ($x + y + z = 1$)

7.1. Introduction

The widespread use of oxide materials in the present generation of automotive batteries is motivated by the favorable balancing between capacity, rate capability, voltage, and density.[155] It is then not surprising that, also among the future generation of cathode materials, some of the most promising candidates still belong to this family. Currently, among the classical layer-structured metal oxide positive electrode in Li-ion batteries, three-component layered $LiNi_xCo_yMn_zO_2$ (NCM, $x+y+z =1$) has received great attention because of its high theoretical capacity depending on the composition of Ni, Co and Mn in the structure and competitive cost. Theoretically, the current generation of layered oxide materials is capable of meeting future energy storage demands by increasing the operating voltages. To acquire high capacity from NCM layered materials, operation in the high-voltage range (≈ 4.7 V) is required, which inevitably results in rapid capacity fade over numerous cycles. It is found that the high voltage operation in NCM is accompanied by the structural transformations resulting capacity fading issue. Electron microscopy studies have revealed the structural reconstruction, from *R3m* layered to *Fd3m* spinel and/or *Fm3m* rock-salt structures, occurs at the surface of NCM material.[156] This directly attributes to the capacity fading and the voltage decay with cycling.

Previously, our group has developed the polyol process to prepare $LiNi_{0.5}Mn_{1.5}O_4$ (*P*-LNMO) spinel material as a high-voltage cathode with the outstanding cyclability. Using the double aberration-corrected scanning TEM (TEAM 0.5 at NCEM), we have observed a dramatic improvement in the surface structural stability compared to those prepared by conventional sol-gel method. In this work, we have extended the polyol method to synthesize the high energy NCM (HE-NCM) materials. It is expected that, similar to *P*-LNMO, the polyol process help to prevent the structural changes occurring at the surface with prolonged cycling at high cut-off voltage window. To solve the long-term stability issues associated with the high-voltage operation, the surface reconstruction and the chemical evolution need to be addressed.

7.2. Experimental

To synthesize various stoichiometric HE-NCM cathode materials, $Ni(CH_3COO)_2{\cdot}4H_2O$, $Mn(CH_3COO)_2{\cdot}4H_2O$, $Co(CH_3COO)_2{\cdot}4H_2O$ and $LiOH{\cdot}H_2O$ (all chemicals from Sigma-Aldrich), and citric acid were added to 100 ml of tetraethylene glycol (TTEG) in a stoichiometric molar ratio. Then, the heat was applied to the mixture in a round bottom flask with constant stirring. The mixture was heated up to 230 °C for 4 h in a round bottom flask connected to a refluxing condenser. The resulting solution was centrifuged several times with ethanol, before being dried at 80 °C for the next 10 hours. After, the resulting precursors were decomposed at 450 °C for 12 hours in air. Then, the powder was made into one or two pellets before being calcinated at 800 °C for 12 hour in air again.

Electrochemical discharging and charging process were performed using coin-type (2016) cells. The working electrodes were composed of polyol synthesized HE-NCM as an active material, acetylene black and PVDF at a weight ratio of 80:10:10. Pure lithium metal was used was used for anode, while Celgard model C480 separator

(Celgard Inc., US) was used as a separator. For the electrolyte, 1- M solution of lithium hexafluorophosphate ($LiPF_6$) in a 1:1 volume mixture of ethylene carbonate (EC) and dimethyl carbonate (DMC) was utilized. Finally, the cell used for the electrochemical tests was assembled in a glove box (H_2O level of <1 ppm) (MBraun, Germany) filled with purified argon gas. The prepared cell was charged and discharged between constant potential of 2.50 V and 4.7 V (*vs*. Li/Li^+) at a rate of 1C and C/10, which was calculated based on the theoretical specific capacity of 200 mAh/g.

Powder x-ray diffraction for the synthesized materials were collected by laboratory x-ray diffractometer (XRD, Bruker D8) with a Cu K_α radiation. The data were collected with continuous scanning of a detector covering an angular range from 10.0 ° to 80.0°. The scanning rate was $0.02° s^{-1}$ with wavelengths of λ= 1.54 Å. Then, the collected data were refined with Fullprof. XPS was performed using a Kratos Ultra DLD XPS. Analysis of the spectra closely followed previous work, with fitting performed by CasaXPS software (version 2.3.15, Casa Software Ltd.).

7.3. Results and Discussion

To investigate the structural properties of the materials, the XRD patterns were collected as shown in Figure 7.1. The layered $LiNi_{1/3}Co_{1/3}Mn_{1/3}O_2$ (NCM333) has the space group, *R3m* and trigonal crystral structure. This structure has Li-ions at the 3a, the transition metal ions (M = Mn, Co, Ni) at 3b and O ions at 6c sites. The Rietveld refinement patterns of the XRD obtained from polyol synthesized (*P*-) and commercial (*C*-) NCM333 from the MTI Corp. exhibit a good agreement with those reported in the literatures. Table 1 and 2 show the lattice parameters, atomic positions and site occupancies result from the Rietveld refinements. The cation mixing of lithium and nickel for the *P*-NCM333 is 3.2 %, which is lower than that for the commercial one form MTI Corp., 4.4 %.

Representative morphologies of the *P*-NCM333 powders and *C*-NCM333 are shown in the scanning electron micrograph (SEM) images of Figure 7.2 and 3, respectively. The average particle size of the *P*-NCM333 powders was approximately 200 nm. They are homogeneously dispersed and no secondary particles were observed, while around 10 μm secondary particles were major in the *C*-NCM333 powders.

Figure 7.4 shows the electrochemical charge and discharge voltage profiles between 2.50 and 4.70 V (vs. Li/Li+) with applied current of 1C rates of both *P*-NCM3333 and *C*-NCM333. Both powders show the typical electrochemical behavior of the NCM layered material. The initial discharge capacities are measured as 170 and 140 mAh/g for *P*-NCM333 and *C*-NCM333 respectively. This discrepancy is ascribed to the different cation mixing with lithium and nickel sites as mentioned in the XRD refinements. Figure 7.5 presents the relation between specific capacity and cycle number of *P*- and *C*-NCM333 materials at the rate of C/10. Initially, the *C*-NCM333 powder had larger capacity, but the capacity fading occurs with the following charge and discharge cycles. It shows that increasing the charge cutoff voltages led to higher reversible capacities for the first few cycles, followed by faster capacity degradation in case of *C*-NCM333. It is also noticeable that the Coulombic Efficiency (C.E.) of *C*-NCM333 is only 90 % during extended cycles. On the other hand, even though *P*-NCM333 powder also exhibits capacity fading for the first few cycles, it seems to stabilize from around 20th cycle with 99% of its C.E..

Figure 7.6 shows the resulting x-ray photoelectron spectroscopy (XPS) spectra for the Ni2p region scans on the pristine and cycled samples of *C*-NCM333 (a) and *P*-NCM333 (b). The Ni2p region scans both have a main peak at ~ 854.5 and 872.1 eV corresponding to two spin-orbit doublets characteristic from Ni2p$_{1/2}$ and Ni2p$_{3/2}$ with intensity area ratio of about 2:1. Ni^{2+}. No noticeable difference is observed in the Ni2p scans from pristine samples. However, the XPS spectra of cycled *C*-NCM333 and *P*-NCM333 are drastically changed. The binding energy peaks for cycled *C*-NCM333 correspond to NiO 2p3/2 and 2p1/2, respectively. It can assume that the surface of the NCM333 particles underdoes severe phase transformation upon electrochemical cycling.

7.4. Conclusion

In this work, the electrochemical properties of $LiNi_{1/3}Co_{1/3}Mn_{1/3}O_2$ (NCM333) layered materials synthesized from the polyol process were investigated and compared with commercially available NCM333 powders from MTI Corp.. The polyol process allows for the synthesis of nanoparticles without the formation of lattice defects, which is difficult to avoid with typical low temperature synthetic methods usually necessary to obtain nanoparticles. The structural and compositional properties of *P*-NCM333 were investigated by XRD refinement. It proved that the properties of both *P*- and *C*-NCM333 powders are almost identical each other but *P*-NCM333 showed stabilized cycling performance after first 20th cycles. XPS analysis revealed that *C*-NCM333 undergoes much severe phase transformation in terms of Ni phase. It is believed that when the NCM electrode is cycled with a 4.7 V cutoff, the highly oxidative environment promotes the formation of the rock salt phase more universe. We believe that these new phases are critical to the increase in charge transfer resistance and the presence of the ionically blocking rock salt phase at the surface inhibits the motion of Li ions.

Chapter 7, in part, is currently being prepared for submission for publication of the material “Probing the Surface Structure of Polyol Syntehsized High Energy $LiNi_xCo_yMn_zO_2$ Layered Cathode Material ($x + y + z = 1$)”. Hyeseung Chung, Hyojung Yoon, Jessie Lin, and Ying Shirley Meng. The dissertation author was the co-investigator and co-author of this material.

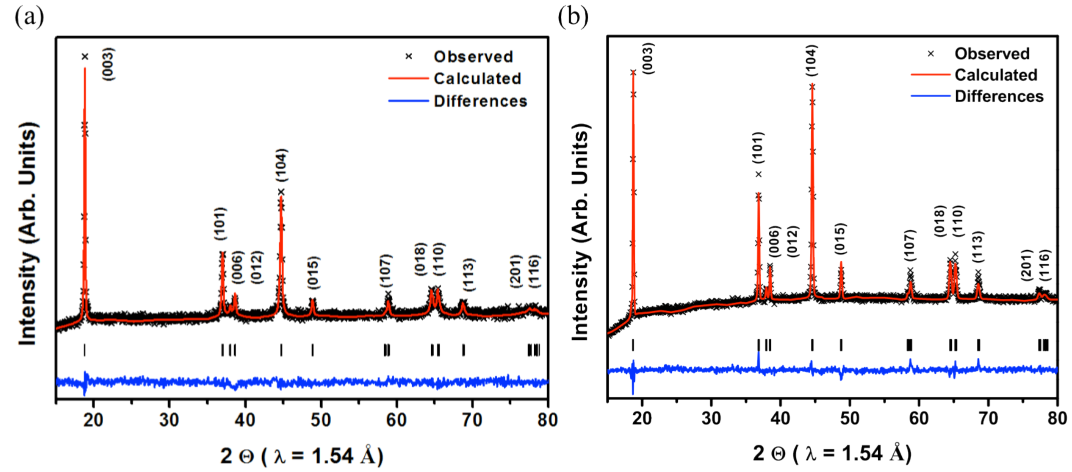

Figure 7.1 The Rietveld refinement results from powder X-ray diffraction patterns collected from the *P*-NCM333 (a) and *C*-NCM333 powders. The black crosses represent the observed pattern, the red line corresponds to the calculated diffraction pattern and the blue is the difference pattern

Table 7.1 Lattice parameters, atomic positions and site occupancies result from Rietveld refinement of the *P*-NCM333 powders

Atom	**Site**	**X**	**Y**	**Z**	**Occ.**
Li	**3a**	**0.00000**	**0.00000**	**0.00000**	**0.96781**
Ni	**3a**	**0.00000**	**0.00000**	**0.00000**	**0.03219**
Li	**3b**	**0.00000**	**0.00000**	**0.50000**	**0.03219**
Ni	**3b**	**0.00000**	**0.00000**	**0.50000**	**0.29781**
Co	**3b**	**0.00000**	**0.00000**	**0.50000**	**0.33000**
Mn	**3b**	**0.00000**	**0.00000**	**0.50000**	**0.33000**
O	**6c**	**0.00000**	**0.00000**	**0.25795**	**2.00000**

a =b = 2.8552 Å, c = 14.2365 Å , α = β = 90 °, γ = 120 °

R_{wp}: 2.39%, R_b: 10.78 %

Table 7.2 Lattice parameters, atomic positions and site occupancies result from Rietveld refinement of the *C*-NCM333 powders

Atom	Site	X	Y	Z	Occ.
Li	3a	0.00000	0.00000	0.00000	0.95564
Ni	3a	0.00000	0.00000	0.00000	0.04436
Li	3b	0.00000	0.00000	0.50000	0.04436
Ni	3b	0.00000	0.00000	0.50000	0.28564
Co	3b	0.00000	0.00000	0.50000	0.33000
Mn	3b	0.00000	0.00000	0.50000	0.33000
O	6c	0.00000	0.00000	0.24935	2.00000

a =b = 2.8568 Å, c = 14.2139 Å , α = β = 90 °, γ = 120 °

R_{wp}: 1.82 %, R_b: 10.19 %

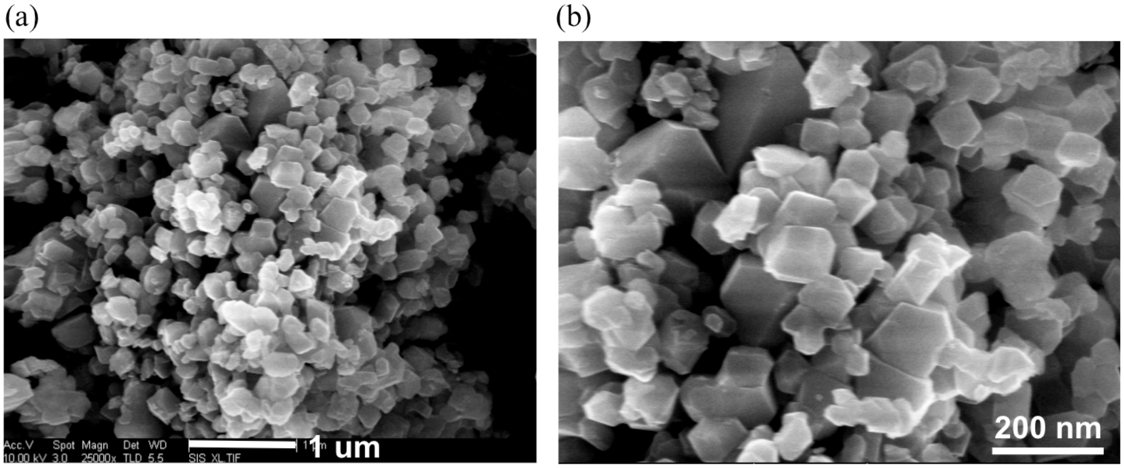

Figure 7.2 SEM images of *P*-NCM333 powders synthesized via a polyol process at low (a) and high (b) magnifications

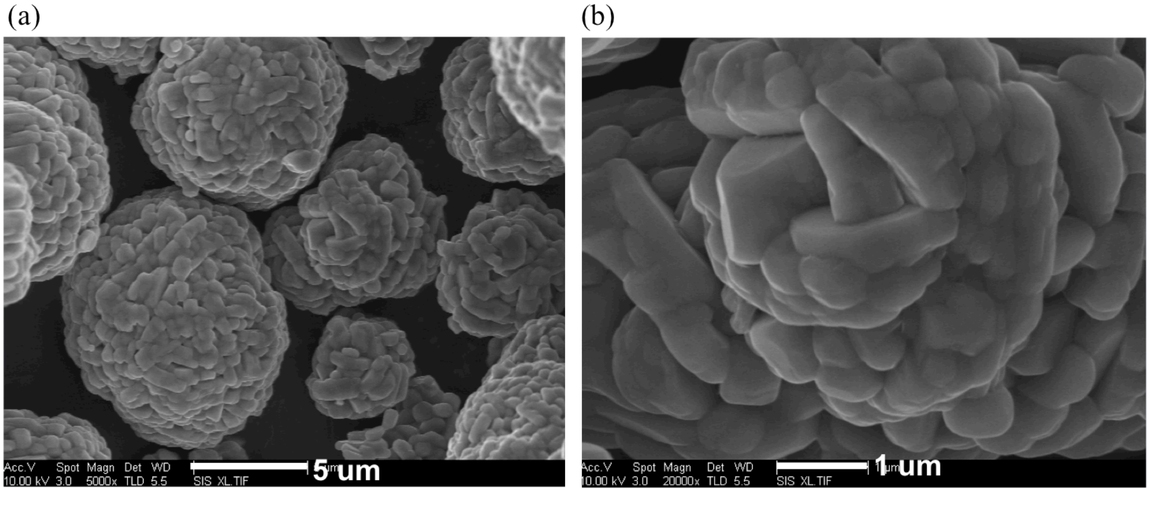

Figure 7.3 SEM images of *C*-NCM333 powders synthesized via a polyol process at low (a) and high (b) magnifications

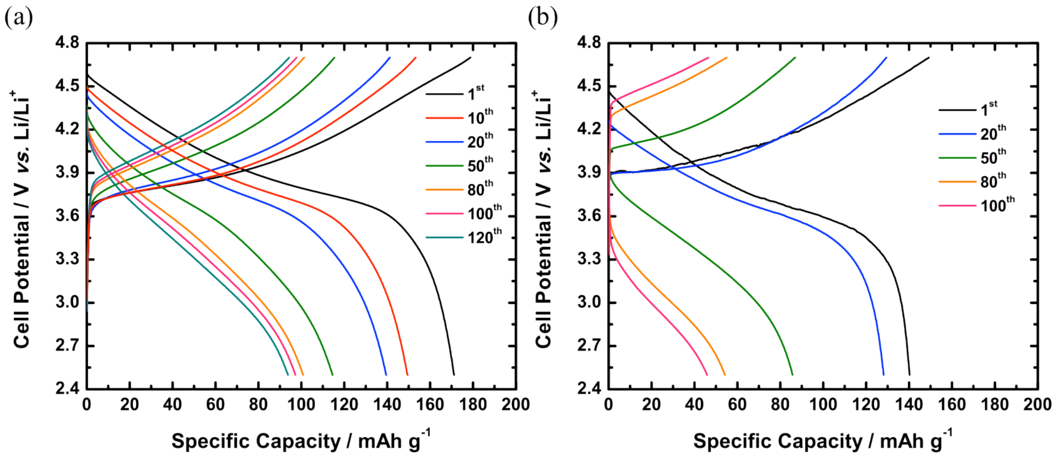

Figure 7.4 Electrochemical voltage profiles of *P*-NCM333 (a) and *C*-NCM333 materials between 2.50 and 4.70 V (vs. Li/Li$^+$)

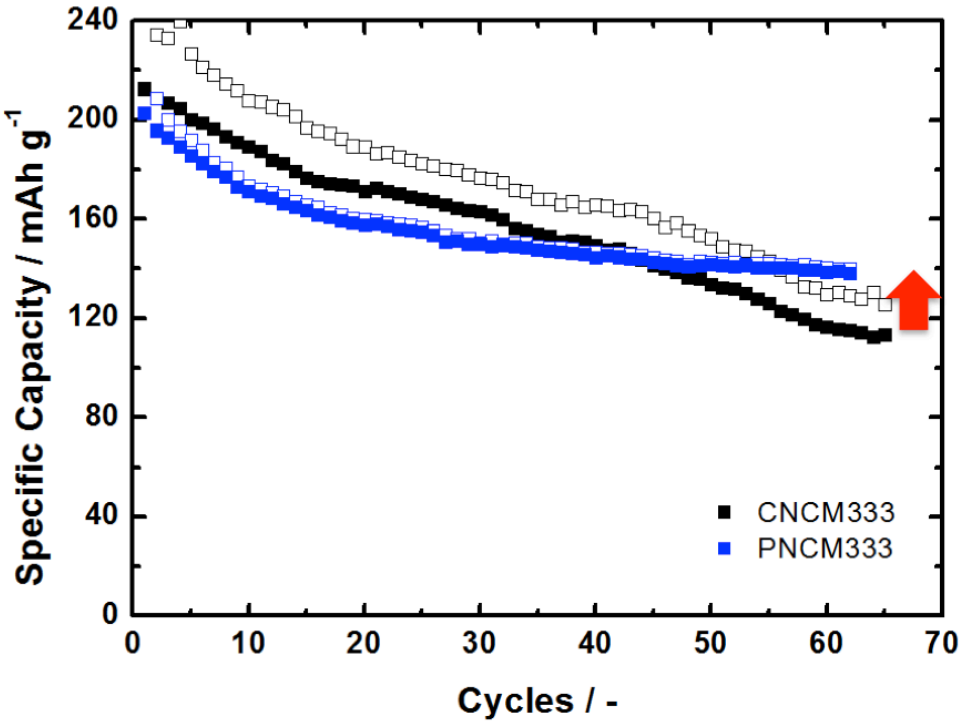

Figure 7.5 Dependence of discharging capacity retention on number of cycles, the voltage range is 2.50 - 4.70 V (*vs.* Li/Li$^+$) at 0.1 C

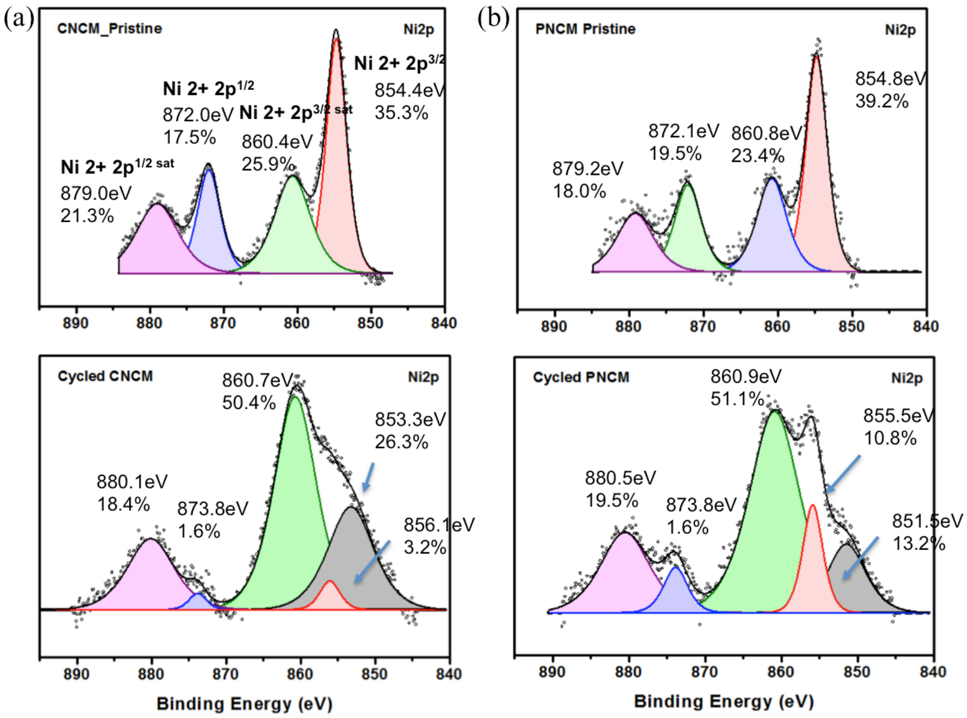

Figure 7.6 XPS results for the Ni2p region scans of the *C*-NCM333 (a) and *P*-NCM333 (b) composite electrode

Chapter 8. Summary and Future Work

8.1. Summary

In this study, the influence of synthetic conditions on the polyol process for high energy high power energy materials are investigated in terms of their electrochemical and structural properties.

In the first part, the nucleation and growth kinetics of a non-aqueous high temperature polyol process for the formation of cobalt carbide nanoparticles were investigated. A nanostructured cobalt carbide (NCC) consisting of an assembly of Co_2C and Co_3C nanoparticles are developed. The resulting material has an energy product of greater than 5 MGOe at room temperature, which is a dramatically improved coercivity compared to pure bulk material. To understand the formation mechanism of the Co_2C and Co3C systems and their associated high-energy product and large anisotropy, *in situ* quick-XAS was used and the nucleation and growth kinetics of cobalt carbide polyol synthesis were proved. These findings will be of high importance to not only the spectroscopy community but also those interested in nucleation/growth of nanomaterials as well as those interested in developing next generation magnetic materials.

In the second part, $LiNi_{0.5}Mn_{1.5}O_4$, $LiCoPO_4$, and $LiNiCoMnO_2$, for high energy density cathode materials in LiBs, have been prepared through the polyol process as a novel synthesis method and their structural and electrochemical properties have been also investigated. The resulting materials synthesized from the polyol method shows outstanding capacity retention compared to those prepared from conventional synthesis methods: this is mainly due to mitigating the surface structural instability and promoting well-maintained original structure during the lithiation/delithiation process. Their bulk and surface local atomic structural and chemical evolution before/after cycling have been investigated by using double aberration-corrected STEM in atomic resolution. On the basis of the combined results of *in situ* XAS and STEM studies, it was found that the atomic structural transformation on the surface of active materials is the main source of the TM dissolution problem.

This study verified that the drawback of the nanosized high voltage cathode materials could be resolved with a new synthesis method, polyol process. The direct confirmation of the structural transformation and decomposition of the conventional electrolyte on the surface, presented in this work, provides novel insight into how to design and optimize this material.

8.2. Future Work

The development of the high performance, low cost and environmentally friendly portable power sources is crucial for the zero-emission transportation and energy back-up technologies. Even though this study presents the most promising high energy cathode materials, achieving stability of the material structures and good cycle performance at high voltage and temperature operating conditions, it is not adequate yet to meet the requirements of advanced applications such as electric vehicles. An additional point that needs to be certainly stressed is that the goal achievement on cell level is strongly depended on the choice of anode. Independent of the cathode potential to meet the targets, fabricating a cell without a paired high energy anode will always lead to decreased capacities and hence lower driving ranges.[157] Therefor, in-depth study on full-cell level is required. On the other hand, development of new electrochemical systems and next-generation batteries with higher energy density are also desired. For instance, lithium-air and lithium-sulfur batteries, are considered promising alternatives.

8.2.1 Irreversible Capacity Loss of High Voltage $LiCoPO_4$

It is proven that the antisite defects in $LiCoPO_4$ are not significantly affected their irreversible capacity loss in this study. Other significant issues are still under debating: the irreversible electrolyte decomposition that occurs at higher voltages and structural decomposition, $LiCoPO_4/CoPO_4$. Some reported researches that Fe-doped $LiCoPO_4$ performs significantly better than neat $LiCoPO_4$ by stabilizing the cathode structure and improving the electronic conductivity of the material. These structural changes, however, do not solve the problem of perpetual electrolyte decomposition that leads to polarization and loss of cycleable lithium. In order to promote a low resistance passivation layer that prevents electrolyte decomposition, studies on electrolyte additives need to be incorporated.

8.2.2 Surface and Interface Properties of High Energy $LiNi_xCo_yMn_zO_2$

Theoretically, the current generation of layered oxide materials is capable of meeting future energy storage demands by increasing the operating voltages. In this study, the polyol process can prepare high energy $LiNi_xCo_yMn_zO_2$ (HE-NCM) layered cathode materials with the outstanding cyclability. However, it is not proved that the structural transformations directly attributes to the capacity fading and the voltage decay with cycling. It needs to further investigate how the high voltage operation in HE-NCM is accompanied by the structural or phase transformations resulting capacity fading issue. Especially, the degradation mechanism of different compositions HE-NCM can be differed, which involves the formation of the O1 phase in the highly delithiated state.[158] This indicated that the degradation mechanisms of the HE-NCM material should be carefully considered for different compositions. Experimental side, XAS and atomic resolution STEM/EELS analysis need to conduct in order to dig deeper into the relationships between structural changes, such as the bonding, electronic properties of the interface.

References

1. Tarascon, J. M.; Armand, M., Issues and challenges facing rechargeable lithium batteries. *Nature* **2001,** *414* (6861), 359-367.

2. Dunn, B.; Kamath, H.; Tarascon, J. M., Electrical Energy Storage for the Grid: A Battery of Choices. *Science* **2011,** *334* (6058), 928-935.

3. Service, R. F., Getting There. *Science* **2011,** *332* (6037), 1494-1496.

4. Rolison, D. R.; Nazar, L. F., Electrochemical energy storage to power the 21st century. *MRS Bull.* **2011,** *36* (07), 486-493.

5. Fergus, J. W., Recent developments in cathode materials for lithium ion batteries. *Journal of Power Sources* **2010,** *195* (4), 939-954.

6. Whittingham, M. S., Lithium batteries and cathode materials. *Chem Rev* **2004,** *104* (10), 4271-4301.

7. Etacheri, V.; Marom, R.; Elazari, R.; Salitra, G.; Aurbach, D., Challenges in the development of advanced Li-ion batteries: a review. *Energ Environ Sci* **2011,** *4* (9), 3243-3262.

8. Strnat, K.; Hoffer, G.; Olson, J.; Ostertag, W.; Becker, J. J., A Family of New Cobalt-Base Permanent Magnet Materials. *J Appl Phys* **1967,** *38* (3), 1001-&.

9. Strnat, K. J.; Strnat, R. M. W., Rare-Earth Cobalt Permanent-Magnets. *J Magn Magn Mater* **1991,** *100* (1-3), 38-56.

10. Sugimoto, S., Current status and recent topics of rare-earth permanent magnets. *J Phys D Appl Phys* **2011,** *44* (6).

11. Herbst, J. F., R2fe14b Materials - Intrinsic-Properties and Technological Aspects. *Rev Mod Phys* **1991,** *63* (4), 819-898.

12. Herbst, J. F.; Croat, J. J., Magnetization of R6fe23 Intermetallic Compounds - Molecular-Field Theory Analysis. *J Appl Phys* **1984,** *55* (8), 3023-3027.

13. Herbst, J. F.; Croat, J. J.; Vanlaar, B.; Yelon, W. B., Magnetic-Structure of Er6fe23. *J Appl Phys* **1984,** *56* (4), 1224-1226.

14. Sagawa, M.; Fujimura, S.; Togawa, N.; Yamamoto, H.; Matsuura, Y., New Material for Permanent-Magnets on a Base of Nd and Fe. *J Appl Phys* **1984,** *55* (6), 2083-2087.

15. Kramer, M. J.; McCallum, R. W.; Anderson, I. A.; Constantinides, S., Prospects for Non-Rare Earth Permanent Magnets for Traction Motors and Generators. *Jom-Us* **2012,** *64* (7), 752-763.

16. Mizushima, K.; Jones, P. C.; Wiseman, P. J.; Goodenough, J. B., Lixcoo2 "(Oless-Thanxless-Than-or-Equal-To1) - a New Cathode Material for Batteries of High-Energy Density. *Mater Res Bull* **1980,** *15* (6), 783-789.

17. Padhi, A. K.; Nanjundaswamy, K. S.; Goodenough, J. B., Phospho-olivines as positive-electrode materials for rechargeable lithium batteries. *J Electrochem Soc* **1997,** *144* (4), 1188-1194.

18. Thackeray, M. M.; David, W. I. F.; Bruce, P. G.; Goodenough, J. B., Lithium Insertion into Manganese Spinels. *Mater Res Bull* **1983,** *18* (4), 461-472.

19. Fiévet, F.; Brayner, R., The Polyol Process. In *Nanomaterials: A Danger or a Promise?*, Brayner, R.; Fiévet, F.; Coradin, T., Eds. Springer London: **2013**; Chapter 1, pp 1-25.

20. Cha, S. I.; Mo, C. B.; Kim, K. T.; Jeong, Y. J.; Hong, S. H., Mechanism for controlling the shape of Cu nanocrystals prepared by the polyol process. *Journal of Materials Research* **2006,** *21* (09), 2371-2378.

21. Feldmann, C., Polyol-mediated synthesis of nanoscale functional materials. *Adv Funct Mater* **2003,** *13* (2), 101-107.

22. Feldmann, C.; Jungk, H. O., Polyol-mediated preparation of nanoscale oxide particles. *Angew Chem Int Edit* **2001,** *40* (2), 359-362.

23. Carroll, K. J.; Reveles, J. U.; Shultz, M. D.; Khanna, S. N.; Carpenter, E. E., Preparation of Elemental Cu and Ni Nanoparticles by the Polyol Method: An Experimental and Theoretical Approach. *J Phys Chem C* **2011,** *115* (6), 2656-2664.

24. Fievet, F.; Lagier, J. P.; Blin, B.; Beaudoin, B.; Figlarz, M., Homogeneous and Heterogeneous Nucleations in the Polyol Process for the Preparation of Micron and Sub-Micron Size Metal Particles. *Solid State Ionics* **1989,** *32-3*, 198-205.

25. Orel, Z. C.; Matijevic, E.; Goia, D. V., Conversion of uniform colloidal Cu2O spheres to copper in polyols. *J Mater Res* **2003,** *18* (4), 1017-1022.

26. Feldmann, C., Polyol-mediated synthesis of nanoscale functional materials. *Solid State Sci* **2005,** *7* (7), 868-873.

27. LaMer, V. K.; Dinegar, R. H., Theory, Production and Mechanism of Formation of Monodispersed Hydrosols. *Journal of the American Chemical Society* **1950,** *72* (11), 4847-4854.

28. Carroll, K. J.; Huba, Z. J.; Spurgeon, S. R.; Qian, M. C.; Khanna, S. N.; Hudgins, D. M.; Taheri, M. L.; Carpenter, E. E., Magnetic properties of Co2C and Co3C nanoparticles and their assemblies. *Appl Phys Lett* **2012,** *101* (1).

29. Perdew, J. P.; Burke, K.; Wang, Y., Generalized gradient approximation for the exchange-correlation hole of a many-electron system. *Phys Rev B* **1996,** *54* (23), 16533-16539.

30. Harris, V. G.; Chen, Y.; Yang, A.; Yoon, S.; Chen, Z.; Geiler, A. L.; Gao, J.; Chinnasamy, C. N.; Lewis, L. H.; Vittoria, C.; Carpenter, E. E.; Carroll, K. J.; Goswami, R.; Willard, M. A.; Kurihara, L.; Gjoka, M.; Kalogirou, O., High coercivity cobalt carbide nanoparticles processed via polyol reaction: a new permanent magnet material. *J Phys D Appl Phys* **2010,** *43* (16).

31. Julien, C. M.; Mauger, A.; Zaghib, K.; Liu, D., High Voltage Cathode Materials. *Green Energy Technol* **2015**, 477-509.

32. Santhanam, R.; Rambabu, B., Research progress in high voltage spinel LiNi0.5Mn1.5O4 material. *Journal of Power Sources* **2010,** *195* (17), 5442-5451.

33. Yano, J.; Yachandra, V. K., X-ray absorption spectroscopy. *Photosynth Res* **2009,** *102* (2-3), 241-254.

34. Bunker, G., *Introduction to XAFS : a practical guide to X-ray absorption fine structure spectroscopy*. Cambridge University Press: Cambridge, UK ; New York, **2010**; p viii, 260 p.

35. Pike, C. R.; Roberts, A. P.; Verosub, K. L., Characterizing interactions in fine magnetic particle systems using first order reversal curves. *Journal of Applied Physics* **1999,** *85* (9), 6660-6667.

36. Roberts, A. P.; Pike, C. R.; Verosub, K. L., First-order reversal curve diagrams: A new tool for characterizing the magnetic properties of natural samples. *J Geophys Res-Sol Ea* **2000,** *105* (B12), 28461-28475.

37. Bertotti, G., *Hysteresis in magnetism : for physicists, materials scientists, and engineers*. Academic Press: San Diego, **1998**; p xvii, 558 p.

38. Heslop, D.; Muxworthy, A. R., Aspects of calculating first-order reversal curve distributions. *J Magn Magn Mater* **2005,** *288*, 155-167.

39. Dodrill, B. C.; Lindemuth, J. R.; Radu, C.; Reichard, H. S., High-temperature FORC study of single- and multi-phase permanent magnets LAKE SHORE CRYOTRONICS, INC. *Mrs Bull* **2015,** *40* (11), 903-904.

40. Carvallo, C.; Muxworthy, A. R.; Dunlop, D. J., First-order reversal curve (FORC) diagrams of magnetic mixtures: Micromagnetic models and measurements. *Phys Earth Planet In* **2006,** *154* (3-4), 308-322.

41. Harrison, R. J.; Feinberg, J. M., FORCinel: An improved algorithm for calculating first-order reversal curve distributions using locally weighted regression smoothing. *Geochem Geophy Geosy* **2008,** *9*.

42. Nellist, P. D., Scanning Transmission Electron Microscopy. In *Science of Microscopy*, Hawkes, P. W.; Spence, J. C. H., Eds. Springer New York: New York, NY, **2007**, pp 65-132.

43. Muller, D. A., Structure and bonding at the atomic scale by scanning transmission electron microscopy. *Nat Mater* **2009,** *8* (4), 263-270.

44. Pennycook, S. J.; Jesson, D. E.; McGibbon, A. J.; Nellist, P. D., High angle dark field STEM for advanced materials. *J Electron Microsc* **1996,** *45* (1), 36-43.

45. Harris, V. G.; Chen, Y.; Yang, A.; Yoon, S.; Chen, Z.; Geiler, A. L.; Gao, J.; Chinnasamy, C. N.; Lewis, L. H.; Vittoria, C.; Carpenter, E. E.; Carroll, K. J.; Goswami, R.; Willard, M. A.; Kurihara, L.; Gjoka, M.; Kalogirou, O., High coercivity cobalt carbide nanoparticles processed via polyol reaction: a new permanent magnet material. *Journal of Physics D: Applied Physics* **2010,** *43* (16), 165003.

46. Kuo, C. L.; Hwang, K. C., Does Morphology of a Metal Nanoparticle Play a Role in Ostwald Ripening Processes? *Chemistry of Materials* **2013,** *25* (3), 365-371.

47. Sun, S. H.; Murray, C. B.; Weller, D.; Folks, L.; Moser, A., Monodisperse FePt nanoparticles and ferromagnetic FePt nanocrystal superlattices. *Science* **2000,** *287* (5460), 1989-1992.

48. Wu, N.; Fu, L.; Su, M.; Aslam, M.; Wong, K. C.; Dravid, V. P., Interaction of Fatty Acid Monolayers with Cobalt Nanoparticles. *Nano Letters* **2004,** *4* (2), 383-386.

49. Amans, D.; Malaterre, C.; Diouf, M.; Mancini, C.; Chaput, F.; Ledoux, G.; Breton, G.; Guillin, Y.; Dujardin, C.; Masenelli-Varlot, K.; Perriat, P., Synthesis of Oxide Nanoparticles by Pulsed Laser Ablation in Liquids Containing a Complexing Molecule: Impact on Size Distributions and Prepared Phases. *The Journal of Physical Chemistry C* **2011,** *115* (12), 5131-5139.

50. Skrabalak, S. E.; Wiley, B. J.; Kim, M.; Formo, E. V.; Xia, Y., On the Polyol Synthesis of Silver Nanostructures: Glycolaldehyde as a Reducing Agent. *Nano Letters* **2008,** *8* (7), 2077-2081.

51. Xiong, Y.; Cai, H.; Wiley, B. J.; Wang, J.; Kim, M. J.; Xia, Y., Synthesis and Mechanistic Study of Palladium Nanobars and Nanorods. *Journal of the American Chemical Society* **2007,** *129* (12), 3665-3675.

52. Sankar, G.; Wright, P. A.; Natarajan, S.; Thomas, J. M.; Greaves, G. N.; Dent, A. J.; Dobson, B. R.; Ramsdale, C. A.; Jones, R. H., Combined QuEXAFS-XRD: a new technique in high-temperature materials chemistry; an illustrative in situ study of the zinc oxide-enhanced solid-state production of cordierite from a precursor zeolite. *The Journal of Physical Chemistry* **1993,** *97* (38), 9550-9554.

53. Harada, M.; Kamigaito, Y., Nucleation and Aggregative Growth Process of Platinum Nanoparticles Studied by in Situ Quick XAFS Spectroscopy. *Langmuir* **2011,** *28* (5), 2415-2428.

54. Harada, M.; Tamura, N.; Takenaka, M., Nucleation and Growth of Metal Nanoparticles during Photoreduction Using In Situ Time-Resolved SAXS Analysis. *The Journal of Physical Chemistry C* **2011,** *115* (29), 14081-14092.

55. Harada, M.; Inada, Y., In Situ Time-Resolved XAFS Studies of Metal Particle Formation by Photoreduction in Polymer Solutions. *Langmuir* **2009,** *25* (11), 6049-6061.

56. Bando, K. K.; Wada, T.; Miyamoto, T.; Miyazaki, K.; Takakusagi, S.; Koike, Y.; Inada, Y.; Nomura, M.; Yamaguchi, A.; Gott, T.; Oyama, S. T.; Asakura, K., Combined in situ QXAFS and FTIR analysis of a Ni phosphide catalyst under hydrodesulfurization conditions. *J Catal* **2012,** *286*, 165-171.

57. Caballero, A.; Gonzalezelipe, A. R.; Fernandez, A.; Herrmann, J. M.; Dexpert, H.; Villain, F., Experimental Set-up for in-Situ X-Ray-Absorption Spectroscopy Analysis of Photochemical-Reactions - the Photocatalytic Reduction of Gold on Titania. *J Photoch Photobio A* **1994,** *78* (2), 169-172.

58. Pun, G. P. P.; Mishin, Y., Embedded-atom potential for hcp and fcc cobalt. *Physical Review B* **2012,** *86* (13), 134116.

59. Tolédano, P.; Krexner, G.; Prem, M.; Weber, H. P.; Dmitriev, V. P., Theory of the martensitic transformation in cobalt. *Physical Review B* **2001,** *64* (14), 144104.

60. Treacy, M. M. J.; Newsam, J. M.; Deem, M. W., A General Recursion Method for Calculating Diffracted Intensities from Crystals Containing Planar Faults. *P Roy Soc Lond a Mat* **1991,** *433* (1889), 499-520.

61. Stephens, P. W., Phenomenological model of anisotropic peak broadening in powder diffraction. *Journal of Applied Crystallography* **1999,** *32* (2), 281-289.

62. Garcia-Otero, J.; Porto, M.; Rivas, J., Henkel plots of single-domain ferromagnetic particles. *Journal of Applied Physics* **2000,** *87* (10), 7376-7381.

63. Wohlfarth, E. P., Relations between Different Modes of Acquisition of the Remanent Magnetization of Ferromagnetic Particles. *Journal of Applied Physics* **1958,** *29* (3), 595-595.

64. Gao, R. W.; Chen, W.; Zhang, J. C.; Fong, W. C.; Li, W.; Li, X. M., Intergrain interaction, coercivity and Henkel plot for NdFeB magnets. *J Mater Sci Technol* **2001,** *17*, S93-S96.

65. Davies, J. E.; Wu, J.; Leighton, C.; Liu, K., Magnetization reversal and nanoscopic magnetic-phase separation in La_{1−x}Sr_{x}CoO_{3}. *Physical Review B* **2005,** *72* (13), 134419.

66. Avrami, M., Kinetics of phase change I - General theory. *J Chem Phys* **1939,** *7* (12), 1103-1112.

67. Avrami, M., Granulation, Phase Change, and Microstructure - Kinetics of Phase Change. III. *J Chem Phys* **1941,** *9* (2), 177-184.

68. Watzky, M. A.; Finke, R. G., Transition Metal Nanocluster Formation Kinetic and Mechanistic Studies. A New Mechanism When Hydrogen Is the Reductant: Slow, Continuous Nucleation and Fast Autocatalytic Surface Growth. *Journal of the American Chemical Society* **1997,** *119* (43), 10382-10400.

69. Kodama, D.; Shinoda, K.; Sato, K.; Sato, Y.; Jeyadevan, B.; Tohji, K., Synthesis of size-controlled Fe–Co alloy nanoparticles by modified polyol process. *J Magn Magn Mater* **2007,** *310* (2, Part 3), 2396-2398.

70. Cheng, J.; Hu, P.; Ellis, P.; French, S.; Kelly, G.; Lok, C. M., Density Functional Theory Study of Iron and Cobalt Carbides for Fischer−Tropsch Synthesis. *The Journal of Physical Chemistry C* **2009,** *114* (2), 1085-1093.

71. Stolbov, S.; Hong, S.; Kara, A.; Rahman, T. S., Origin of the C-induced p4g reconstruction of Ni(001). *Physical Review B* **2005,** *72* (15), 155423.

72. Tsakoumis, N. E.; Ronning, M.; Borg, O.; Rytter, E.; Holmen, A., Deactivation of cobalt based Fischer-Tropsch catalysts: A review. *Catal Today* **2010,** *154* (3-4), 162-182.

73. Lahiri, J.; Miller, T.; Adamska, L.; Oleynik, I. I.; Batzill, M., Graphene Growth on Ni(111) by Transformation of a Surface Carbide. *Nano Letters* **2010,** *11* (2), 518-522.

74. Baumgartner, J.; Dey, A.; Bomans, P. H.; Le Coadou, C.; Fratzl, P.; Sommerdijk, N. A.; Faivre, D., Nucleation and growth of magnetite from solution. *Nature materials* **2013,** *12* (4), 310-4.

75. Sathiya, M.; Abakumov, A. M.; Foix, D.; Rousse, G.; Ramesha, K.; Saubanere, M.; Doublet, M. L.; Vezin, H.; Laisa, C. P.; Prakash, A. S.; Gonbeau, D.; VanTendeloo, G.; Tarascon, J. M., Origin of voltage decay in high-capacity layered oxide electrodes. *Nat Mater* **2015,** *14* (2), 230-238.

76. Kim, M. C.; Nam, K. W.; Hu, E. Y.; Yang, X. Q.; Kim, H.; Kang, K.; Aravindan, V.; Kim, W. S.; Lee, Y. S., Sol- Gel Synthesis of Aliovalent Vanadium- Doped LiNi0.Mn-5(1).O-5(4) Cathodes with Excellent Performance at High Temperatures. *Chemsuschem* **2014,** *7* (3), 829-834.

77. Huang, R.; Ikuhara, Y. H.; Mizoguchi, T.; Findlay, S. D.; Kuwabara, A.; Fisher, C. A. J.; Moriwake, H.; Oki, H.; Hirayama, T.; Ikuhara, Y., Oxygen-Vacancy Ordering at Surfaces of Lithium Manganese(III,IV) Oxide Spinel Nanoparticles. *Angew Chem Int Edit* **2011,** *50* (13), 3053-3057.

78. Kim, J. H.; Yoon, C. S.; Myung, S. T.; Prakash, J.; Sun, Y. K., Phase transitions in Li1-delta Ni0.5Mn1.5O4 during cycling at 5 v. *Electrochem Solid St* **2004,** *7* (7), A216-A220.

79. Manthiram, A.; Chemelewski, K.; Lee, E.-S., A perspective on the high-voltage LiMn1.5Ni0.5O4 spinel cathode for lithium-ion batteries. *Energy & Environmental Science* **2014**.

80. Liu, D.; Zhu, W.; Trottier, J.; Gagnon, C.; Barray, F.; Guerfi, A.; Mauger, A.; Groult, H.; Julien, C. M.; Goodenough, J. B.; Zaghib, K., Spinel materials for high-voltage cathodes in Li-ion batteries. *RSC Advances* **2014,** *4* (1), 154-167.

81. Xiao, J.; Chen, X.; Sushko, P. V.; Sushko, M. L.; Kovarik, L.; Feng, J.; Deng, Z.; Zheng, J.; Graff, G. L.; Nie, Z.; Choi, D.; Liu, J.; Zhang, J.-G.; Whittingham, M. S., High-Performance LiNi0.5Mn1.5O4 Spinel Controlled by Mn3+ Concentration and Site Disorder. *Adv. Mater.* **2012,** *24* (16), 2109-2116.

82. Cho, H.-M.; Meng, Y. S., Effect of Ni/Mn Ordering on Elementary Polarizations of LiNi0.5Mn1.5O4 Spinel and Its Nanostructured Electrode. *J. Electrochem. Soc.* **2013,** *160* (9), A1482-A1488.

83. Ulvestad, A.; Singer, A.; Cho, H.-M.; Clark, J. N.; Harder, R.; Maser, J.; Meng, Y. S.; Shpyrko, O. G., Single Particle Nanomechanics in Operando Batteries via Lensless Strain Mapping. *Nano Lett.* **2014,** *14* (9), 5123-5127.

84. Singer, A.; Ulvestad, A.; Cho, H.-M.; Kim, J. W.; Maser, J.; Harder, R.; Meng, Y. S.; Shpyrko, O. G., Nonequilibrium Structural Dynamics of Nanoparticles in LiNi1/2Mn3/2O4 Cathode under Operando Conditions. *Nano Lett.* **2014,** *14* (9), 5295-5300.

85. Xia, Y. Y.; Zhou, Y. H.; Yoshio, M., Capacity fading on cycling of 4 V Li/LiMn2O4 cells. *J Electrochem Soc* **1997,** *144* (8), 2593-2600.

86. Zhan, C.; Lu, J.; Jeremy Kropf, A.; Wu, T.; Jansen, A. N.; Sun, Y.-K.; Qiu, X.; Amine, K., Mn(II) deposition on anodes and its effects on capacity fade in spinel lithium manganate–carbon systems. *Nat Commun* **2013,** *4*.

87. Lin, M. X.; Ben, L. B.; Sun, Y.; Wang, H.; Yang, Z. Z.; Gu, L.; Yu, X. Q.; Yang, X. Q.; Zhao, H. F.; Yu, R.; Armand, M.; Huang, X. J., Insight into the Atomic Structure of High-Voltage Spinel LiNiO3Mn1.5O4 Cathode Material in the First Cycle. *Chemistry of Materials* **2015,** *27* (1), 292-303.

88. Pistoia, G.; Antonini, A.; Rosati, R.; Zane, D., Storage characteristics of cathodes for Li-ion batteries. *Electrochim Acta* **1996,** *41* (17), 2683-2689.

89. Pieczonka, N. P. W.; Liu, Z. Y.; Lu, P.; Olson, K. L.; Moote, J.; Powell, B. R.; Kim, J. H., Understanding Transition-Metal Dissolution Behavior in LiNi0.5Mn1.5O4 High-Voltage Spinel for Lithium Ion Batteries. *J Phys Chem C* **2013,** *117* (31), 15947-15957.

90. Aurbach, D.; Levi, M. D.; Gamulski, K.; Markovsky, B.; Salitra, G.; Levi, E.; Heider, U.; Heider, L.; Oesten, R., Capacity fading of LixMn2O4 spinel electrodes studied by XRD and electroanalytical techniques. *Journal of Power Sources* **1999,** *81–82*, 472-479.

91. Huang, H. T.; Vincent, C. A.; Bruce, P. G., Capacity loss of lithium manganese oxide spinel in LiPF6/ethylene carbonate-dimethyl carbonate electrolytes. *J Electrochem Soc* **1999,** *146* (2), 481-485.

92. Jang, D. H.; Shin, Y. J.; Oh, S. M., Dissolution of spinel oxides and capacity losses in 4V Li/LixMn2O4 coils. *J Electrochem Soc* **1996,** *143* (7), 2204-2211.

93. Kim, M. C.; Kim, S. H.; Aravindan, V.; Kim, W. S.; Lee, S. Y.; Lee, Y. S., Ultrathin Polyimide Coating for a Spinel LiNi0.5Mn1.5O4 Cathode and Its Superior Lithium Storage Properties under Elevated Temperature Conditions. *J Electrochem Soc* **2013,** *160* (8), A1003-A1008.

94. Kim, J.-H.; Pieczonka, N. P. W.; Li, Z.; Wu, Y.; Harris, S.; Powell, B. R., Understanding the capacity fading mechanism in LiNi0.5Mn1.5O4/graphite Li-ion batteries. *Electrochim Acta* **2013,** *90*, 556-562.

95. MahootcheianAsl, N.; Kim, J. H.; Pieczonka, N. P. W.; Liu, Z. Y.; Kim, Y., Multilayer electrolyte cell: A new tool for identifying electrochemical performances of high voltage cathode materials. *Electrochem Commun* **2013,** *32*, 1-4.

96. Fang, X.; Ding, N.; Feng, X. Y.; Lu, Y.; Chen, C. H., Study of LiNi0.5Mn1.5O4 synthesized via a chloride-ammonia co-precipitation method: Electrochemical performance, diffusion coefficient and capacity loss mechanism. *Electrochim Acta* **2009,** *54* (28), 7471-7475.

97. Choi, W.; Manthiram, A., Comparison of metal ion dissolutions from lithium ion battery cathodes. *J Electrochem Soc* **2006,** *153* (9), A1760-A1764.

98. Shin, Y. J.; Manthiram, A., Microstrain and capacity fade in spinel manganese oxides. *Electrochem Solid St* **2002,** *5* (3), A55-A58.

99. Tang, D. C.; Sun, Y.; Yang, Z. Z.; Ben, L. B.; Gu, L.; Huang, X. J., Surface Structure Evolution of LiMn2O4 Cathode Material upon Charge/Discharge. *Chemistry of Materials* **2014,** *26* (11), 3535-3543.

100. Shukla, A. K.; Ramasse, Q. M.; Ophus, C.; Duncan, H.; Hage, F.; Chen, G. Y., Unravelling structural ambiguities in lithium- and manganese-rich transition metal oxides. *Nat Commun* **2015,** *6*.

101. Song, J.; Shin, D. W.; Lu, Y.; Amos, C. D.; Manthiram, A.; Goodenough, J. B., Role of Oxygen Vacancies on the Performance of Li[Ni0.5–xMn1.5+x]O4 (x = 0, 0.05, and 0.08) Spinel Cathodes for Lithium-Ion Batteries. *Chem. Mat.* **2012,** *24* (15), 3101-3109.

102. Hagh, N. M.; Cosandey, F.; Rangan, S.; Bartynski, R.; Amatucci, G. G., Electrochemical Performance of Acid-Treated Nanostructured LiMn1.5Ni0.5O4 − δ Spinel at Elevated Temperature. *J. Electrochem. Soc.* **2010,** *157* (3), A305-A319.

103. Thackeray, M. M.; Shao-Horn, Y.; Kahaian, A. J.; Kepler, K. D.; Vaughey, J. T.; Hackney, S. A., Structural fatigue in spinel electrodes in high voltage (4V) Li/LixMn2O4 cells. *Electrochem Solid St* **1998,** *1* (1), 7-9.

104. Larcher, D.; Patrice, R., Preparation of metallic powders and alloys in polyol media: A thermodynamic approach. *J Solid State Chem* **2000,** *154* (2), 405-411.

105. Poul, L.; Ammar, S.; Jouini, N.; Fievet, F.; Villain, F., Synthesis of inorganic compounds (metal, oxide and hydroxide) in polyol medium: A versatile route related to the sol-gel process. *Journal of Sol-Gel Science and Technology* **2003,** *26* (1-3), 261-265.

106. Yoon, H.; Xu, A.; Sterbinsky, G. E.; Arena, D. A.; Wang, Z.; Stephens, P. W.; Meng, Y. S.; Carroll, K. J., In situ non-aqueous nucleation and growth of next generation rare-earth-free permanent magnets. *Physical Chemistry Chemical Physics* **2015,** *17* (2), 1070-1076.

107. Qiu, L.; Pol, V. G.; Calderon-Moreno, J.; Gedanken, A., Synthesis of tin nanorods via a sonochemical method combined with a polyol process. *Ultrasonics Sonochemistry* **2005,** *12* (4), 243-247.

108. Cho, H. M.; Meng, Y. S., Effect of Ni/Mn Ordering on Elementary Polarizations of LiNi0.5Mn1.5O4 Spinel and Its Nanostructured Electrode. *Journal of the Electrochemical Society* **2013,** *160* (9), A1482-A1488.

109. Carroll, K. J.; Yang, M.-C.; Veith, G. M.; Dudney, N. J.; Meng, Y. S., Intrinsic Surface Stability in LiMn2–xNixO4–δ ($x = 0.45, 0.5$) High Voltage Spinel Materials for Lithium Ion Batteries. *Electrochemical and Solid-State Letters* **2012,** *15* (5), A72-A75.

110. Yang, M.-C.; Xu, B.; Cheng, J.-H.; Pan, C.-J.; Hwang, B.-J.; Meng, Y. S., Electronic, Structural, and Electrochemical Properties of LiNixCuyMn2–x–yO4 ($0 < x < 0.5$, $0 < y < 0.5$) High-Voltage Spinel Materials. *Chem. Mat.* **2011,** *23* (11), 2832-2841.

111. Wang, Z. L.; Yin, J. S.; Jiang, Y. D., EELS analysis of cation valence states and oxygen vacancies in magnetic oxides. *Micron* **2000,** *31* (5), 571-580.

112. Carroll, K. J.; Qian, D.; Fell, C.; Calvin, S.; Veith, G. M.; Chi, M. F.; Baggetto, L.; Meng, Y. S., Probing the electrode/electrolyte interface in the lithium excess layered oxide Li1.2Ni0.2Mn0.6O2. *Phys Chem Chem Phys* **2013,** *15* (26), 11128-11138.

113. Ravel, B.; Newville, M., ATHENA, ARTEMIS, HEPHAESTUS: data analysis for X-ray absorption spectroscopy using IFEFFIT. *Journal of synchrotron radiation* **2005,** *12* (4), 537-541.

114. Zhong, G. B.; Wang, Y. Y.; Yu, Y. Q.; Chen, C. H., Electrochemical investigations of the LiNi0.45M0.10Mn1.45O4 (M = Fe, Co, Cr) 5 V cathode materials for lithium ion batteries. *J. Power Sources* **2012,** *205* (0), 385-393.

115. Abbate, M.; Goedkoop, J. B.; de Groot, F. M. F.; Grioni, M.; Fuggle, J. C.; Hofmann, S.; Petersen, H.; Sacchi, M., Probing depth of soft x-ray absorption spectroscopy measured in total-electron-yield mode. *Surface and Interface Analysis* **1992,** *18* (1), 65-69.

116. Schroeder, S. L. M., Towards a 'universal curve' for total electron-yield XAS. *Solid State Commun* **1996,** *98* (5), 405-409.

117. Kurata, H.; Lefevre, E.; Colliex, C.; Brydson, R., Electron-Energy-Loss near-Edge Structures in the Oxygen K-Edge Spectra of Transition-Metal Oxides. *Phys Rev B* **1993,** *47* (20), 13763-13768.

118. Xu, B.; Fell, C. R.; Chi, M. F.; Meng, Y. S., Identifying surface structural changes in layered Li-excess nickel manganese oxides in high voltage lithium ion batteries: A joint experimental and theoretical study. *Energ Environ Sci* **2011,** *4* (6), 2223-2233.

119. Graetz, J.; Ahn, C. C.; Ouyang, H.; Rez, P.; Fultz, B., White lines and d-band occupancy for the $3d$ transition-metal oxides and lithium transition-metal oxides. *Phys Rev B* **2004,** *69* (23), 235103.

120. Lin, F.; Nordlund, D.; Pan, T. J.; Markus, I. M.; Weng, T. C.; Xin, H. L. L.; Doeff, M. M., Influence of synthesis conditions on the surface passivation and electrochemical behavior of layered cathode materials. *J Mater Chem A* **2014,** *2* (46), 19833-19840.

121. Wang, F.; Yang, J.; NuLi, Y. N.; Wang, J. L., Highly promoted electrochemical performance of 5 V LiCoPO4 cathode material by addition of vanadium. *Journal of Power Sources* **2010,** *195* (19), 6884-6887.

122. Sharabi, R.; Markevich, E.; Borgel, V.; Salitra, G.; Aurbach, D.; Semrau, G.; Schmidt, M. A.; Schall, N.; Stinner, C., Significantly improved cycling performance of LiCoPO4 cathodes. *Electrochem Commun* **2011,** *13* (8), 800-802.

123. Sharabi, R.; Markevich, E.; Fridman, K.; Gershinsky, G.; Salitra, G.; Aurbach, D.; Semrau, G.; Schmidt, M. A.; Schall, N.; Bruenig, C., Electrolyte solution for the improved cycling performance of LiCoPO4/C composite cathodes. *Electrochem Commun* **2013,** *28*, 20-23.

124. Bramnik, N. N.; Bramnik, K. G.; Buhrmester, T.; Baehtz, C.; Ehrenberg, H.; Fuess, H., Electrochemical and structural study of LiCoPO4-based electrodes. *J Solid State Electr* **2004,** *8* (8), 558-564.

125. Amine, K.; Yasuda, H.; Yamachi, M., Olivine LiCoPO4 as 4.8 V electrode material for lithium batteries. *Electrochem Solid St* **2000,** *3* (4), 178-179.

126. Xing, L. Y.; Hu, M.; Tang, Q.; Wei, J. P.; Qin, X.; Zhou, Z., Improved cyclic performances of LiCoPO4/C cathode materials for high-cell-potential lithium-ion batteries with thiophene as an electrolyte additive. *Electrochim Acta* **2012,** *59*, 172-178.

127. Kang, Y. M.; Kim, Y. I.; Oh, M. W.; Yin, R. Z.; Lee, Y.; Han, D. W.; Kwon, H. S.; Kim, J. H.; Ramanath, G., Structurally stabilized olivine lithium phosphate cathodes with enhanced electrochemical properties through Fe doping. *Energ Environ Sci* **2011,** *4* (12), 4978-4983.

128. Allen, J. L.; Jow, T. R.; Wolfenstine, J., LiCoPO4 as Li-ion Cathode. *Ecs Transactions* **2012,** *41* (29), 15-20.

129. Nakayama, M.; Goto, S.; Uchimoto, Y.; Wakihara, M.; Kitajima, Y., Changes in electronic structure between cobalt and oxide ions of lithium cobalt phosphate as 4.8-V positive electrode material. *Chemistry of Materials* **2004,** *16* (18), 3399-3401.

130. Park, K. Y.; Park, I.; Kim, H.; Lim, H. D.; Hong, J.; Kim, J.; Kang, K., Anti-Site Reordering in LiFePO4: Defect Annihilation on Charge Carrier Injection. *Chem Mater* **2014,** *26* (18), 5345-5351.

131. Truong, Q. D.; Devaraju, M. K.; Tomai, T.; Honma, I., Direct Observation of Antisite Defects in LiCoPO4 Cathode Materials by Annular Dark- and Bright-Field Electron Microscopy. *Acs Appl Mater Inter* **2013,** *5* (20), 9926-9932.

132. Devaraju, M. K.; Truong, Q. D.; Tomai, T.; Hyodo, H.; Sasaki, Y.; Honma, I., Antisite defects in LiCoPO4 nanocrystals synthesized via a supercritical fluid process. *Rsc Adv* **2014,** *4* (94), 52410-52414.

133. Truong, Q. D.; Deyaraju, M. K.; Sasaki, Y.; Hyodo, H.; Tomai, T.; Honma, I., Relocation of Cobalt Ions in Electrochemically Delithiated LiCoPO4 Cathode Materials. *Chemistry of Materials* **2014,** *26* (9), 2770-2773.

134. Sugiyama, J.; Nozaki, H.; Harada, M.; Kamazawa, K.; Ikedo, Y.; Miyake, Y.; Ofer, O.; Mansson, M.; Ansaldo, E. J.; Chow, K. H.; Kobayashi, G.; Kanno, R., Diffusive behavior in LiMPO4 with M = Fe, Co, Ni probed by muon-spin relaxation. *Phys Rev B* **2012,** *85* (5).

135. Boulineau, A.; Gutel, T., Revealing Electrochemically Induced Antisite Defects in LiCoPO4: Evolution upon Cycling. *Chemistry of Materials* **2015,** *27* (3), 802-807.

136. Bramnik, N. N.; Bramnik, K. G.; Baehtz, C.; Ehrenberg, H., Study of the effect of different synthesis routes on Li extraction-insertion from LiCoPO4. *Journal of Power Sources* **2005,** *145* (1), 74-81.

137. Guo, B. B.; Ruan, H. C.; Zheng, C.; Fei, H. L.; Wei, M. D., Hierarchical LiFePO4 with a controllable growth of the (010) facet for lithium-ion batteries. *Sci Rep-Uk* **2013,** *3*.

138. Devaraju, M. K.; Rangappa, D.; Honma, I., Controlled synthesis of plate-like LiCoPO4 nanoparticles via supercritical method and their electrode property. *Electrochim Acta* **2012,** *85*, 548-553.

139. Yoon, H. J.; Xu, A. R.; Sterbinsky, G. E.; Arena, D. A.; Wang, Z. Y.; Stephens, P. W.; Meng, Y. S.; Carroll, K. J., In situ non-aqueous nucleation and growth of next generation rare-earth-free permanent magnets. *Phys Chem Chem Phys* **2015,** *17* (2), 1070-1076.

140. Lim, J.; Kim, D.; Mathew, V.; Kim, J., Synthesis of LiMPO4 (M = Fe, Mn, Co) nanocrystals in polyol medium and their electrochemical properties. *Phys Scripta* **2010,** *T139*.

141. Lim, J. S.; Kim, D. H.; Jung, I. O.; Woo, C. H.; Choi, E. S.; Gim, J. H.; Kim, J., Synthesis and Electrochemical Properties of LiMPO4 (M = Fe, Mn, Co) Nanocrystals in Polyol Medium. *J Nanosci Nanotechno* **2010,** *10* (5), 3357-3361.

142. Markevich, E.; Salitra, G.; Fridman, K.; Sharabi, R.; Gershinsky, G.; Garsuch, A.; Semrau, G.; Schmidt, M. A.; Aurbach, D., Fluoroethylene Carbonate as an Important Component in Electrolyte Solutions for High-Voltage Lithium Batteries: Role of Surface Chemistry on the Cathode. *Langmuir* **2014,** *30* (25), 7414-7424.

143. Markevich, E.; Sharabi, R.; Gottlieb, H.; Borgel, V.; Fridman, K.; Salitra, G.; Aurbach, D.; Semrau, G.; Schmidt, M. A.; Schall, N.; Bruenig, C., Reasons for capacity fading of LiCoPO4 cathodes in LiPF6 containing electrolyte solutions. *Electrochem Commun* **2012,** *15* (1), 22-25.

144. Lin, F.; Markus, I. M.; Nordlund, D.; Weng, T. C.; Asta, M. D.; Xin, H. L. L.; Doeff, M. M., Surface reconstruction and chemical evolution of stoichiometric layered cathode materials for lithium-ion batteries. *Nature Communications* **2014,** *5*.

145. Markevich, E.; Sharabi, R.; Haik, O.; Borgel, V.; Salitra, G.; Aurbach, D.; Semrau, G.; Schmidt, M. A.; Schall, N.; Stinner, C., Raman spectroscopy of carbon-coated LiCoPO4 and LiFePO4 olivines. *Journal of Power Sources* **2011,** *196* (15), 6433-6439.

146. Allen, J. L.; Jow, T. R.; Wolfenstine, J., Improved cycle life of Fe-substituted LiCoPO4. *Journal of Power Sources* **2011,** *196* (20), 8656-8661.

147. Yang, M.; Du, C. Q.; Tang, Z. Y.; Wu, J. W.; Zhang, X. H., Synthesis of LiCoPO4 as a cathode material for lithium-ion battery by a polymer method. *Ionics* **2014,** *20* (7), 1039-1046.

148. Li, X. Y.; Zhang, B.; Zhang, Z. G.; He, L. H.; Li, H.; Huang, X. J.; Wang, F. W., Crystallographic structure of LiFe1-xMnxPO4 solid solutions studied by neutron powder diffraction. *Powder Diffr* **2014,** *29* (3), 248-253.

149. Nyten, A.; Thomas, J. O., A neutron powder diffraction study of LiCoxFe1-xPO4 for x=0, 0.25, 0.40, 0.60 and 0.75. *Solid State Ionics* **2006,** *177* (15-16), 1327-1330.

150. Bramnik, N. N.; Nikolowski, K.; Baehtz, C.; Bramnik, K. G.; Ehrenberg, H., Phase transitions occurring upon lithium insertion-extraction of LiCoPO4. *Chemistry of Materials* **2007,** *19* (4), 908-915.

151. Kaus, M.; Issac, I.; Heinzmann, R.; Doyle, S.; Mangold, S.; Hahn, H.; Chakravadhanula, V. S. K.; Kubel, C.; Ehrenberg, H.; Indris, S., Electrochemical Delithiation/Relithiation of LiCoPO4: A Two-Step Reaction Mechanism Investigated by in Situ X-ray Diffraction,

in Situ X-ray Absorption Spectroscopy, and ex Situ Li-7/P-31 NMR Spectroscopy. *J Phys Chem C* **2014,** *118* (31), 17279-17290.

152. Castro, L.; Dedryvere, R.; Ledeuil, J. B.; Breger, J.; Tessier, C.; Gonbeau, D., Aging Mechanisms of LiFePO4 // Graphite Cells Studied by XPS: Redox Reaction and Electrode/Electrolyte Interfaces. *J Electrochem Soc* **2012,** *159* (4), A357-A363.

153. Dedryvere, R.; Laruelle, S.; Grugeon, S.; Gireaud, L.; Tarascon, J. M.; Gonbeau, D., XPS identification of the organic and inorganic components of the electrode/electrolyte interface formed on a metallic cathode. *J Electrochem Soc* **2005,** *152* (4), A689-A696.

154. Dedryvere, R.; Maccario, M.; Croguennec, L.; Le Cras, F.; Delmas, C.; Gonbeau, D., X-Ray Photoelectron Spectroscopy Investigations of Carbon-Coated LixFePO4 Materials. *Chemistry of Materials* **2008,** *20* (22), 7164-7170.

155. Nanda, J.; Remillard, J.; O'Neill, A.; Bernardi, D.; Ro, T.; Nietering, K. E.; Go, J. Y.; Miller, T. J., Local State-of-Charge Mapping of Lithium-Ion Battery Electrodes. *Adv Funct Mater* **2011,** *21* (17), 3282-3290.

156. Lin, F.; Markus, I. M.; Nordlund, D.; Weng, T. C.; Asta, M. D.; Xin, H. L. L.; Doeff, M. M., Surface reconstruction and chemical evolution of stoichiometric layered cathode materials for lithium-ion batteries. *Abstr Pap Am Chem S* **2014,** *248*.

157. Andre, D.; Kim, S. J.; Lamp, P.; Lux, S. F.; Maglia, F.; Paschos, O.; Stiaszny, B., Future generations of cathode materials: an automotive industry perspective. *J Mater Chem A* **2015,** *3* (13), 6709-6732.

158. Jung, S. K.; Gwon, H.; Hong, J.; Park, K. Y.; Seo, D. H.; Kim, H.; Hyun, J.; Yang, W.; Kang, K., Understanding the Degradation Mechanisms of LiNi0.5Co0.2Mn0.3O2 Cathode Material in Lithium Ion Batteries. *Adv Energy Mater* **2014,** *4* (1).